Master's thesis

NTNU
Norwegian University of Science and Technology
Faculty of Information Technology and Electrical Engineering
Department of Engineering Cybernetics

Simen Krantz Knudsen

Model validation and berthing of an autonomous ferry

Master's thesis in Cybernetics and Robotics
Supervisor: Tor Arne Johansen
Co-supervisor: Håkon Hagen Helgesen and Giorgio D. K. Minde Kufoalor

June 2021

NTNU
Norwegian University of Science and Technology

Simen Krantz Knudsen

Model validation and berthing of an autonomous ferry

Master's thesis in Cybernetics and Robotics
Supervisor: Tor Arne Johansen
Co-supervisor: Håkon Hagen Helgesen and Giorgio D. K. Minde Kufoalor
June 2021

Norwegian University of Science and Technology
Faculty of Information Technology and Electrical Engineering
Department of Engineering Cybernetics

NTNU

Kunnskap for en bedre verden

Master's thesis

Candidate:	Simen Krantz Knudsen
Candidate no.:	10100
Course:	TTK4900 - Engineering Cybernetics, Master's Thesis
Thesis title:	Model validation and berthing of an autonomous ferry
Problem description:	Docking is one of the most common and complex vessel operations, where the vessel is "parked" in a designated space. Its complexity results from the need for maneuvers with relatively large changes in speed, heading and course within a very confined space with risk for collision with other vessels and structures. Limited controllability (thrust and steering) in combination with environmental forces from wind, currents and waves makes the problem challenging.

The main tasks will be:

1. To validate the mathematical models in the milliAmpere simulator, using experimental data collected by postdoctoral fellow Bjørn-Olav Holtung Eriksen on December 1, 2020.

2. To implement a model for first-order wave-induced forces, as well as second-order wave drift forces, in the milliAmpere simulator. The first-order wave forces should try to replicate wake wave forces from passing vessels.

3. To test a new berthing scheme experimentally, using the milliAmpere ferry as experimental platform. Discuss the results in detail, and propose further refinements for the berthing scheme.

Start date:	January 11, 2021
Due date:	June 7, 2021
Thesis performed at:	Department of Engineering Cybernetics, Norwegian University of Science and Technology
Supervisor:	Prof. Tor Arne Johansen [1]
Co-supervisors:	Håkon Hagen Helgesen [1] Giorgio D. K. Minde Kufoalor [2]

[1] Department of Engineering Cybernetics, NTNU

[2] Maritime Robotics AS, Trondheim

Abstract

The research on unmanned surface vessels is growing rapidly, with an increased focus on autonomous docking and berthing operations. This thesis aims to contribute to this research by presenting a new berthing scheme. The milliAmpere ferry is an autonomous ferry meant to operate around the waters of Ravnkloa, Trondheim, and will serve as both the simulation and experimental platform.

The first two tasks will be to validate mathematical models and implement two wave models in the milliAmpere simulator. The third task is to improve the berthing scheme first developed in the specialization project. The wave models were tested through three dynamic positioning stationkeeping tests. For the validation task, experimental reference data was replicated in the simulator by keeping the guidance system disabled during 35 simulations. Each simulation had different values for a subset of parameters. The berthing scheme underwent experimental tests in Havnebassenget, Trondheim. One prerequisite for the thesis is that the dynamic positioning system onboard the milliAmpere ferry yields a satisfactory closed-loop behavior. Consequently, this system will not be tuned or altered in any way, neither during the validation task, the berthing task nor to improve the behavior when the milliAmpere ferry is influenced by wave forces and moments.

The model of the first-order wave-induced forces and moments proved to be simple, yet effective for the purpose of simulating the milliAmpere ferry. The stationkeeping tests highlighted that the dynamic positioning controller should be tuned in future work, in order to better counteract these forces and moments. The validation task concluded that the azimuth angle model and motor speed gains, the reference model, the damping matrix and the thrust allocation algorithm should be in focus for later model validation and tuning work. The berthing scheme proved to be flexible and scalable through the experimental trials. Nevertheless, maintaining control in both sway and heading is necessary during the QUAY phase. Additionally, bumpless transfer or gain scheduling is needed for improvement of the transients during the phase transitions.

Sammendrag

Det blir stadig mer forskning på ubemannede overflatefartøy, med et økt fokus på dokking-operasjoner. Denne avhandlingen ønsker å bidra til denne forskningen ved å presentere en ny metode for dokking. milliAmpere-ferjen er en autonom ferje som skal operere i området rundt Ravnkloa i Trondheim, og vil brukes både i simuleringer og eksperimentelle forsøk.

De to første oppgavene består av å validere matematiske modeller og implementere to bølgemodeller i milliAmpere-simulatoren. Den tredje oppgaven vil være å forbedre dokking-metoden først utviklet i prosjektoppgaven. Bølgemodellene ble testet gjennom tre stasjonærtester som anvendte dynamisk posisjonerings-systemet. I valideringsoppgaven ble eksperimentell referansedata gjentatt i simulatoren ved å deaktivere gaidingsssystemet gjennom 35 simuleringer. Hver simulering hadde ulike verdier for utvalgte parametere. Dokking-metoden gjennomgikk eksperimentelle tester i Havnebassenget i Trondheim. En forutsetning for avhandlingen er at dynamisk posisjonerings-systemet ombord på milliAmpere-ferjen har en tilfredsstillende oppførsel i lukket sløyfe. Dette systemet vil dermed ikke bli tunet eller endret på noe vis, verken gjennom valideringsoppgaven, dokking-oppgaven eller for å bedre oppførselen når milliAmpere-ferjen er påvirket av bølgekrefter og -momenter.

Modellen for de førsteordens bølgekreftene og -momentene var enkel, men effektiv for simulering av milliAmpere-ferjen. Stasjonærtestene understreket at regulatoren i dynamisk posisjonerings-systemet bør tunes, for å bedre motvirke disse kreftene og momentene. Valideringsoppgaven konkluderte at modellen for azimuth-vinkelen, forsterkningene i motorhastighetsmodellen, referansemodellen, dempematrisen og kraftfordelingsalgoritmen bør fokuseres på i senere valideringsarbeider. De eksperimentelle testene viste at dokking-metoden er fleksibel og skalerbar. Likevel må regulering i både sway og heading opprettholdes gjennom QUAY-fasen. I tillegg vil bumpless transfer- eller gain-scheduling-teknikker være nødvendig for å bedre transientene ved faseoverganger.

Preface

This master's thesis is part of the fulfillment of the five-year Master of Science (M.Sc.) in Engineering Cybernetics at The Norwegian University of Science and Technology (NTNU) in Trondheim, Norway. The work throughout the thesis is based on the work conducted in the subject TTK4550 Engineering Cybernetics, Specialization Project, presented in Knudsen [2020].

I would like to thank my main supervisor professor Tor Arne Johansen for our discussions throughout this thesis, and for being very easy to reach by e-mail. My first co-supervisor Håkon Hagen Helgesen needs credit for helping me with large and small challenges alike throughout the thesis, as well as providing valuable input during the finalization. Many thanks to my second co-supervisor Giorgio D. K. Minde Kufoalor as well, for his suggestions and proposals regarding the motivation and focus of the work. The supervisors have provided both feedback and feedforward throughout the thesis.

To my family and Frida, I'm truly grateful for your support and ability to motivate me the last year. Furthermore, ten extraordinary guys have made the last five years fun and unforgettable, I hope to keep our Monday tradition in the years to come. A special thanks to Magne Sirnes, a dear friend and fellow fifth year student at ITK. He has been willing to discuss various problems I've encountered during the last five years in general, and during this thesis in particular. Lastly, Andreas Aurlien, another fifth year student at ITK, needs credit for providing help during the experiments with the milliAmpere ferry on April 19 and May 10.

Simen Krantz Knudsen
Trondheim, June 3, 2021

Table of Contents

List of Tables

List of Figures

Abbreviations

ASV	=	Autonomous surface vehicle
CO	=	Center of origin
COLREGs	=	International Regulations for Preventing Collisions at Sea
DOF	=	Degree of freedom
DP	=	Dynamic positioning
ECEF	=	Earth-centered Earth-fixed reference frame
ECI	=	Earth-centered inertial frame
FFT	=	Fast Fourier Transform
GNC	=	Guidance, navigation and control
GNSS	=	Global Navigation Satellite Systems
IMU	=	Inertial measurement unit
INS	=	Inertial navigation system
MAE	=	Mean absolute error
MPC	=	Model predictive control
NED	=	North-East-Down coordinate system
NTNU	=	Norwegian University of Science and Technology
PID	=	Proportional-integral-derivative
RAO	=	Response amplitude operator
RK4	=	Runge-Kutta 4th order method
RMSE	=	Root-mean-square error
ROS	=	Robot Operating System
RTK	=	Real-time kinematic
SSA	=	Smallest signed angle
USV	=	Unmanned surface vessel

Nomenclature

$\{n\}$	=	The North-East-Down (NED) frame
$\{b\}$	=	The BODY frame
x^n	=	Generalized north position
y^n	=	Generalized east position
ψ	=	Generalized heading/yaw angle
u	=	Surge velocity
v	=	Sway velocity
r	=	Yaw rate
U	=	Forward horizontal speed
β	=	Desired wave encounter angle
T_ψ	=	Time constant of the heading dynamics
m_j^i	=	Metric j associated to simulation i
$m_{\text{error},j}^i$	=	Error metric j associated to simulation i
κ_i	=	The cost associated to simulation i
σ_{opt}	=	Simulation with the most favorable model changes
α_{quay}	=	Angle of the quay structure, constant in $\{n\}$

Chapter 1

Introduction

This thesis will study berthing of an unmanned surface vessel (USV) influenced by wave forces and moments. Another major task of the thesis is validation of mathematical models and parameters in the milliAmpere simulator.

The simulator maneuvering model used in this thesis considers only 3 degrees of freedom (DOFs), where the main purpose is to develop and test control algorithms before experimental testing. Model-based control design simulators tend to be simplified [Fossen, 2021, p.5], i.e. the purpose of the simulator is to have a behavior which is ”good enough” before experimental trials. That being said, major model discrepancies must at least be brought to focus, and is the reason why the validation task was initiated.

In order to replicate the conditions in which the milliAmpere ferry performs docking operations, environmental forces must be modeled in the simulator as they appear in such conditions. Replicating these forces is the reason why the wave model task was initiated, as the simulator lacked wave models in general.

The thesis is a continuation of the work conducted in the specialization project [Knudsen, 2020] in the course *TTK4550 – Engineering Cybernetics, Specialization Project* at the Norwegian University of Science and Technology (NTNU). The specialization project studied berthing of the milliAmpere ferry when it was influenced by environmental forces, developing a new berthing scheme. The proposed berthing scheme needed improvements, refinement and experimental testing, and is the reason the berthing task was initiated. Sections 2.2, 2.3 and 4.1 are based upon chapter 3 in Knudsen [2020], while sections 3.5.1 and 4.3 present some of the same articles used in the specialization project. All the work which originates from the specialization project has been thoroughly altered and rewritten, including some figures drawn using the LaTeX packages PGF/TikZ.

1.1 Background and motivation

The motivation for the model validation task originates from Knudsen [2020], indicating inferior behavior in the simulator compared to experimental results from previous works

[Bitar et al., 2020, Martinsen et al., 2020]. Furthermore, the motivation for the implementation of the wave models is that the milliAmpere simulator lacks such models. Ocean current and wind models have been implemented during previous works. Additionally, the wake wave model may present itself as an alternative to state-space models and response amplitude operators, by modeling the forces and moments directly.

The motivation behind autonomous docking and berthing schemes in general encompass safety improvements, reducing stress and risk for the crew, development of a marine system which is fully autonomous, energy consumption, among others. Regarding energy or fuel consumption, a human crew may have to try two or three times in order to successfully dock a large vessel manually [Bentzrød, 2019]. Autonomous docking systems do not necessarily have to minimize the fuel consumption throughout the docking operation: A system capable of successful docking the vessel at the first attempt will nevertheless save fuel, simply by avoiding a second or third attempt. Thruster wear-and-tear may still be an issue to address.

Confined waters with stationary and moving objects to avoid may be the most challenging environment in which USVs operate. Most docking and berthing operations take place in such confined waters, e.g. ports, canals and rivers. Furthermore, the "golden rule of berthing" is to have a controlled approach towards the berth at a slow speed [Murdoch et al., 2012], and should be upheld.

In a similar matter, Maritime Robotics AS has expressed worries regarding the magnitude of the velocities that most common berthing schemes produce close to the quay. Large velocities close to a berth are dangerous for both the vessel, the humans onboard and the surroundings. These velocities are often caused by the control system trying to counteract various environmental forces and moments. The cause of this may largely be due to the use of position references from trajectory tracking (see definition 3.4.1) and third-order reference models. Finally, a berthing scheme which scales well, regardless of e.g. the size and speed of the vessel, as well as the quay structure, is desirable.

1.1.1 Summary of the specialization project

The goal of the specialization project, presented in Knudsen [2020], was to investigate a different berthing scheme compared to similar works [Bitar et al., 2020, Martinsen et al., 2019, 2020]: Close the final distance ($\sim 1\,\mathrm{m}$) to the quay by using a dynamic positioning (DP) system with disabled controller gains in surge, while commanding a constant velocity reference in surge for the DP controller to follow.

The motivation behind the berthing scheme was to replicate what most ferry captains do in practice, avoiding large velocities, accelerations and control inputs close to the quay, as well as improving the safety of the berthing vessel. The latter was tried by making the berthing scheme time independent (see definition 3.4.2). Simulation results, both with and without ocean currents and wave forces acting on the milliAmpere ferry, were presented.

The results indicated that control inputs were reduced close to the quay, as intended. During the berthing operation, the surge velocity and yaw rate decreased and remained

unchanged, respectively. The sway velocity increased close to the quay, which is unintentional. This increase became significant when environmental forces were present. Furthermore, control in sway and heading was poor close to the quay wall.

1.2 Thesis description and assumptions

What follows is the problem statement of the thesis, as well as the assumptions taken for the berthing scheme in particular.

1.2.1 Problem statement

Docking is one of the most common and complex vessel operations, where the vessel is ”parked” in a designated space. Its complexity results from the need for maneuvers with relatively large changes in speed, heading and course within a very confined space with risk for collision with other vessels and structures. Limited controllability (thrust and steering) in combination with environmental forces from wind, currents and waves makes the problem challenging. The main tasks of the thesis are the following:

1. Validate the mathematical models in the milliAmpere simulator, using experimental data collected by postdoctoral fellow Bjørn-Olav Holtung Eriksen on December 1, 2020.

2. Implement a model for first-order wave-induced forces, as well as second-order wave drift forces, in the milliAmpere simulator.

3. Improve the berthing scheme first developed by Knudsen [2020], and test the scheme experimentally.

Another goal of the thesis will be to summarize information regarding the milliAmpere ferry from different sources. Information and documentation about the ferry are spread across various sources, including various papers from recent years and a Github repository.

Lastly, the thesis aims to yield a presentation on the topic of unmanned surface vessels, with focus on USVs in ports and harbors. USVs influenced by environmental forces will also be considered. This is to give a background for the berthing scheme in particular, as well as to put this thesis in a wider perspective.

The difference between using a DP system on open water and during a docking scenario is vital to point out. During the docking operation, predicting the behavior of the vessel is crucial. The reason being that it is very challenging to correct the pose and velocity of the vessel when it is influenced by large environmental forces. Consequently, the berthing scheme in this thesis tries to redefine the most common methods in literature today, by avoiding the use of position references in surge close to the quay.

1.2.2 Assumptions and prerequisites

The velocity of operation of the milliAmpere ferry will be considered close to zero, and will in practice never exceed the upper speed limit of dynamic positioning applications (roughly $2\,\mathrm{m\,s^{-1}}$ [Fossen, 2021]). The first-order wake force consists of two parts: One force in $\{n\}$ decomposed in x^n and y^n, which is further rotated to $\{b\}$, as well as one moment influencing heading only. Full information regarding the quay structure at which the berthing operation takes place is assumed to be known in advance. Lastly, the milliAmpere ferry is meant to dock head-on towards the quay, and not laterally as exemplified in fig. 1.3a. Roll-on roll-off vessels, e.g. car ferries, dock in a similar fashion.

One prerequisite throughout the thesis is that the DP system onboard the milliAmpere ferry yields a satisfactory closed-loop behavior. This DP system is used during simulations, as well. Consequently, it will not be tuned or altered in any way in this work, neither during the validation task, the berthing task nor to improve behavior when the milliAmpere ferry is influenced by wave forces and moments. Tuning of the DP system will be left as future work. The same applies to the thrust allocation algorithm and the reference model in the guidance system.

1.3 About the milliAmpere ferry

The milliAmpere ferry, depicted in fig. 1.1, serves as a platform for experimentation and validation in the Autoferry project. This is a cross-disciplinary project which combines autonomy, communication, cyber security and risk management, among others [NTNU, n.d.]. The research project is motivated by a hypothesis that autonomous ferries and other, manned marine vessels can operate safely together in urban water channels and similar confined waters. The goal of the research with the milliAmpere ferry is to develop autonomous ferries for transport of people, bicycles, etc. in urban water channels. The specifications of the milliAmpere ferry are shown in table 1.1, while a sketch of the waterline footprint is depicted in fig. 1.2.

Figure 1.1: The milliAmpere ferry moored to a quay at Brattørkaia, depicted by the author on April 19, 2021.

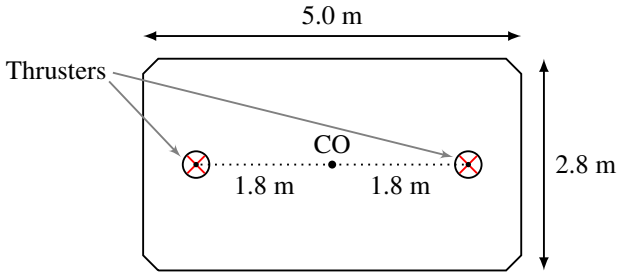

Figure 1.2: The waterline footprint of the milliAmpere ferry. The positions of the azimuth thrusters are marked with red crosses, and CO denotes the center of origin of the ferry.

Specifications	
Length	5.0 m
Width	2.8 m
Position and heading reference system	Vector™ VS330 GNSS
Thrusters	Two azimuth thrusters
Thruster locations	1.8 m aft and fore of the center of origin, along the center line
Obstacle detection	Velodyne Puck VLP-16 LIDAR Sensor, four mounted short range ultrasonic distance sensors (two aft and two fore)

Table 1.1: The milliAmpere ferry specifications. Courtesy of Bitar et al. [2020] and Martinsen et al. [2020]

The milliAmpere ferry uses a Vector™ VS330 Global Navigation Satellite Systems (GNSS) Receiver for position and heading data. This dual antenna GNSS receiver has real-time kinematic (RTK) capabilities [Hemisphere GNSS, Inc., 2019], with modern RTK receivers achieving a position accuracy in the order of magnitude of centimeters [Fossen, 2021]. The milliAmpere ferry has mounted four short range ultrasonic distance sensors, as well: two aft and two fore [Martinsen et al., 2020], that may be utilized during berthing of the vessel.

1.4 Validation of simulator models

Sargent [2010] presents four basic approaches for validation of a given simulator model:

- The team in charge of developing the model, i.e. the model development team, decides whether a simulator model is valid.

- A joint team, consisting of the user(s) of the model and the model development team, decides the validity of the model.
- An independent third party, with thorough understanding of the purpose of the simulator model, is used for validation.
- Determining a set of (subjective) weights for different aspects or parts of the validation process, with a scoring model yielding the final result.

These different approaches all have strengths and weaknesses. Sargent [2010] discusses five main disadvantages regarding the latter scoring model approach: This subjective approach is often presented as being objective; the subjectivity arises when choosing the weights; the best model may have defects that still need improvement; the scores of a model may lead to over-confidence, and lastly; the scores may be used to argue that one model is better than another. Nevertheless, this is the approach taken in this thesis, albeit the disadvantages will be further discussed in section 7.2.

One important aspect to keep in mind is that a model with sufficient accuracy for the experimental conditions, does not necessarily indicate that the model is valid in the whole applicable domain. The applicable domain being, in the case of the milliAmpere ferry, the possible control schemes and scenarios in which the ferry may be simulated and tested. Therefore, this thesis addresses the most favorable and least favorable model changes, not the best and worst model changes. Moreover, the main goal of the validation task is to highlight possible subsystems in the simulator which may need further validation.

1.5 The concepts of berthing and docking

In general, docking is a demanding task for human operators, and is one of the frequently performed operations of ferries, container ships and other marine crafts connected with the highest risk. Automatic methods are thus a necessity, and even a partly automated docking or berthing method may relief the crew of marine crafts. The terms *berthing* and *docking* are often used in the literature, and one distinction between these terms will be presented next. The docking process may be said to consist of four phases:

1. Navigation through a port or similar confined waters towards the berth position, which often involves a trajectory tracking/path following scheme and collision avoidance.
2. Berthing the vessel, i.e. closing the final few meters between the vessel and the quay structure.
3. Detecting when the fenders aboard the vessel make contact with the fenders mounted on the quay structure.
4. Keeping the vessel in the correct pose for mooring to take place, and the system to shut down.

Examples of the second phase, the berthing phase, is illustrated in fig. 1.3. In terms of docking of USVs, each phase utilizes different technologies, some which may be more refined and mature than others. In addition, the first two phases in particular may be those proving to be the most challenging. A literature review of marine craft docking and berthing methods in general will be given in section 3.6. Articles and work regarding docking and berthing of the milliAmpere ferry in particular is presented in section 4.3.

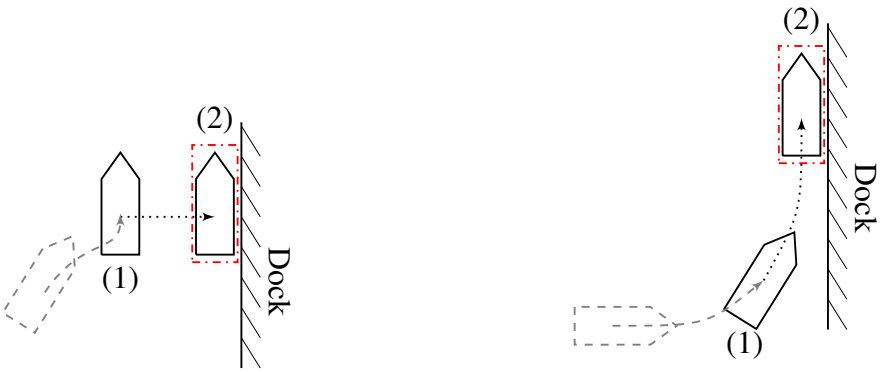

(a) Example of berthing of a fully actuated vessel. **(b)** Example of berthing of an under-actuated vessel.

Figure 1.3: The concepts of berthing a surface vessel. After having navigated the vessel through a port (denoted by the gray, dotted position), the goal is to move the vessel from position (1) to position (2). The designated berth position is marked as a dashed, red rectangle. Courtesy of Knudsen [2020].

1.6 Contribution of the thesis

Most research on docking or berthing of marine surface crafts utilize position references from a third degree reference model, such a model implemented in the milliAmpere system is presented in eq. (4.10) To the author's knowledge, this work is one of the very few works using a velocity reference in one degree of freedom, while attempting to attain position control in the other degrees of freedom. Insight in how different schemes work (gained through experimental testing) would increase knowledge on what scheme works best, depending on e.g. which environmental forces are present, the size of the vessel, etc.

The contribution of this thesis may then be summarized as three main parts: (1) Yield pointers to which models in the milliAmpere simulator in need of further refinement and tuning; (2) implement wave models relevant for the environment in which the milliAmpere ferry normally operates; (3) to regard the berthing scheme as a proof of concept, or lay the foundation for future work and improvements before a proof of concept is ready.

1.7 Outline

The outline of the rest of the thesis is listed below.

- chapter 2 presents the notation and equations of motion for marine crafts, as well as the models for wave forces and moments implemented as the second main task of this thesis.
- chapter 3 gives an introduction to unmanned surface vessels, focusing on USVs in harbors and ports. Marine crafts influenced by environmental forces and moments and how these may be counteracted, will also be presented.
- chapter 4 presents the milliAmpere ferry, and the simulator models relevant for the validation task.
- chapter 5 summarizes the first task of the thesis, regarding validation and tuning of the mathematical models in the milliAmpere simulator.
- chapter 6 presents the berthing scheme developed through the specialization project and this master's thesis. In addition, summaries of the bumpless transfer and gain-scheduling techniques are given, yielding context for future work.
- chapter 7 presents the results from the three main tasks, and discusses these in further detail.
- chapter 8 concludes the thesis, and presents proposals for the continuation of the work.

Chapter 2

Mathematical modeling

This chapter presents the mathematical maneuvering model often used for simulation of marine surface vessels, and various definitions regarding motion control. In addition, the models of wave forces implemented during this thesis will be presented. Lastly, a short summary of various wave filter techniques will be presented. This is done in order to highlight other means of including the effects of wave forces and moments.

Sections 2.2 and 2.3 are based upon chapter 3 in Knudsen [2020]. The 3 degrees of freedom (3DOF) equations of motion are the same, albeit this chapter will go more in-depth on the model parameters and notation.

2.1 Introduction and preliminaries

Throughout the thesis, the notation of SNAME [1950] for marine crafts will be used, similar to the works of Fossen [2011, 2021]. This notation will be presented next, in the context of 3DOF motions. Heave, roll, and pitch will not be included.

2.1.1 Reference frames

Reference frames are used for analysis of the motion of marine crafts. Two common Earth-centered coordinate frames are the Earth-centered inertial (ECI) frame and the Earth-centered Earth-fixed (ECEF) reference frame [Fossen, 2021]. The former is a non-accelerating reference frame with origin at the center of the Earth, and the axes fixed in space. The ECI frame is used for terrestrial navigation and inertial navigation systems (INSs). The origin of the ECEF frame is fixed at the center of the Earth, while the axes rotate relative to the ECI frame. The ECEF frame is used for global navigation (e.g. intercontinental shipping). Consult figure 2.2 in Fossen [2021] for a graphical overview of the ECI and ECEF frames.

When studying USVs and control systems, a normal assumption is flat Earth navigation [Fossen, 2011]. This implies that the longitude and latitude of the USV should be close to constant, i.e. the marine craft operates in a small area. A tangent plane fixed to the

surface of the Earth is then used for navigation. This geographic reference frame is normally denoted North-East-Down (NED), and abbreviated as $\{n\}$. In the $\{n\}$ frame, the x_n axis points towards true north, the y_n axis pointing towards east and the z_n axis pointing downwards, normal to the surface of Earth. It can be assumed that the $\{n\}$ frame is inertial, given that the rotation of the Earth is neglected [Fossen, 2011]. The result of this is that Newton's laws of motion apply. An alternative to the NED frame is the right-handed East-North-Up reference frame. Both frames are commonly used in control applications, albeit $\{n\}$ will be used in this thesis.

The BODY frame, denoted $\{b\}$, is fixed to the marine craft [Fossen, 2011]. The x_b axis is going from aft to fore, the transverse axis y_b points towards starboard and the normal axis z_b is pointing from the deck to the keel of the marine craft [SNAME, 1950]. Motions along the x_b and y_b axes are commonly referred to as surge and sway, while rotation about the z_b axis is called yaw.

2.1.2 Position and velocities

Applying the convention presented in Fossen [2011], with $\mathbb{R}$ denoting the set of real numbers and $\mathbb{S} = [-\pi, \pi)$ denoting the set of angles, the generalized position vector is defined as:

$$\boldsymbol{\eta} = \begin{bmatrix} x^n & y^n & \psi \end{bmatrix}^\top \in \mathbb{R}^2 \times \mathbb{S} \tag{2.1}$$

The generalized position vector is given in the $\{n\}$ frame, and is also called the *pose* of the marine craft [Fossen, 2021].

Furthermore, the vectors $\boldsymbol{\nu}$, $\boldsymbol{\nu}_r$, and $\boldsymbol{\nu}_c$ denote the velocity vector, the relative velocity vector and the generalized ocean current velocity vector, respectively. The three velocity vectors are all decomposed in the $\{b\}$ frame [Fossen, 2011]. The elements in the velocity vectors are denoted the following way:

$$\boldsymbol{\nu} = \begin{bmatrix} u & v & r \end{bmatrix}^\top \in \mathbb{R}^3 \tag{2.2a}$$

$$\boldsymbol{\nu}_c = \begin{bmatrix} u_c & v_c & 0 \end{bmatrix}^\top \in \mathbb{R}^3 \tag{2.2b}$$

$$\boldsymbol{\nu}_r = \boldsymbol{\nu} - \boldsymbol{\nu}_c = \begin{bmatrix} u_r & v_r & r_r \end{bmatrix}^\top \in \mathbb{R}^3 \tag{2.2c}$$

In eq. (2.2a), u and v is the linear velocity in the x_b and y_b direction, respectively. These are often referred to as the surge and sway speed. Likewise is r the angular velocity about z_b, commonly referred to as the yaw rate. For the element $\boldsymbol{\nu}_{c,3}$ in eq. (2.2b) to be zero, the ocean current must be considered irrotational and constant in $\{n\}$ [Fossen, 2011]. Furthermore, when neglecting motion in heave, roll and pitch, the ocean current becomes a 2D current in the horizontal plane. If no ocean current is present, the two velocity vectors $\boldsymbol{\nu}_r$ and $\boldsymbol{\nu}$ will be equal. Lastly, with $U = \sqrt{u_r^2 + v_r^2}$ denoting the forward horizontal speed of a marine surface vessel, fig. 2.1 shows the geometrical relationship between the

heading angle ψ, the course angle χ and the crab angle β_c. This relationship is given by the expression [Fossen, 2011]:

$$\chi = \psi + \beta_c \tag{2.3}$$

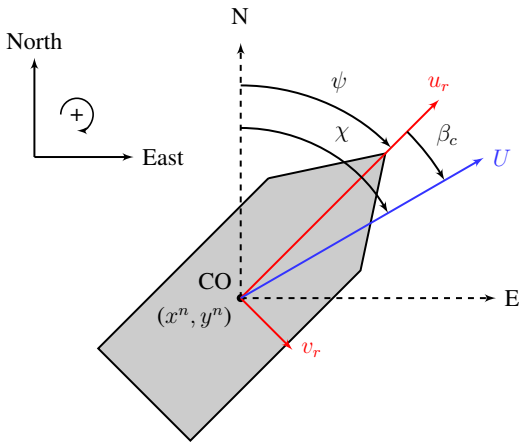

Figure 2.1: The north position x^n and the east position y^n of a marine surface vessel influenced by an ocean current. CO denotes the center of origin of the vessel, u the surge speed, v the sway speed and U the forward horizontal speed of the vessel. Rotation about the z_n axis is positive clockwise.

2.1.3 Configuration space and workspace

A configuration space contains all possible positions and orientations that a marine craft may achieve. The configuration space can be uniquely described using an n-dimensional vector of generalized coordinates [Fossen, 2011], this thesis will focus on a 3-dimensional ($n = 3$) configuration space. Similarly, control systems for marine surface crafts need a workspace of m dimensions in order to specify the control objective [Fossen, 2011].

2.2 The 3 DOF equations of motion

When deriving the widely-used 3 DOF nonlinear maneuvering model, it's assumed that the fluid through which the marine craft moves is ideal, the masses of the marine craft are uniformly distributed and the marine craft owns the port-starboard symmetry [Liu et al., 2016].

Following these assumptions, as well as the notation presented in section 2.1, the 3 DOF maneuvering model used for simulations of surface vessels influenced by environmental forces (ocean current, wave and wind forces) is given by Fossen [2011, 2021]:

$$\dot{\boldsymbol{\eta}} = \boldsymbol{R}_b^n(\psi)\boldsymbol{\nu} \tag{2.4a}$$

$$\boldsymbol{M}\dot{\boldsymbol{\nu}}_r + \boldsymbol{N}(\boldsymbol{\nu}_r)\boldsymbol{\nu}_r = \boldsymbol{\tau} + \boldsymbol{\tau}_{\text{wind}} + \boldsymbol{\tau}_{\text{wave}} \tag{2.4b}$$

The vector $\boldsymbol{\tau} \in \mathbb{R}^3$ denotes the control inputs. $\boldsymbol{\tau}_{\text{wave}} \in \mathbb{R}^3$ is the vector of wave-induced forces and moments, likewise the vector $\boldsymbol{\tau}_{\text{wind}} \in \mathbb{R}^3$ contains the wind forces and moments. All three aforementioned vectors are given in $\{b\}$. The wind models implemented in the milliAmpere simulator will be briefly presented in section 4.1.2.

A principal rotation is a rotation about one axis only [Fossen, 2021]. The principal rotation about the z axis from $\{b\}$ to $\{n\}$ is defined as:

$$\boldsymbol{R}_b^n(\psi) = \begin{bmatrix} \cos(\psi) & -\sin(\psi) & 0 \\ \sin(\psi) & \cos(\psi) & 0 \\ 0 & 0 & 1 \end{bmatrix} \tag{2.5}$$

and is positive when rotating clockwise.

With $\boldsymbol{M}_{RB}$ denoting the rigid-body mass matrix and $\boldsymbol{M}_A$ denoting the added mass matrix, $\boldsymbol{M} = \boldsymbol{M}_{RB} + \boldsymbol{M}_A$ in eq. (2.4b) denotes the mass matrix. It may be challenging to distinguish the elements belonging in the rigid-body mass matrix from those in the hydrodynamic added mass matrix. For control purposes, using the collective matrix $\boldsymbol{M}$ has no significant impact on the behavior of the control system. In addition, using $\boldsymbol{M}$ simplifies the design of the control system.

For readability purposes, the matrix $\boldsymbol{N}(\boldsymbol{\nu}_r)$ in eq. (2.4b) is a collective term defined as:

$$\boldsymbol{N}(\boldsymbol{\nu}_r) = \boldsymbol{C}_{RB}(\boldsymbol{\nu}_r) + \boldsymbol{C}_A(\boldsymbol{\nu}_r) + \boldsymbol{D}(\boldsymbol{\nu}_r) \tag{2.6}$$

Here, $\boldsymbol{C}_{RB}(\boldsymbol{\nu}_r)$ denotes the rigid-body Coriolis and centripetal matrix, and $\boldsymbol{C}_A(\boldsymbol{\nu}_r)$ the added mass Coriolis and centripetal matrix. $\boldsymbol{D}(\boldsymbol{\nu}_r)$ is the hydrodynamic damping matrix. The sum of $\boldsymbol{C}_{RB}$ and $\boldsymbol{C}_A$ is the collective Coriolis and centripetal matrix, denoted $\boldsymbol{C}(\boldsymbol{\nu}_r)$. As with the mass matrices $\boldsymbol{M}_{RB}$ and $\boldsymbol{M}_A$, distinguishing the elements of the rigid-body and added mass Coriolis and centripetal matrices yield no different result in practical control applications, and thus the collective matrix $\boldsymbol{C}$ is used.

In order to implement the ocean current model from Knudsen [2020] correctly in the simulator, the kinetics model given in eq. (2.4b) is altered slightly [Fossen, 2021]:

$$\dot{\boldsymbol{\nu}} = \begin{bmatrix} rv_c \\ -ru_c \\ 0 \end{bmatrix} + \boldsymbol{M}^{-1}(\boldsymbol{\tau} + \boldsymbol{\tau}_{\text{wind}} + \boldsymbol{\tau}_{\text{wave}} - \boldsymbol{N}(\boldsymbol{\nu}_r)\boldsymbol{\nu}_r) \tag{2.7}$$

In the vector on the far left on the right-hand side of the expression, r denotes the yaw rate, while u_c and v_c denotes the longitudinal and lateral component of the ocean current velocity, respectively.

2.3 Wave forces and moments

The environmental forces and moments may have a significant impact in precision systems, examples of such are automatic berthing and docking systems. Next, the wave force models implemented during the second task of this thesis will be presented.

2.3.1 The wave models

Wave forces are caused either by wind forces disturbing the ocean surface, as a result of the tides or as a combination of both. Two-dimensional wave spectra caused by wind forces can be said to consist of two parts: One part directly influenced by local wind conditions, and a second part that is generated by far-away winds. The latter part has propagated from areas far from the location of the marine vessel. As such, the sea state at any place is a combination of generated components of the two aforementioned types [Janssen, 2004].

One important aspect to consider after berthing a vessel regarding wave forces and moments, is that moored vessels experience a net wave force when each ocean wave hits the vessel. This may lead to large mooring line tensions, especially on large offshore vessels influenced by extreme conditions on the open sea [Hsu and Blenkarn, 1972].

The wave forces and moments $\boldsymbol{\tau}_{\text{wave}}$ in eq. (2.4) consist of one slowly-varying and one oscillatory component. In general, $\boldsymbol{\tau}_{\text{wave}}$ can be split in two parts using the superposition principle:

$$\boldsymbol{\tau}_{\text{wave}} = \boldsymbol{\tau}_{\text{wave1}} + \boldsymbol{\tau}_{\text{wave2}} \tag{2.8}$$

where $\boldsymbol{\tau}_{\text{wave1}}$ denotes the first-order wave-induced forces, and $\boldsymbol{\tau}_{\text{wave2}}$ denotes the second-order wave-induced forces. According to Fossen [2021], the former will often be observed as zero-mean oscillations, while the latter is observed as slowly-varying nonzero drift forces.

First-order wave-induced forces and moments

First-order wave-induced motions $\boldsymbol{\eta}_{\text{wave}}$ occurring due to influence of $\boldsymbol{\tau}_{\text{wave1}}$ may be modeled as linear state-space models, one model for each DOF i. Fossen [2021] recommends using the JONSWAP spectrum, which assumes a finite depth of the water. Furthermore, it's assumed that the wind producing the waves has traveled a limited distance of open water. This wave spectrum is ideal for simulations of non-fully developed seas, i.e. not fit for conditions occurring during a storm that has raged for a long time. The model as a whole is summarized in Fossen [2021, pp.279–281], where $\boldsymbol{\eta}_{\text{wave}}$ is added to the navigation model to estimate and compensate for the wave influence in the measurements. One drawback of the state-space model is that the intended use is simulations of operations at open seas, and for closed-loop analysis only. In addition, a model-based navigation system is needed, which is not the case for the milliAmpere simulator.

Fossen [2021] mentions response amplitude operators (RAOs) as an alternative to state-space models, either motion RAOs or force RAOs. The former computes the first-order wave-induced positions by low-pass filtering the generalized wave forces $\boldsymbol{\tau}_{\text{wave1}}$, while the latter relates wave amplitudes to first- and second-order wave-induced forces using a wave spectrum. A drawback using RAOs is the need of a hydrodynamic program computing RAO tables, which considers the geometry of the ship hull to determine the wave forces [Fossen, 2021].

This thesis tries to replicate realistic physical first-order wave-induced forces as they may appear in confined waters and ports. The state-space model is typically used to compensate for the influences of wave forces and moments in the navigation system. What this thesis aims to model is the wave forces and moments themselves, and not the influence these forces and moments have in the navigation system. Thus, the first-order wave-induced forces will be modeled as simplified wake forces. These oscillating forces are assumed to originate from nearby vessels in motion, may have a period of 1–2 seconds and dies out quite rapidly. An example of such is depicted in fig. 2.2.

Figure 2.2: Example of wake waves from a marine surface craft in motion.
Photo: Petr Kratochvil, free access.

In general, the total wake force acting in surge and sway, and the wake moment acting in yaw, follow time-dependent functions on the form:

$$g_{\text{w}}^{n}(t) = Ae^{-at}\cos\left(ft + \varphi\right) + Be^{-bt}, \qquad t \geq 0 \tag{2.9}$$

The wake force acting in surge and sway is originally given in $\{n\}$. Consequently, this force needs to first be decomposed in x^n and y^n, using a desired wave encounter angle β, before being rotated to $\{b\}$. Let $W_{xy}^{n}(t)$, given in $\{n\}$, be a function on the general form defined in eq. (2.9), and denoting the total wake force which is meant to act in surge and

sway. $W_{xy}^n(t)$ is decomposed to force components $W_x^n(t)$, acting in x^n, and $W_y^n(t)$, acting in y^n, using:

$$W_x^n(t) = W_{xy}^n(t)\cos\beta$$
$$W_y^n(t) = W_{xy}^n(t)\sin\beta$$

From here, $W_\psi(t)$ denotes the moment acting in ψ and the elements of the vector of first-order wave-induced forces and moments will be denoted $\boldsymbol{\tau}_{\text{wave1}} = \begin{bmatrix} X_{\text{wave1}}^b & Y_{\text{wave1}}^b & N_{\text{wave1}}^b \end{bmatrix}^\top$. $\boldsymbol{\tau}_{\text{wave1}}$ is given in $\{b\}$, and the wake forces are rotated to $\{b\}$ using:

$$\boldsymbol{\tau}_{\text{wave1}} = \begin{bmatrix} X_{\text{wave1}}^b \\ Y_{\text{wave1}}^b \\ N_{\text{wave1}}^b \end{bmatrix} = \boldsymbol{R}_n^b(\psi) \begin{bmatrix} W_x^n(t) \\ W_y^n(t) \\ W_\psi(t) \end{bmatrix} \tag{2.10}$$

These forces and moments are added to the kinetics model, defined by eq. (2.4b), in the simulator. In eq. (2.10), $\boldsymbol{R}_n^b(\psi) = \boldsymbol{R}_b^n(\psi)^{-1}$ denotes the inverse of the rotation matrix defined in eq. (2.5), i.e. the principal rotation from $\{n\}$ to $\{b\}$. Plots of the first-order wave-induced force $W_{xy}^n(t)$ is shown in fig. C.1, likewise is the moment affecting yaw shown in fig. C.2. From here, it's implicit that the wake forces are time-dependent.

Second-order wave-induced forces and moments

The dynamics of the wave-drift forces $\boldsymbol{\tau}_{\text{wave2}}$ can be modeled as three slowly-moving random walk processes [Fossen, 2021]:

$$\dot{d}_i = w_{d_i}, \qquad i \in \{1, 2, 6\} \tag{2.11a}$$
$$\boldsymbol{\tau}_{\text{wave2}} = \begin{bmatrix} d_1 & d_2 & d_6 \end{bmatrix}^\top \tag{2.11b}$$

The input w_{d_i} to the random walk d_i is a zero-mean Gaussian white noise process, i.e. a stationary random and normal process with a mean value of zero and a constant spectral density function [Brown and Hwang, 2012]. In eq. (2.11b), the element d_i for DOF $i \in \{1, 2, 6\}$ consists of both the dynamic part defined in eq. (2.11a) and a stationary component. Plots of the second-order wave drift forces and moments are shown in fig. C.3.

2.3.2 Wave filtering

This next section briefly summarizes other basic alternatives for including effects from wave-induced forces and moments, apart from modeling the forces as presented in the previous section. One common way to hinder the wave-frequency motions entering the feedback loop is to implement a wave filter. Such a wave filter is added to the navigation system, in order to estimate and remove the impact the wave forces and moments have

on the true states of the system. A literary study regarding DP systems and wave filtering will be presented in section 3.5.1.

The Kalman filter is arguably the most famous model-based state estimation algorithm, first presented by Kalman [1960]. It may be used for e.g. estimation of the low-frequency motions of a vessel, which is influenced by wave forces and moments. Kalman filtering is often used in inertial navigation systems, integrating inertial measurement units (IMUs), accelerometers and other sensors with satellite navigation systems. Consult e.g. Fossen [2021] for a thorough review of these applications. The milliAmpere simulator doesn't have such a navigation system, and is consequently not fit for state estimation as of now.

Other techniques, as presented by Fossen [2021], include using a low-pass filter, a low-pass filter cascaded with a notch filter, a nonlinear observer for the estimation of the wave encounter frequency when U is non-constant, as well as a method using the Fast Fourier Transform (FFT). The latter is not an alternative for the milliAmpere simulator, as the best results from the FFT method use the heave or pitch response of the vessel, as well as assuming both forward speed U and desired wave encounter angle β to be constant. This leaves low-pass filtering, alternatively cascaded with a notch filter, as the most beneficial option for future wave filtering in the milliAmpere system. The purpose of the cascaded notch filter is to let frequencies containing ship dynamics through the low-pass filter. This is necessary if the wave frequencies and the frequencies of the ship dynamics are similar. For large vessels with high time constants, e.g. oil tankers, this is hardly the case, but may be relevant for the small milliAmpere ferry.

Chapter 3

Unmanned surface vessels

The Norwegian mainland has a coastal line of 29 775 kilometers and a total shoreline, which also includes all islands, of roughly 103 000 kilometers [Thorsnæs, 2020]. As a result of the Norwegian marine and offshore industry, unmanned surface vessels (USVs) are of great interest in various industries and for various applications. This may result in Norwegian high-tech businesses being more competitive on the international maritime markets, as well as prove vital to the digitalization process of the maritime industries.

Next, an introduction to the field of USVs will be given. The main motivation is to highlight challenges and solutions regarding USVs in ports, as well as USVs influenced by environmental forces and moments.

3.1 Introduction

The term *unmanned surface vessel* is frequently used in this thesis. A suitable definition of a USV is given by Breivik [2010]:

Definition 3.1.1 (Unmanned surface vessel)**.** An unmanned surface vessel operates in a variety of cluttered environments without any human intervention, exhibiting highly nonlinear dynamics.

Similarly, Breivik [2010] defines a fully autonomous USV as:

Definition 3.1.2 (Fully autonomous unmanned surface vessel)**.** A fully autonomous unmanned surface vessel is a marine surface vehicle able to both govern its own decisions, as well as making those very same decisions, from launch to recovery.

The difference between these two terms may be that the former uses e.g. manually predefined waypoints during operations, while the latter autonomously instead decides the best waypoints during runtime. The research field of USVs, also called autonomous surface vehicles (ASVs), is in focus and rapidly expanding. The reasons for this increase of interest are many, some of which are listed below:

- Increase in computational power and its reduced cost.
- Availability to large data sets, e.g. weather data.
- Reliable and powerful wireless communication technology.
- Increased focus on sustainability, e.g. The European Green Deal, and the transition from fossil fuel to renewable energy.
- Reduced fuel consumption, by the use of optimal control.
- More reliable sensor systems.
- Easier access to GNSS data.
- Increased safety of ship operations.
- Developing decision-support systems for human operators, enabling large and effective unmanned operations overseen by a limited number of people.

3.2 USV applications

Applications of USVs, available both today and in the future, include mapping of the ocean and the ocean floor, tracking of marine life, minesweepers and firefighting. Such missions are examples that can be summarized as being dirty, dull and dangerous [Breivik, 2010], and are great examples of the potential of USVs. Other applications mentioned are autonomous ferries, cruise ships and container ships.

Similarly, Devaraju et al. [2018] defines four potential main applications for USVs, depicted in fig. 3.1. The different sub-applications under *Cargo transport* may be challenging to distinguish. However, short-sea cargo transport (sometimes referred to as short-sea shipping) can be used in terms of transportation of goods, passengers and/or vehicles along fjords and coastal lines within a country or continent. Consult Paixão and Marlow [2002] for a more in-depth discussion of the term. Assuming deep- and short-sea cargo may be viewed as opposites, deep-sea cargo can be used in terms of intercontinental cargo transport and when crossing open seas (e.g. the Atlantic ocean). Lastly, the term inland shipping covers cargo transport on rivers and inland lakes.

Confined waters with stationary and especially moving objects to avoid, may be the most challenging environment in which USVs operate. Most docking and berthing operations take place in such confined waters, e.g. ports, canals and rivers. Such environments are often crowded with marine crafts, people, and structures on land and in the water. An accident or hazardous behavior in such an environment could be devastating, potentially leading to loss of lives and income, worsened reputation of a responsible part and fewer future missions for the vessel or corporation in charge of an accident.

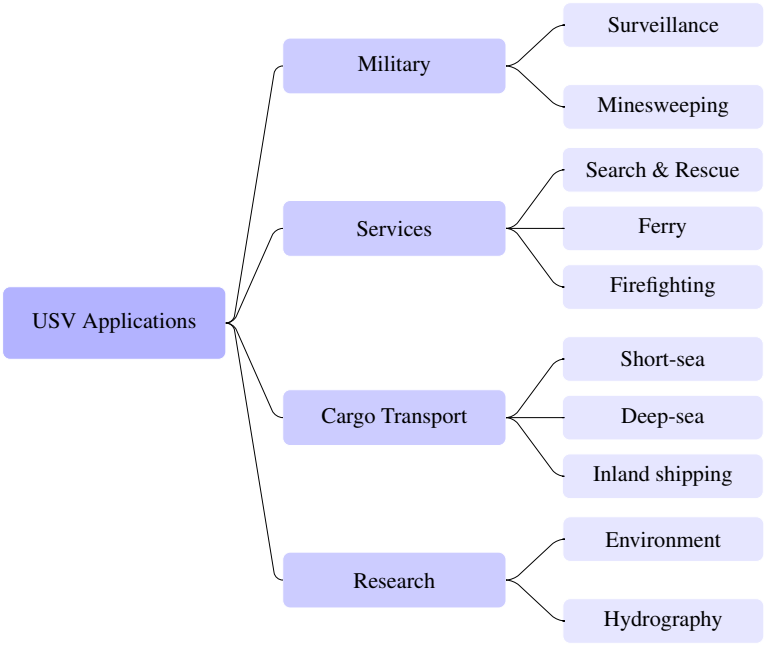

Figure 3.1: Four potential main applications for USVs, with more specific examples listed on the far right. Courtesy of Devaraju et al. [2018].

3.2.1 Examples of USVs today

The following paragraphs present a selection of autonomous marine vessels, with various applications.

The Saildrone USVs

The Saildrone USVs from the California-based company Saildrone, Inc. are meant for ocean exploration. The saildrones are towed in and out of the harbor, but utilizes wind forces only for propulsion in the area of operations. The newest vessel of the fleet is the ”Saildrone Surveyor”, a 22 meter long vessel covering 100 kilometers per day on average [Saildrone, Inc., 2021]. A smaller vessel from the same company, a 7 meter long ”Saildrone Explorer”, was the first USV to cross the Atlantic Ocean in both directions (first west-to-east and then east-to-west). During the former trip, the vessel also set the record for the fastest autonomous Atlantic crossing [Saildrone, Inc., 2019]. Both Saildrone models use solar energy to power the onboard computers and navigation systems. The Saildrone USVs may be said to belong to the *Research* application depicted in fig. 3.1.

Yara Birkeland

Yara Birkeland is a project involving Yara and Kongsberg which started in 2017, with the goal of building the first zero-emission and autonomous container ship in the world [Yara, 2020]. The ship, which is powered by batteries only, is meant to sail from the Yara plant in Porsgrunn to the ports in Brevik and Larvik, replacing 40 000 journeys with trucks

each year [Yara, 2018]. The main motivation of the project is reducing emissions and improving road safety. Yara Birkeland is depicted in fig. 3.2. This type of autonomous container ships covers the *Cargo transport* application in fig. 3.1, more specifically the *Short-sea cargo transport*.

Figure 3.2: Yara Birkeland depicted in April, 2020[1].

Bastø Fosen VI

In early February, 2020, the Norwegian car ferry Bastø Fosen VI successfully completed the world's first automatic ferry transit from dock to dock, with both passengers and cars onboard [Kongsberg Maritime, 2020]. Undocking from Horten port, the transit as well as the docking at Moss port were all fully autonomous operations. The system was, as of February 2020, not fully autonomous, in the regard that the bridge was fully manned. If obstacles or other ferries are detected to be on collision course, the crew is meant to take full control of the ferry. During trials without passengers in December, 2019, the ferry consistently arrived within two seconds of the schedule. The goal of the project is reduced greenhouse gas emissions and to improve passenger safety, as well as accomplish greater schedule accuracy and better logistics. Bastø Fosen VI covers the *Ferry* section of the *Service* application in fig. 3.1

3.3 Challenges for USVs

USVs do not only have vast and groundbreaking potentials, several challenges present themselves. Next, various types of challenges will be presented.

3.3.1 Technical challenges

Liu et al. [2016] presents an in-depth technical review of USV challenges, and a summary of the current state and future perspective of USV research. Regarding USV challenges,

[1]Downloaded February 24, 2021. Free access from `https://www.yara.com/news-and-media/media-library/image-library/`.

it's emphasized that the future research progress of USVs depends on whether fully autonomous USVs are developed, see definition 3.1.2.

Breivik [2010] focuses on collision avoidance, proposing sensor solutions providing local information to the vessel as one bottleneck for further reasearch and development of USVs. Other challenges mentioned are access to global information about the environment in which the marine craft operates, as well as the development of algorithms for making the USVs capable of performing proactive and reactive planning. The latter is needed in order to avoid obstacles. Legal framework and guidelines are also highlighted as challenges for future development and refinement of USV technology, as well as maintenance logistics.

Similarly, Caccia [2006] emphasizes four basic research issues regarding USVs:

1. Identification of practical USV dynamics models.
2. Challenges regarding guidance, navigation and control systems, further divided into:
   (a) Control in the horizontal plane
   (b) Trajectory tracking and path following.
   (c) Cooperative motion control.
3. Mission control, how human supervisors may interact with a USV during operations.
4. Legal challenges.

Furthermore, other types of challenges USV research are likely to face are political and social challenges. These include the opinion of the public and politicians regarding leaving important (and in worst-case scenarios, life-changing) decisions to a system they may not fully comprehend. Optimizing user experience design for people of all ages is yet another challenge needed to be resolved.

3.3.2 COLREGs compliance

The International Regulations for Preventing Collisions at Sea, commonly referred to as the COLREGs (COLlision REGulations), specify the types of maneuvers a ship should take when risking collision with another ship [Kuwata et al., 2014]. The development of unmanned systems able to follow the COLREGs is highly necessary, as is making those systems able to manage situations where the surrounding vessels do *not* obey the COLREGs. The latter is needed for fault tolerant behavior.

Benjamin and Curcio [2004] points out that the COLREGs depend on the human common sense to both determine if a given situation applies, as well as show flexibility in

the actions if e.g. several rules apply at once. In order to provide the COLREGs to autonomous systems, this effectiveness and flexibility must be captured. Regarding effectiveness, Benjamin and Curcio [2004] highlights that situations where several rules apply, or where one rule is compromising mission objective, must be handled properly, smoothly and with compromise when possible.

3.3.3 Ports and harbors

The number of governmental harbors in Norway, serving both the maritime industries as well as the local communities, is approximately 600 [Norwegian Coastal Administration, 2016]. Regarding berthing of USVs, port infrastructure is an important aspect to consider in order to fully exploit the advantages of USVs. Communication between the autonomous vessel and the port management should be exchanged instantaneous, non-verbally, automatically and in real-time. Furthermore, infrastructure must be made available for autonomous mooring, maintenance and battery charging facilities. Other types of infrastructure needed include automatic loading and unloading of cargo. These challenges are all vital to solve before the berthing process may be deemed fully autonomous [Devaraju et al., 2018].

Different berthing policies may also present themselves as useful, apart from the most standard first-come, first-served. What this particular policy incentives, is for a ship to sail at full speed towards the destination port. This leads to the consumption of enormous amounts of fuel for large vessels, and may result in ships being anchored for days before being designated a berth within the actual harbor.

To battle this, Alvarez et al. [2010] presents a mixed-integer programming simulation model. This model includes a function mapping the speed of a vessel to it's fuel consumption, the spatial configuration of the destination port, the travel time and distance from a given ship's origin to the destination port, among others. Case studies of three berthing policies were conducted in Alvarez et al. [2010]: (1) first-come, first-served; (2) standardized estimated arrival time; and (3) global optimization of speed berth, and equipment allocations. The latter policy yields the best results, reducing fuel consumption by 6 percent, reducing the number of cancellations, and reducing the average dwell time in the harbor.

3.3.4 Safety

The safety aspect close to the quay during berthing of USVs has not been part of the main focus of similar work, and safety is one important motivation behind the berthing scheme presented in this thesis. Thus, a brief introduction regarding safety of marine crafts in general will be given.

One may distinguish between different categories of safety; the safety of the environment (marine life, vegetation, etc.) in which the marine craft operates, the safety of the marine craft itself, the passengers and/or crew of the vessel, the safety of other structures and marine crafts nearby, as well as any combination of these.

As global trade is increasing, the marine traffic increases as well. One consequence of the marine traffic increase is severe accidents happening at a higher frequency. Severe accidents are accidents that render a ship unseaworthy, lead to ship breakdowns or result in serious damage or financial loss [Eliopoulou et al., 2016].

Compared to a DNV GL report studying the period 1999–2004, Eliopoulou et al. [2016] identified an increase in severe marine accidents of 30% in the period 2000–2012. 80% of marine accidents are attributed to human factors [Eliopoulou et al., 2016], although the paper pointing out that the practice regarding reporting ship accidents may have been improved compared to the previous DNV GL study.

Factors that may contribute to the increase in serious ship accidents include reduced maintenance and increased naval traffic due to large global trade [Eliopoulou et al., 2016]. Contrary to the increase of severe accidents during the years 2000–2012, lives lost at sea happens at a significantly reduced frequency [Eliopoulou et al., 2016] compared to the period 1999–2004.

3.3.5 Cyber security

Cyber security is yet another aspect regarding the safety of both manned and unmanned surface vessels. As modern-day ships depend on high-tech solutions in order to operate as intended, cyber security cannot be neglected.

In 2020, the world leading risk management and assurance company DNV GL and the maritime cyber security solutions provider Naval Dome performed penetration tests on a cargo ship without proper on-board cyber security solutions. The experts managed to alter the ship position shown on the radar display, turning machinery on and off, as well as override fuel control and steering [Csorba, 2020]. This exemplifies how vulnerable autonomous USVs in particular can be to malevolent actions, when no crew is available for safekeeping.

3.4 Guidance, navigation and control

The guidance, navigation and control (GNC) system is a vital part of marine crafts in general, and arguably the most important part of a USV. A GNC system consists of three subsystems; a guidance system, a navigation system and a control system.

The guidance system is tasked with computing the pose, velocity and acceleration references used by the control system. The goal of the control system is to calculate the control forces and moments needed, in order for the vessel to satisfy some control objective (e.g. minimizing fuel consumption, trajectory tracking or path following). The navigation system determines the pose, velocity and acceleration of the vessel, using e.g. GNSS measurements, inertial measurement units (IMUs) and other motion sensors [Fossen, 2021].

These three subsystems are often tightly connected, meaning that a flaw or imperfection

in one subsystem may ripple through the GNC system and lead to degrading performance overall [Liu et al., 2016].

A simplified sketch of the GNC system relevant for this thesis is shown in fig. 3.3. The main advantage of the wind feedforward term $\hat{\tau}_{\text{wind}}$, is that the integral term of the controller avoids integrating up the wind disturbance. One assumption for the wind feedforward term to function well, is that the wind forces and moments must be measurable [Balchen et al., 2016]. In other words, measurements of the wind speed and direction must be available. Furthermore, an accurate model of the wind forces and moments is needed [Fossen, 2021]. For more detailed GNC drawings, consult e.g. Fossen [2011, p.233] or Fossen [2021, p.290].

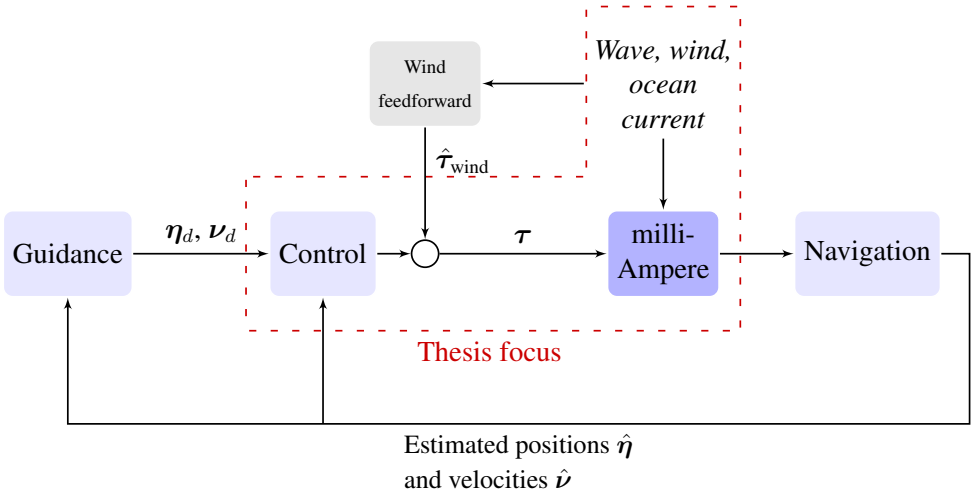

Figure 3.3: A block diagram showing the GNC subsystems and the signal flow between these. The milliAmpere ferry denotes the plant of the system, with the red box highlighting the focus of the thesis.

This thesis addresses the difference between trajectory tracking and path following when berthing or docking USVs, focusing on establishing a new scheme emphasizing path following. The following definitions are given:

Definition 3.4.1 (Trajectory Tracking)**.** Trajectory tracking is the simultaneous construction of a geometric path and the dynamic behavior of its path particle. Trajectory tracking inherently mixes the space and time assignments into one single assignment [Breivik and Fossen, 2005, p.627].

Definition 3.4.2 (Path Following)**.** Path following separates the construction of a geometric path and the dynamic assignment of its path particle. Path following has spatial localization as a primary objective, and the dynamic aspect as a secondary objective [Breivik and Fossen, 2005, p.627].

According to Breivik and Fossen [2005], trajectory tracking can be interpreted as an open loop, feedforward solution due to some a priori assumptions of the system. These assumptions are made to ensure feasibility. If no action is made to ensure feasibility when

something happens to the system, the path particle will be oblivious to the state of the actual particle. Path following, on the other hand, may be seen as a closed loop solution, where the path particle evolves according to the actual particle [Breivik and Fossen, 2005]. This makes path following more robust to unforeseen events, e.g. environmental disturbances, and is the motivation behind focusing on path following, and not trajectory tracking, in this thesis.

3.5 Dynamic positioning

The dynamic positioning (DP) system is a vital part of the berthing scheme presented in the thesis, as such a brief introduction to this field of study is given next. The main goal of a DP system is to control a marine surface vessel such that the vessel has a fixed position and heading, within a set error margin. This is achieved by the use of thrusters and propellers only [Fossen, 2021].

3.5.1 Dynamic positioning and wave filtering

The first DP systems were introduced during the 1960s. These systems used one conventional proportional-integral-derivative (PID) controller for each degree of freedom. In order to avoid wave-induced motion entering the feedback loop, the controllers were cascaded with low pass or notch filters [El-Hawary, 2000]. Such filters introduce a phase lag to the closed-loop system, resulting in poorer performance overall.

If the first-order wave-induced motions enter the feedback loop, this may result in an increase in both thruster wear-and-tear and fuel consumption. This is due to the control system trying to counteract every single wave disturbance, regardless of the magnitude or frequency of these waves. Consequently, techniques for suppressing wave-induced motion have been in focus since the earliest research on the subject of DP systems.

Balchen et al. [1976] designed an adaptive wave filter using a Kalman filter, and combined this with multivariable optimal control theory. Balchen et al. [1980] continued this work, adding ocean current estimation and feedforward from the wind force estimates, as well as conducting experimental sea trials. Saelid et al. [1983] improved the work further by adding a damping term to the mass-spring models of the high-frequency vessel model from Balchen et al. [1980], modified the low-frequency model structure, and presented and analyzed a wave frequency adaption algorithm.

Lindegaard [2003] introduced acceleration feedback in the DP controller in order to better compensate slowly-varying wave drift forces.

Hassani et al. [2012] presented a multiple model adaptive wave filter, which only relied on position and heading measurements, adapting the wave filtering to variations of the sea state. The main motivation was that previous work assumed the sea state to be constant during operations.

Værnø et al. [2019] compared three Kalman filters for four different DP control design models, using two test cases: the DP 4-corner test and a transient test, conducting both simulation tests and full-scale experiments.

3.6 Literary study of berthing and docking

Next, various articles regarding docking and berthing are presented. Docking articles focusing on fuzzy logic, deep learning or artificial neural network controllers, docking of underwater vehicles and space-related articles have been considered irrelevant for this thesis. The reason for these omissions being the focus on traditional control theory, and marine surface vessels.

Aune [2019] developed an autonomous docking system at a specific pier in Horten, Norway. The USV was meant to dock parallel to the pier, closing the last distance with velocity in sway direction only. A detection filter was used to determine when the USV had reached the desired position before docking could take place. Roll compensation for cancellation of wave excitations was implemented, as well. This approach is not possible to test in this thesis, as the mathematical model only considers 3 DOFs.

Kløvning [2020] studied how wind may affect the power consumption of a passenger ferry during berthing operations. 125 ship approaches in Molde port, Norway were conducted. Results indicated that wind speed above $5\,\mathrm{m\,s^{-1}}$ lead to an increase in power consumption, and that this increase may be close to linear with respect to wind speed. Limitations of the work include the inability to measure the direction of the wind, as well as disregarding several effects that a berthing ship may experience.

Shuai et al. [2020] proposed a method for maneuvering autonomous low-speed vessels towards a dock, steering the vessel along a pre-planned path using a line-of-sight algorithm. Collision avoidance was considered, as were the effects of environmental forces acting on the vessels.

Spange [2016] implemented a line-of-sight steering law for path-following towards the berth, before gliding the vessel to the berth position. Acoustic proximity sensors and a LiDAR were used for obstacle detection. The experimental platform was a small-scale and fully-actuated vessel model with spherical hull.

Abramowicz-Gerigk [2008] conducted an experimental study on the induced hydrodynamic forces generated by the thrusters and propellers on a large manned model of a twin-propeller ferry. The operations studied were berthing and unberthing close to a vertical quay wall, with motions in heave, roll and pitch being those of interest. The influence of both the water depth and the distance between the quay wall and ship side were studied, as were various interaction forces.

Mizuno et al. [2015] proposes a quasi real-time method for minimum-time approaching control for automatic berthing. The goal of the operation is to take a ship from one starting point to the berth position in minimum time. The minimum-time control method is an effective, albeit highly nonlinear, maneuvering method, deriving the maximum maneuverability of a ship approaching a berth. Simulations included constant wind disturbances, and two model predictive control (MPC) schemes were utilized in order to reduce the online computing time.

Chapter 4

The milliAmpere ferry

In the following chapter, the milliAmpere ferry is presented in detail. The ferry serves as both the experimental and simulation platform of this thesis. Consequently, a summary of the mathematical models and the overall structure of the system is deemed relevant. Section 4.1 is based upon chapter 3 in Knudsen [2020].

4.1 The milliAmpere models

The mathematical ship model applied in the milliAmpere project is a surge-decoupled model, i.e. surge is not directly affected by neither sway nor yaw. The assumption needed for this to be valid is starboard-port symmetry [Fossen, 2021]. As seen in the sketch of the waterline footprint of the milliAmpere ferry in fig. 1.2, this assumption is valid. Decoupling surge from sway and yaw reduces the complexity of the model, and is a common assumption to make. The following sections 4.1.1–4.1.3 present various mathematical models in the milliAmpere simulator, albeit none have been implemented during this thesis.

4.1.1 The system matrices

The mass matrix of the surge-decoupled model, used in both the simulator and the onboard computer on the milliAmpere ferry, is given below:

$$\boldsymbol{M} = \begin{bmatrix} m_{11} & 0 & 0 \\ 0 & m_{22} & m_{23} \\ 0 & m_{32} & m_{33} \end{bmatrix} = \begin{bmatrix} 2390 & 0 & 0 \\ 0 & 2448 & 268.1 \\ 0 & -23.84 & 4862 \end{bmatrix} \tag{4.1}$$

Furthermore, the Coriolis and centripetal matrix $\boldsymbol{C}(\boldsymbol{\nu}_r)$ in the surge-decoupled model is defined as:

$$\boldsymbol{C}(\boldsymbol{\nu}_r) = \begin{bmatrix} 0 & 0 & c_{13}(\boldsymbol{\nu}_r) \\ 0 & 0 & c_{23}(\boldsymbol{\nu}_r) \\ c_{31}(\boldsymbol{\nu}_r) & c_{32}(\boldsymbol{\nu}_r) & 0 \end{bmatrix} \tag{4.2}$$

with the matrix elements listed below:

$$\begin{aligned} c_{13}(\boldsymbol{\nu}_r) &= -m_{22}v_r - \frac{1}{2}(m_{23} + m_{32})r_r \\ c_{23}(\boldsymbol{\nu}_r) &= m_{11}u_r \\ c_{31}(\boldsymbol{\nu}_r) &= m_{22}v_r + \frac{1}{2}(m_{23} + m_{32})r_r \\ c_{32}(\boldsymbol{\nu}_r) &= -m_{11}u_r \end{aligned} \tag{4.3}$$

Similarly, the damping matrix contains only nonlinear terms:

$$\boldsymbol{D}(\boldsymbol{\nu}_r) = \begin{bmatrix} d_{11}(\boldsymbol{\nu}_r) & 0 & 0 \\ 0 & d_{22}(\boldsymbol{\nu}_r) & d_{23}(\boldsymbol{\nu}_r) \\ 0 & d_{32}(\boldsymbol{\nu}_r) & d_{33}(\boldsymbol{\nu}_r) \end{bmatrix} \tag{4.4}$$

with the elements listed in eq. (4.5).

$$\begin{aligned} d_{11}(\boldsymbol{\nu}_r) &= 106.6 + 21.39|u_r| + 37.43u_r^2 \\ d_{22}(\boldsymbol{\nu}_r) &= 29.44 + 172.9|v_r| + 1517.0|r_r| + 1.338v_r^2 \\ d_{23}(\boldsymbol{\nu}_r) &= -62.58 - 488.7|v_r| + 198.2|r_r| - 77.58u_r \\ d_{32}(\boldsymbol{\nu}_r) &= -7.34 + 4.352|v_r| - 437.8|r_r| + 90.97u_r \\ d_{33}(\boldsymbol{\nu}_r) &= 142.7 + 122.0|v_r| + 831.7|r_r| - 178.5u_r \end{aligned} \tag{4.5}$$

In eqs. (4.3) and (4.5) u_r, v_r and r_r denotes the relative surge, sway and yaw velocity, respectively.

4.1.2 Various simulator models

Several mathematical models have been implemented in the milliAmpere simulator in previous projects, and some of these will be briefly presented as context for this thesis. These models have in common that they are used during simulations only, not during experimental testing. During the validation task addressed in chapter 5, the models used only in the simulator were investigated to narrow down the reason of the model discrepancies. That being said, the reason for these discrepancies may be caused by other factors or models.

Pedersen [2019] identified several mathematical models using a method similar to model predictive control (MPC). Two of these models were a fully-coupled and a surge-decoupled 3DOF maneuvering model. The parameter values of the latter differs from the surge-decoupled model presented in section 4.1.1. Apart from these two maneuvering models, several of the models identified by Pedersen [2019] are used in the simulator. These models will be presented next.

The motor-speed dynamic model for motor i from Pedersen [2019] is on the form:

$$\dot{\omega}_i = K_{\omega,i}(\omega_{d,i} - \omega_i), \qquad i \in \{1, 2\} \tag{4.6}$$

where ω_i denotes the rotational speed for motor i, and $\omega_{d,i}$ denotes the desired rotational speed. The gain $K_{\omega,i}$ represents miscellaneous physical aspects (inertia of the shaft, hydrodynamic added mass, etc.). Similarly, Pedersen [2019] identified the dynamics of the azimuth angles, which is on the form:

$$\dot{\alpha}_i = K_{\alpha,i} \frac{(\alpha_{d,i} - \alpha_i)}{\sqrt{(\alpha_{d,i} - \alpha_i)^2 + \epsilon_i^2}}, \qquad i \in \{1, 2\} \tag{4.7}$$

where α_i denotes the azimuth angle for azimuth i, $\alpha_{d,i}$ denotes desired angle for azimuth i, the parameter $K_{\alpha,i}$ represents rotational transmission velocity and ϵ_i is a tunable parameter for the transient behavior. Lastly, Pedersen [2019] presents a wind force model for marine crafts in motion:

$$\boldsymbol{\tau}_{\text{wind}} = \frac{1}{2}\rho_a V_{rw}^2 \begin{bmatrix} C_X(\gamma_{rw}) A_{F_w} \\ C_Y(\gamma_{rw}) A_{L_w} \\ C_N(\gamma_{rw}) A_{L_w} L_{oa} \end{bmatrix} \tag{4.8}$$

where γ_{rw} is the relative wind angle of attack, V_{rw} denotes the relative wind speed, A_{F_w} and A_{L_w} denote the frontal and lateral surface area of the vessel, and L_{oa} is the total length of the vessel. For an explanation of the rest of the parameters, consult Fossen [2011, pp.188–191]. The wind velocity model in the simulator consists of one steady part, modeled as a second-order Gauss-Markov process, and a gust part, modeled as a first-order Gauss-Markov process.

Table 4.1 shows the simulator values of the parameters in eqs. (4.6)–(4.8).

Parameter	Value
$K_{\omega,1}$	0.563
$K_{\omega,2}$	0.591
$K_{\alpha,1}$	34.46
$K_{\alpha,2}$	37.53
ϵ_1	6.277
ϵ_2	7.721
A_{F_w}	$2.9\,\mathrm{m}^2$
A_{L_w}	$8.6\,\mathrm{m}^2$
L_{oa}	$5.0\,\mathrm{m}$

Table 4.1: Parameter values for mathematical models used in the milliAmpere simulator, identified by Pedersen [2019].

During the work of Knudsen [2020], an ocean current model was implemented in the simulator. The derivative of the ocean current speed is modeled as a first-order Gauss-Markov process. The ocean current speed V_c consists of this dynamics and a constant term, which is decomposed in $\{b\}$ given the horizontal current direction β_{V_c} and ψ.

During previous works, contact forces between the vessel and the tip of "Hurtigbåtkaia" at Brattøra have been implemented in the simulator. The normal force and collision points follow a spring-damper model, possibly to simulate fender forces. The contact forces are implemented to make it possible for the milliAmpere ferry to experience both a static friction force (modeled as a Coulomb friction force), and slide along the quay wall during impact. The latter takes place if the friction force cancels out the sum of both the normal force and the various other forces acting on the ferry. The yaw-moment is not considered during the calculation of the contact forces, according to the documentation.

4.1.3 The numerical integrator

A numerical integrator yields a numerical solution to a differential equation on the form

$$\dot{\boldsymbol{y}} = \boldsymbol{f}(\boldsymbol{y}, t), \qquad \boldsymbol{y}(t_0) = \boldsymbol{y}_0 \tag{4.9}$$

Equation (4.9) is an initial value problem. The goal of the numerical integrator is to approximate the exact solution of the (nonlinear) derivative function $\boldsymbol{f}$, with an acceptable accuracy.

The milliAmpere simulator consists of a multitude of differential equations, linear and nonlinear alike. The numerical integrator used in the simulator is a Runge-Kutta 4th order (RK4) method, which uses $\sigma = 4$ stages in order approximate $\boldsymbol{f}$. Butcher arrays are used to distinguish different explicit Runge-Kutta methods, and RK4 has the following Butcher array [Egeland and Gravdahl, 2002]:

0				
$1/2$	$1/2$			
$1/2$	0	$1/2$		
1	0	0	1	
	$1/6$	$2/6$	$2/6$	$1/6$

Table 4.2: The Butcher array of the 4th order Runge-Kutta method.

The RK4 method was implemented in the simulator before the work of this thesis.

4.2 The system structure

This section describes a few of the subsystems in the milliAmpere code base. None of the subsystems mentioned next have been implemented during the work of this thesis, but the section is meant as a technical background for the validation and berthing tasks, in particular.

4.2.1 ROS and technical specifications

The milliAmpere software is written in Python 2.7.12 and 3.7.10, and utilizes Robot Operating System (ROS): a framework consisting of several libraries and tools used to create collaborative robot software.The release used for the milliAmpere software is ROS Kinetic Kame, first released in May, 2016.

The idea of implementing a robot system in ROS is to create modular nodes, each node designated with performing a distinct task. The various nodes communicate by sending messages over public topics, to which all nodes in the system can subscribe. All messages from one simulation or one experimental trial are stored in a `.bag` file, and a designated ROS library for reading these messages can be utilized in Python, C++ and MATLAB. The timestamps of the messages are given in Unix time, the number of seconds since January 1, 1970 excluding leap seconds.

In general, the ROS framework tries to uphold the simulation rate each node is initialized with. This may not always be possible, and could potentially result in a given ROS node being interrupted while performing a task. The ROS system is run in a Docker container, both on developer computers and the milliAmpere onboard computer. The versions used for development were Docker 20.10.6 and docker-compose version 1.17.1, on the Linux operating system Ubuntu 18.04.

4.2.2 The milliAmpere subsystems

The structure of the physical milliAmpere system includes a DP system, thrust allocation, guidance and navigation systems, a supervisor, among others. Each of these subsystems are implemented in distinct ROS nodes.

The milliAmpere simulator is a part of the same code base and utilizes a majority of the same subsystems as the aforementioned physical system, e.g. the DP and guidance systems. A navigation system used for simulations only has been developed previously, as well. An overview of the nodes and topics used in the simulator is shown in fig. D.1. A simple graphical user interface, enabling easy setup of waypoints for the DP system and showing a map with the pose of milliAmpere, has been implemented in previous work. This interface is shown in fig. 4.1.

Supervisor

The supervisor in the system implements a finite state machine, enabling different system modes and transitions between these. This is utilized during the berthing scheme presented in chapter 6. The supervisor relies heavily on the Python library `smach`[1].

There are eight different modes in the system, with the *DP* and *Berthing* modes being of interest for this thesis, as well as the *Joystick* mode for experimental testing. The latter

[1] `http://wiki.ros.org/smach`, accessed May 19, 2021.

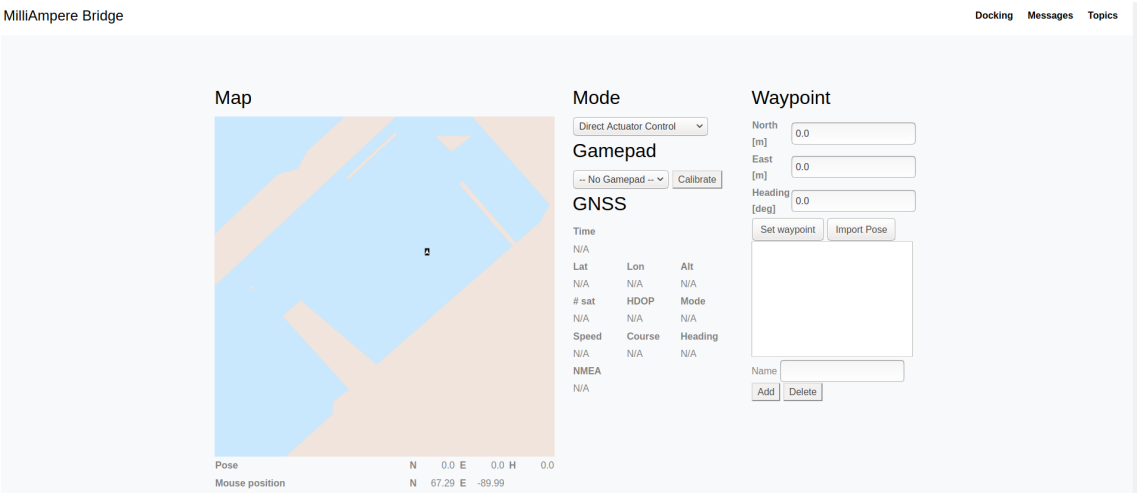

Figure 4.1: The graphical interface containing a map of Brattørkaia in Trondheim.

mode is used when manually controlling the ferry with a remote control, and is a mode never used during the development of the berthing scheme in the simulator. The default supervisor mode when the simulator is initialized is *Direct actuator control*.

Reference model

The third order position and attitude reference model follows the vectorial setting:

$$\boldsymbol{\eta}_d^{(3)} + (2\boldsymbol{\Delta} + \boldsymbol{I})\boldsymbol{\Omega}\ddot{\boldsymbol{\eta}}_d + (2\boldsymbol{\Delta} + \boldsymbol{I})\boldsymbol{\Omega}^2\dot{\boldsymbol{\eta}}_d + \boldsymbol{\Omega}^3\boldsymbol{\eta}_d = \boldsymbol{\Omega}^3\boldsymbol{r}^n \tag{4.10}$$

where $\boldsymbol{\eta}_d$ denotes the desired position and attitudes, and $\boldsymbol{r}^n$ denotes the reference signal in $\{n\}$ [Fossen, 2011, pp.249-250]. The goal of the reference model is to filter steps in $\boldsymbol{r}^n$. The design matrices $\boldsymbol{\Delta} > 0$ and $\boldsymbol{\Omega} > 0$ contain relative damping ratios and natural frequencies, respectively. The values of the elements in these matrices are tunable, albeit the default values used in this thesis are:

$$\boldsymbol{\Delta} = \text{diag}(3.0, 3.0, 3.0) \tag{4.11}$$
$$\boldsymbol{\Omega} = \text{diag}(0.5, 0.5, 0.5) \tag{4.12}$$

The position, velocity and acceleration references published by the guidance node, are all given in $\{n\}$. Furthermore, saturation on the velocity and acceleration references are:

$$\dot{\boldsymbol{\eta}}_{d,\text{sat}} = \begin{bmatrix} \pm 0.5\,\text{m}\,\text{s}^{-1} & \pm 0.5\,\text{m}\,\text{s}^{-1} & \pm 0.05\,\text{rad}\,\text{s}^{-1} \end{bmatrix}^\top$$
$$\ddot{\boldsymbol{\eta}}_{d,\text{sat}} = \begin{bmatrix} \pm 0.05\,\text{m}\,\text{s}^{-2} & \pm 0.05\,\text{m}\,\text{s}^{-2} & \pm 0.03\,\text{rad}\,\text{s}^{-2} \end{bmatrix}^\top$$

DP controller

The DP controller consists of one PID controller in each DOF, with anti-windup implemented due to the saturating elements in the guidance node. The DP controller gains

remain unchanged throughout the thesis, and are the following:

$$\begin{aligned}\boldsymbol{K}_p &= \mathrm{diag}(200, 200, 800)\\ \boldsymbol{K}_i &= \mathrm{diag}(10, 10, 15)\\ \boldsymbol{K}_d &= \mathrm{diag}(700, 700, 1600)\end{aligned}$$

Anti-windup is implemented in the DP controller, with the control input limits

$$\boldsymbol{\tau}_{\text{windup}} = \begin{bmatrix}150\,\mathrm{N} & 150\,\mathrm{N} & 200\,\mathrm{N}\end{bmatrix}^\top$$

in such a way that the contribution from the integral action never exceeds these limits. This is achieved by clipping the integrator value to these limits if the absolute value exceeds them. The reason behind the anti-windup scheme is to avoid a scenario following large setpoint changes. Such scenarios may result in a large overshoot and a long period of time before the integrator is brought back to the steady-state value. This is due to the integrator value becoming very large without effecting the plant output [Bohn and Atherton, 1995]. When calculating the desired control input, the DP controller considers the damping matrix in eq. (4.4) and the diagonal elements of the mass matrix in eq. (4.1).

Thrust allocation

The goal of the thrust allocation system is to calculate the individual thruster forces, which results in a given desired control force vector $\boldsymbol{\tau}$ [Martinsen et al., 2020]. The collective vector of control forces and moments is given below [Martinsen et al., 2020]:

$$\boldsymbol{\tau} = \begin{bmatrix} F_{x,1} + F_{x,2} \\ F_{y,1} + F_{y,2} \\ F_{y,1} l_{x,1} + F_{y,2} l_{x,2} \end{bmatrix} \tag{4.13}$$

where $l_{x,i} = 1.80\,\mathrm{m}, i = \{1, 2\}$ denotes the distance from the position of azimuth thruster i to the center of origin (CO). Furthermore, the force in $\{b\}$ from thruster i is denoted $F_{x,i}$ and $F_{y,i}$ in surge and sway, respectively.

The milliAmpere ferry is a fully actuated marine vessel, as the dimension of $\boldsymbol{\tau}$ ($r = 3$) equals the dimension of the generalized position vector $\boldsymbol{\eta}$ ($n = 3$). In the 3DOF case, full actuation results in independence between the heading of the vessel and the direction of its linear velocities [Breivik et al., 2006].

4.3 Previous docking projects on the milliAmpere ferry

The next two paragraphs present previous docking work, both using the milliAmpere ferry as the experimental test platform.

4.3.1 Trajectory Planning and Control for Automatic Docking of ASVs with Full-Scale Experiments

Bitar et al. [2020] combined a trajectory planner and a DP controller, with the former formulated as an optimal control problem. The goal of the trajectory planner was to arrive at the desired docking pose with zero velocity. The DP system was used was to account for both unmodeled dynamics, and environmental forces and moments. The trajectory planner included a map of the harbor in which the milliAmpere intended to dock, this map was used as constraints for the planner. Experimental tests were conducted with wind of $2 - 3\,\mathrm{m\,s^{-1}}$ and calm sea. Of continuation of the work, tuning of the DP controller, development of an environmental disturbance estimator as well as further research of the coupling effects in the feedforward term of the DP controller, are mentioned.

4.3.2 Optimization-Based Automatic Docking and Berthing of ASVs Using Exteroceptive Sensors

Martinsen et al. [2020] extended the work of Bitar et al. [2020], developing a valid scheme for both docking and undocking. Spatial constraints were constructed from the map of the harbor known in advance, in which landmasses are represented as polygons. Information from a light detection and ranging (LIDAR) device was used to supplement the harbor map, adding additional spatial constraints for the optimal control problem. The use of short range ultrasonic distance sensors may be used to complement the LIDAR and harbor map, in addition to using radar and cameras for better environmental view. The DP system was used for reference tracking, with no spatial constraints violated and obstacle avoidance being successful.

Chapter 5

Model validation and tuning

This chapter aims to summarize the work of model validation and tuning of parameters in the milliAmpere simulator. The validation was the first task of this thesis, the results and discussion will be presented in section 7.2.

5.1 Motivation

The results from the specialization project [Knudsen, 2020] indicated that the simulator did not behave as well as previous experimental results had shown. In addition, the results from Bitar et al. [2020], Martinsen et al. [2020] indicate that the DP system performs well enough, although further tuning is one improvement mentioned. Consequently, the DP system has remained unchanged during this task, as tuning of that particular subsystem should be disconnected from tuning of the mathematical models. This implies that even though e.g. the mass matrix element m_{33} has been tuned in the maneuvering model, the value has remained unchanged in the diagonal mass matrix used in the DP controller.

5.2 Metrics applied in this thesis

A total of 19 calculated values have been used as metrics when determining the most favorable model modifications: The mean absolute error (MAE) and the root-mean-square error (RMSE) in pose, velocity, and the gradients of the control input references, as well as the heading time constant from the start of each simulation. The reason for including control input references is to punish rapidly oscillating control input references. Chances are that the nature of such control inputs are too fast for the controller to follow.

MAE is calculated as:

$$\text{MAE} = \frac{\sum_{k=1}^{n} |x_k - x_{ref,k}|}{n}, \qquad k \in \{1, .., n\} \tag{5.1}$$

whereas the formula for RMSE given by:

$$\text{RMSE} = \sqrt{\frac{\sum_{k=1}^{n}(x_k - x_{ref,k})^2}{n}}, \qquad k \in \{1, .., n\} \tag{5.2}$$

In both eqs. (5.1) and (5.2), n denotes the number of data points, x_k is the state at time instance k and $x_{ref,k}$ denotes the state reference at time k.

Chai and Draxler [2014] discusses thoroughly both RMSE and MAE, regarding model evaluation and assessment of the performance of a model. They conclude that, when assessing the performance of a mathematical model, a combination of metrics will often be required, as different metrics have different advantages and disadvantages. RMSE is more sensitive to outliers, while MAE may not reflect model errors as well as RMSE. The latter is due to MAE's suitability for modeling uniformly distributed errors, while model errors often follow a normal distribution [Chai and Draxler, 2014]. In addition, any given metric emphasizes only one projection of the errors of a model. Consequently, both RMSE and MAE were chosen as metrics for the validation task.

A common method of estimating the heading dynamics is to look at the step response, and identifying the time constant of the heading dynamics, from here denoted T_ψ. The time constant is defined as the time it takes for the step response to reach 63.2% of its steady-state magnitude [Furat and Eker, 2014]. In order to estimate the heading time constant from the experimental data from Holtung-Eriksen, 30 seconds of the heading reference data and the resulting heading behavior was used. In this data, a step from $83.946°$ to a final value of $159.52°$ occurs, and was replicated in all of the 35 simulations.

5.3 Deciding the most favorable simulator model

For the validation task, the 19 metrics calculated from the experimental data were used as references for the 35 simulations. The goal was to find the model changes resulting in metrics closest to the experimental metrics. This will be presented more in depth next.

The formula for normalizing any given vector $\boldsymbol{\gamma} = \begin{bmatrix}\gamma_1, \ldots, \gamma_q\end{bmatrix}$ is:

$$\begin{aligned} \hat{\gamma}_i &= \frac{\gamma_i - \min \boldsymbol{\gamma}}{\max \boldsymbol{\gamma} - \min \boldsymbol{\gamma}}, \qquad i \in \{1, \ldots, q\} \\ \hat{\boldsymbol{\gamma}} &= \begin{bmatrix}\hat{\gamma}_1, \ldots, \hat{\gamma}_q\end{bmatrix}^\top \end{aligned} \tag{5.3}$$

where, from here on, the superscript $\hat{\cdot}$ denotes a normalized vector. For all metric values, the corresponding metric from the experimental data has been used as reference, meaning that the values to normalize using eq. (5.3) are

$$T^i_{\psi,\text{error}} = \left|T_{\psi,\text{experimental}} - T^i_\psi\right| \tag{5.4a}$$

$$m^i_{\text{error},j} = \left|m_{\text{experimental},j} - m^i_j\right| \tag{5.4b}$$

for a given simulation i. m_j^i denotes any RMSE or MAE metric.

Furthermore, p denotes the number of simulations. The total cost of simulation $i \in \{1, \ldots, p\}$, denoted κ_i, is given by the following formula:

$$\kappa_i = \hat{T}^i_{\psi,\text{error}} + \sum_{j=1}^{\mu} \hat{m}^i_{\text{error,j}} \tag{5.5}$$

Here, $T^i_{\psi,\text{error}}$ and $m^i_{\text{error,j}}$ are defined in eq. (5.4). It's important to point out that κ_i contains the normalized error values of these. Furthermore, μ denotes the total number of RMSE and MAE metrics in pose, velocity and gradients of control input references, two metrics for each DOF. In this case,

$$\mu = \underbrace{2}_{\substack{\text{no. of types} \\ \text{of metrics}}} \cdot \underbrace{3}_{\substack{\text{no. of} \\ \text{DOFs}}} \cdot \underbrace{3}_{\substack{\text{position, velocity,} \\ \text{control input} \\ \text{gradients}}} = 18$$

The total cost vector is defined as:

$$\boldsymbol{K} = \left[\kappa_1, \ldots, \kappa_p\right] \tag{5.6}$$

Lastly, σ_{opt} denotes the simulation which is closest to the experimental metrics overall:

$$\sigma_{\text{opt}} = \arg\min_i \boldsymbol{K} \tag{5.7}$$

with $\boldsymbol{K}$ defined in eq. (5.6). As such, σ_{opt} denotes the simulation with the most favorable model changes, numbered according to tables 5.1 and B.1. This method does not include weights for each metric, albeit being an alternative approach. The reasons for omitting the weights from this scoring model approach are shortly presented in section 1.4, with a more detailed discussion in Sargent [2010].

5.4 Validation of the milliAmpere simulator models

The following section presents information regarding the experimental data used for validation. Available weather data for December 1, 2020, an overview of the method used for validation, and a chosen subset of the 35 simulations with their respective parameter changes will be presented, as well.

5.4.1 The experimental data used for model validation

The data used as the foundation for the model validation was collected by Bjørn-Olav Holtung-Eriksen, a postdoctoral fellow at the Department of Engineering Cybernetics, NTNU, on December 1, 2020.

The data consists of one ROS bag with 4.3 GB of data, with relevant ROS messages collected by the onboard computer on the milliAmpere ferry throughout approximately

6.5 hours of experimental testing. Subsets of the reference data in pose, velocity and acceleration were used to mimic the guidance system during the 35 simulations. I.e., the ROS node usually handling the guidance system was disabled during the validation task. A chosen subset of reference data, conducted between 13:16:40 to 13:58:20 UTC+01:00 on December 1, 2020, formed the basis of the replicated operation in the simulator. Plots of the pose and velocities from the full experiment are given in appendix A, with the chosen time interval used for validation marked in the plots.

The data collected by Holtung-Eriksen originates from docking experiments. Consequently, the data was deemed relevant enough for model validation for this thesis. In particular, the velocities throughout the experiment are low and coincide with the velocities presented in Knudsen [2020]. With few exceptions, the surge velocity and sway velocity during the experiment is below $\pm 1.0\,\mathrm{m\,s^{-1}}$ and $\pm 0.50\,\mathrm{m\,s^{-1}}$, respectively. The yaw rate rarely exceeds $\pm 0.10\,\mathrm{rad\,s^{-1}}$. One downside of using this docking data is that the applicable domain of the model changes may possibly be narrowed down, as briefly discussed in section 1.4. Consequently, the method used for validation may not scale well to larger vessels, or other vessels in general.

5.4.2 The weather conditions during the experiment

As the author of this thesis didn't participate in the experimental testing, historical data from the weather website `yr.no` (a service from the Norwegian Meteorological Institute and NRK) was used to check the weather at Ravnkloløpet. The temperature between 13:00:00 and 14:00:00 UTC+01:00 was reported to be in the range $[-0.10\,^{\circ}\mathrm{C},\ 0.10\,^{\circ}\mathrm{C}]$, with no precipitation during this time of day[1].

The historical data from `yr.no` doesn't contain wind data. Thus, data from *Norsk Klimaservicesenter* was consulted. Three weather stations around Trondheim, "Sverresborg", "Lade" and "Trondheim – Høvringen", were audited[2]. Only the latter detected wind: At 13:00 the mean wind velocity was $1.8\,\mathrm{m\,s^{-1}}$ with direction 216.0°, and at 14:00 the mean wind velocity was $2.2\,\mathrm{m\,s^{-1}}$ with a direction of 211.0°.

This weather survey was conducted in order to disclose any significant weather that may affected the experimental results drastically. As such, the wind conditions are known to some extent, while both the ocean current and wave conditions are unknown. Albeit, with such low wind velocities and these wind directions, the probability for large waves are small. The only waves the milliAmpere ferry may have experienced, would be caused by nearby boats in motion (i.e., wake waves).

5.4.3 Replicating the experiment in the simulator

The experiment was replicated in the simulator by keeping the guidance system disabled during all the simulations. As a substitute for the missing guidance node, the experimental

[1] `https://www.yr.no/nb/historikk/graf/1-2819430/Norge/Tr%C3%B8ndelag/Trondheim/Ravnklol%C3%B8pet?q=2020-12-01`, accessed March 18, 2021.

[2] `https://seklima.met.no/observations/`, accessed March 18, 2021.

reference data in pose, velocity and acceleration were published to the DP system by a separate ROS node. The DP system, the navigation system and the node implementing the thrust allocation algorithm were not of interest for this thesis, partly due to satisfactory behavior in earlier theses and works. As the guidance system was disabled during the simulations, validation of this particular subsystem will be left for future work.

The ROS node responsible for calculating the pose and velocity of the milliAmpere ferry in the simulator runs at $50\,\mathrm{Hz}$, so does the navigation system when performing experimental tests with the ferry. The guidance node, on the other hand, has a rate of $10\,\mathrm{Hz}$ both in the simulator and experimentally. As such, only each fifth data point in pose and velocity was used when calculating the MAE and RMSE after the validation and tuning. For every simulation, the initial pose of the milliAmpere ferry was:

$$\boldsymbol{\eta}_0 = \begin{bmatrix} -517.40 & -311.39 & 83.95^\circ \end{bmatrix}^\top \tag{5.8}$$

Throughout the task of tuning and validating the simulator model, environmental forces were not used in the simulator. Furthermore, the pose, velocity and acceleration references are identical in all 35 simulations.

For tuning of the damping matrix, the linear damping elements will be most significant during low-speed applications. Furthermore, only quadratic damping terms cause oscillatory behavior at low speed [Fossen, 2021, p.150]. Consequently, linear and quadratic damping elements were considered for tuning of the heading dynamics, in addition to the yaw moment m_{33}. The remaining parameter values in the $\boldsymbol{M}$, $\boldsymbol{C}$ and $\boldsymbol{D}$ matrices were too many to include in the validation task, and is a clear weakness of the manual approach taken in this thesis. Had more parameters been included, the conclusion of the validation task might have been different.

5.4.4 Subset of the 35 simulations

Parameter changes of the chosen 12 simulations are shown in table 5.1. These simulations are highlighted because they in total contain changes in all the parameters focused upon in the thesis, albeit the complete table containing information about all 35 simulations is given in table B.1. The number of tunable parameters in the azimuth, propeller and ship dynamics models in the simulator exceeds 30. As such, the focus in this thesis was only some of these parameters, although hopefully providing pointers to which subsystems that need further improvements.

In table 5.1 (as well as in table B.1), ϵ_i marked *NA* indicates that the azimuth dynamics only were the error states:

$$\dot{\alpha}_i = \alpha_{d,i} - \alpha_i, \tag{5.9}$$

and not the model given by eq. (4.7). Furthermore, empty cells indicate that the parameter value in question is unchanged from the value used during the experiment and the original simulation. These values are given as a shared upper row in table 5.1.

Significant work went into trying to tune the parts of the simulator dynamics not used experimentally, both the propeller model in eq. (4.6) and the azimuth dynamics given by eq. (4.7). The reason only ϵ_i was tuned for the azimuth dynamics in eq. (4.7), and not $K_{\alpha,i}$, is that ϵ_i is the parameter influencing the transient behavior of the azimuth model. Similarly, as the references for the motor speeds during both the experiment conducted by Bjørn-Olav Holtung Eriksen and the original simulation showed some highly unusual values and rapid change thereof, the motor speed parameters $K_{\omega,1}$ and $K_{\omega,2}$ were two of the main focus parameters.

Parameter changes

Model	***M*** *matrix*	*Motor speed*		*Azimuth angles*		***D*** *matrix*			
No.	m_{33}	$K_{\omega,1}$	$K_{\omega,2}$	ϵ_1	ϵ_2	N_r	N_v	$N_{\|v\|v}$	$N_{\|v\|r}$
Exp.	4862	0.563	0.591	6.277	7.721	-142.7	7.34	-4.352	-122
Orig.									
1.	4660			*NA*	*NA*				
3.	4660	1.0	1.0						
6.			*0.300*						
7.		0.500	0.400						
12.		0.450	0.450						
17.	5200	0.450	0.450	8.000	9.000			-24.352	
21.	5000	1.0	1.0					-24.352	-250
23.		**1.0**	**1.0**			**-250.0**			
24.		1.0	1.0			-250.0	8.50	-24.352	
28.	4700	1.0	1.0			-250.0			
32.		1.0	1.0			-200.0	2.00		
33.		1.0	1.0			-200.0	15.0		

Table 5.1: Parameter changes in 12 of the 35 tuning simulations. The abbreviations *Exp.* and *Orig.* stand for the experimental data and the simulation using the original simulator model, respectively. Bold symbolizes the most favorable simulation, italics symbolizes the least favorable simulation.

Chapter 6

The berthing scheme

This chapter presents the berthing scheme, the third and final task of the thesis, and is a continuation of the work conducted during the specialization project [Knudsen, 2020]. Results from two experimental tests, conducted on April 19 and May 10, form the basis of important changes to the method and the discussion of this thesis, respectively. The setup and results from May 10, as well as the discussion, follow in section 7.3.

First, the motivation and a thorough presentation of the phases will be presented, before the implementation of the transitions between different phases are presented. Lastly, a short summary of techniques which may improve these transitions is given.

6.1 Motivation and summary of the scheme

The berthing scheme tries to replicate what experienced ferry captains do in practice: Steering the vessel along a slowly-varying path towards the berth, making sure the heading angle is as desired, before controlling the velocity slowly towards the quay [Werner, 2020]. Consequently, the scheme tries to comply with the ”golden rule of berthing” (see section 1.2). Even though the milliAmpere ferry docks head-on the quay, the scheme is meant to be flexible in its implementation. Docking lateral to the quay should be possible, by changing some parameter values vital for the berthing scheme.

Furthermore, it was desired to create a modular method, making migration and integration with already implemented software easier. Consequently, only minor changes are made to e.g. the DP system, while a distinct ROS node is responsible for determining when phase transitions should take place and communicate this to the rest of the system. This node will be addressed as the berthing supervisor, not to be confused with the system supervisor. Additionally, a method which scales well regardless of e.g. the size and speed of the vessel, is desirable. This motivation resulted in using different phases during the berthing scheme, and transitioning between these during the flow of the operation. The berthing scheme consists of the following three phases:

1. APPROACH phase, the standard DP system is used to close the distance from a given starting point, towards a waypoint in proximity of the final berth.

2. BERTHING phase, where the goal is to keep the velocities low, while the milliAmpere ferry closes the final distance to the quay.

3. QUAY phase, with the goal being the fourth phase of docking, to keep the ferry at the berth.

The berthing operation is overseen by a distinct node containing the berthing supervisor, as depicted in fig. 6.1.

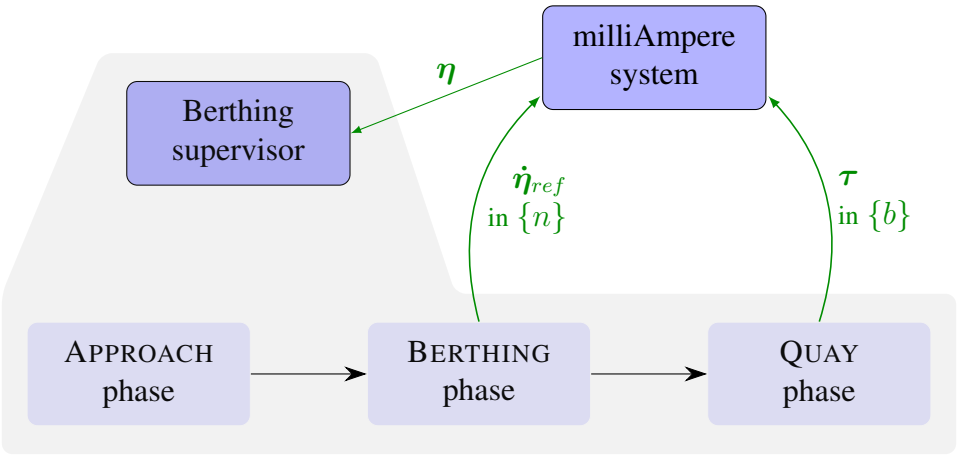

Figure 6.1: The gray polygon marks the berthing scheme, while *milliAmpere system* symbolizes the remaining system, including the DP and guidance systems. The berthing supervisor node oversees the transitions (black arrows) between the three berthing phases (light blue blocks). The green arrows represent important information flow. The berthing supervisor depends on position data from the navigation system, while velocity and control input references are sent to the milliAmpere system during the BERTHING and QUAY phase, respectively.

6.2 The proposed berthing scheme

As neither collision avoidance nor techniques to detect when the ferry makes contact with the quay will be considered, the berthing scheme will handle the second and fourth phases of docking presented in section 1.5.

6.2.1 The APPROACH phase

For the APPROACH phase the standard milliAmpere DP system, summarized in section 4.2.2, is used. After the initialization of the milliAmpere system and its nodes, the supervisor mode of the system switches to *DP* mode, before the waypoint:

$$\boldsymbol{\eta}_{\text{WP,approach}} = \begin{bmatrix} x^n_{\text{WP}_1} & y^n_{\text{WP}_1} & \psi_{\text{WP}_1} \end{bmatrix}^\top \tag{6.1}$$

is assigned to the guidance system. The rest of the phase is a standard low-speed DP operation.

6.2.2 The BERTHING phase

After transition from the APPROACH to the BERTHING phase, the supervisor mode is changed from *DP* to *Berthing* and the waypoint:

$$\boldsymbol{\eta}_{\text{WP,berthing}} = \begin{bmatrix} x^n_{\text{WP}_2} & y^n_{\text{WP}_2} & \psi_{\text{WP}_2} \end{bmatrix}^\top \tag{6.2}$$

is published to the guidance system. The DP controller gains are altered to

$$\begin{aligned} \boldsymbol{K}_p &= \text{diag}(0, 200, 800) \\ \boldsymbol{K}_i &= \text{diag}(0, 10, 15) \\ \boldsymbol{K}_d &= \text{diag}(0, 700, 1600) \end{aligned}$$

i.e. setting the controller gains in surge to zero. This alteration of the controller gains were made in order to avoid controlling the milliAmpere ferry in surge, while keeping control in sway and heading.

The guidance system is altered, as well. Using the waypoint given in eq. (6.2), the DP controller utilizes the position references, but neither the velocity nor acceleration references, from the reference model in order to calculate the control input references. Instead of using the velocity references, the desired velocity in $\{b\}$

$$\boldsymbol{\nu}_{d,\text{berthing}} = \begin{bmatrix} u_{d,\text{berthing}} & v_{d,\text{berthing}} & r_{d,\text{berthing}} \end{bmatrix}^\top \tag{6.3}$$

was rotated to $\{n\}$ using the constant angle of the quay structure α_{quay}, and published to the DP controller. In other words, the berthing scheme assumes that the ferry arrives at the quay with $\psi = \alpha_{\text{quay}}$. Additionally, the velocities of the ferry is not accounted for when the velocity reference in eq. (6.3) is set during the BERTHING phase. The acceleration references were set to zero. When the system meets the requirements for transitioning to the QUAY phase, a Boolean flag is published by the node overseeing the berthing operation. This flag is then published to the DP and guidance systems using a designated topic, and is published to the topic only once.

6.2.3 The QUAY phase

The goal of the QUAY phase is the fourth phase of docking; to push the ferry against the quay, for mooring and shut-down of the system to take place.

When the DP and guidance systems receive the Boolean flag published at the end of the BERTHING phase, both these systems become inactive. Instead, a constant vector of control input reference is commanded from the berthing supervisor node. This constant vector is

$$\boldsymbol{\tau}_{\text{quay}} = \begin{bmatrix} X_{ref,\text{quay}} & Y_{ref,\text{quay}} & N_{ref,\text{quay}} \end{bmatrix}^\top \tag{6.4}$$

and is given in $\{b\}$. The magnitude of the control input reference in surge was determined during simulations.

6.3 Transition between the phases

As the method is based upon three different phases, a way of transitioning from one phase to the next is crucial. In this thesis, an ellipse with center in a given waypoint is used. Two phase transitions are necessary during this berthing scheme, consequently two ellipses were defined. When transitioning should take place, is managed by the berthing supervisor node, see fig. 6.1.

Another requirement that must be met in order to transition from one phase to the next, is that the heading angle ψ is within the range $[-2.0\,\text{deg}, 2.0\,\text{deg}]$ from the angle of the quay structure α_{quay} in $\{n\}$. No requirements on the vessel velocities before transition were considered, although this could be included in future work.

The ellipses used for transitioning are rotated with an angle φ. Given the $\{n\}$ position $\begin{bmatrix} x^n & y^n \end{bmatrix}^\top$ of the ferry, in order to find out whether the CO of the ferry is within the ellipse the following checksum is utilized:

$$\frac{((y_c - y^n)\cos\varphi - (x_c - x^n)\sin\varphi)^2}{a^2} + \frac{((y_c - y^n)\sin\varphi + (x_c - x^n)\cos\varphi)^2}{b^2} \leq 1 \quad (6.5)$$

Above, the point $\boldsymbol{\xi}_c = \begin{bmatrix} x_c & y_c \end{bmatrix}^\top$ denotes the center of the ellipse, and corresponds to the waypoint assigned to the guidance system in each of the APPROACH and BERTHING phases. Furthermore, a denotes the semi-major axis of the ellipse, and b denotes the semi-minor axis. The ellipse is rotated with the $\{n\}$ angle φ:

$$\varphi = 180^\circ - \alpha_{\text{quay}} \quad (6.6)$$

Above, α_{quay} denotes the angle of the quay in $\{n\}$. The reason φ is defined as presented in eq. (6.6), is due to how a and b are being used in eq. (6.5).
The semi major and minor axes used during the APPROACH phase were much smaller because the unaltered DP system was used in this particular phase, and thought to yield a behavior which could meet these stricter transition requirements. Furthermore, the GNSS may not guarantee a resolution high enough for even smaller values for the semi major and minor axes. Consequently, the magnitude of the values in table 7.5 was deemed sufficient.

One alternative way to perform the phase transitions would be to use circles centered at the waypoints. The main reason ellipses were chosen, is that leeway along the transverse axis of the vessel is desired when using this scheme. Given that the intended berth is located at the center of the quay and the quay structure itself is much wider than the width of the vessel (as is the case with Hurtigbåtkaia and the milliAmpere ferry), it's deemed tolerable that the ferry doesn't reach the exact desired berth. The main concern is to hit the quay head on, i.e. with $\psi = \alpha_{\text{quay}}$. This stems from simulations resulting in varying performance of the altered control system, or in the QUAY phase, when no control is maintained as of now. This consideration may be up for evaluation in future work.

6.3.1 Bumpless transfer and gain scheduling

Techniques for improving the phase transitions will be briefly presented next, as context for future work. This is due to the results in section 7.3 indicating that this vital part of the berthing scheme is in need of refinement, before a proof of concept is ready. In addition, the basic approach behind the berthing scheme relies on a supervising system, determining when phase transitions should take place depending on different scenarios. Thus, the scheme may be subject to the bumpless transfer problem. Specific cases where such problems may arise will be discussed in section 7.3.3.

The bumpless transfer problem is characterized by large transients, taking place either during system initialization or when switching between different controllers in multi-controller schemes [Zaccarian and Teel, 2002]. These transients often arise due to the initial conditions of the controller and the plant, at the time of switching, being incompatible from the perspective of the control system. The underlying problem often originate from linear controllers being designed for nonlinear plants assumed to be approximately linear [Edwards and Postlethwaite, 1998]. This is a normal assumption to make. Linear controllers applied to nonlinear plants usually only provides decent closed-loop behavior close to the operating point of the controller. Consequently, several controllers may be designed to broaden the number of operation points. Zaccarian and Teel [2002] proposes a bumpless transfer scheme for linear systems, which assigns an appointed transient behavior immediately after switching between two controllers. This is done by applying additional control inputs to the feedback system. Asymptotic stability for the overall system is guaranteed, and works in the presence of saturation to the plant input. Moreover, consult e.g. Edwards and Postlethwaite [1998] for a literature review regarding bumpless transfer and anti-windup schemes.

Gain-scheduling is another technique for switching between controllers in multi-controller schemes. Gain-scheduled controllers for nonlinear plants are developed by first linearizing the plant about a number of operating points, then designing linear controllers for the plant linearization around each operating point [Kaminer et al., 1995]. Lastly, the parameters of the controllers from the previous step are interpolated to achieve adequate performance of the closed-loop system, before this gain-scheduled controller is implemented on the nonlinear plant. Kaminer et al. [1995] presents a simple method for implementation of gain-scheduled controllers, aiming to achieve the same internal and input-output properties of the overall linearized feedback system (nonlinear plant and gain-scheduled controller), as the feedback of the linearized plant around each operating point and the corresponding linear controller.

Chapter 7

Results and discussion

This chapter presents results from the three main tasks of the thesis, and a discussion related to each task. Additionally, the setup of the wave model tests and the berthing experiment conducted on May 10 will be given.

7.1 The wave model

This section outlines the DP simulation tests, in which the milliAmpere ferry is influenced by the wave model from section 2.3. The closed-loop behavior of the DP system onboard the milliAmpere ferry is deemed to be satisfying for the thesis. Consequently, tuning and/or other refinements of the DP system, to better counteract the wave forces and moments, will be left for future work.

7.1.1 Tests of the wave models

The wave models were tested in three similar scenarios, with the total wave forces and moments consisting of both first- and second-order wave models in all three DOFs. These models have been presented in eq. (2.10) and eq. (2.11), respectively. The goal of all three simulations was a DP stationkeeping test at the waypoint

$$\boldsymbol{\eta}_{\text{WP,wave}} = \begin{bmatrix} 0 & 0 & 0 \end{bmatrix}^\top \tag{7.1}$$

For each of the three simulations, the desired wave encounter angle was

$$\beta \in \{0\,\text{deg}, 90\,\text{deg}, -135\,\text{deg}\},$$

respectively. The reason for these choices were to test the effect of the waves acting in surge and sway only, as well as investigating the coupled motion in surge and sway when $\beta = -135\,\text{deg}$. The tests were initiated with 30 seconds without wave forces, followed by 90 seconds with wave forces activated. Neither ocean current or wind forces and moments acted upon the vessel during the simulations. The DP system was initialized from the start of the simulation, with a supervisor mode transition from *Direct actuator control* to *DP*.

Due to the nature of the wake forces, these only last for about 10 seconds before being zero. Afterwards, only the drift forces act on the ferry. The parameters of the two wake force models are given in table 7.1. The parameters were found through both open- and closed-loop simulations, testing how the wake forces influenced the milliAmpere ferry. The stationary components of the drift forces were set to $10\,\mathrm{N}$, and the standard deviations for the three zero-mean white noise processes were all 1.0.

Surge and sway		Heading	
A	30.0	A	10.0
a	0.45	a	0.75
B	30.0	B	10.0
b	0.45	b	3.50
f	5.0	f	5.0
φ	180.0	φ	180.0

Table 7.1: The parameter values of the wake force models.
The phase angle φ is given in degrees.

Plots of the wave forces and moments are given in figs. C.1–C.3.

7.1.2 Results

The pose of the milliAmpere ferry in each scenario is given in figs. 7.1–7.3, where β was $0°$, $90°$ and $-135°$, respectively. In all three cases, the x^n position changed from zero 2–3 seconds into the simulation. Independent of β, the norm of the combined excitation in x^n and y^n increased to about $0.25\,\mathrm{m}$. The heading response in all three cases was close to identical, as the parameters of neither the wake moment nor the second-order drift moment affecting heading were altered. The wake wave moment acting in heading excited ψ to little more than one degree. In all three cases, the x^n position of the ferry was most prone to long-lasting oscillations.

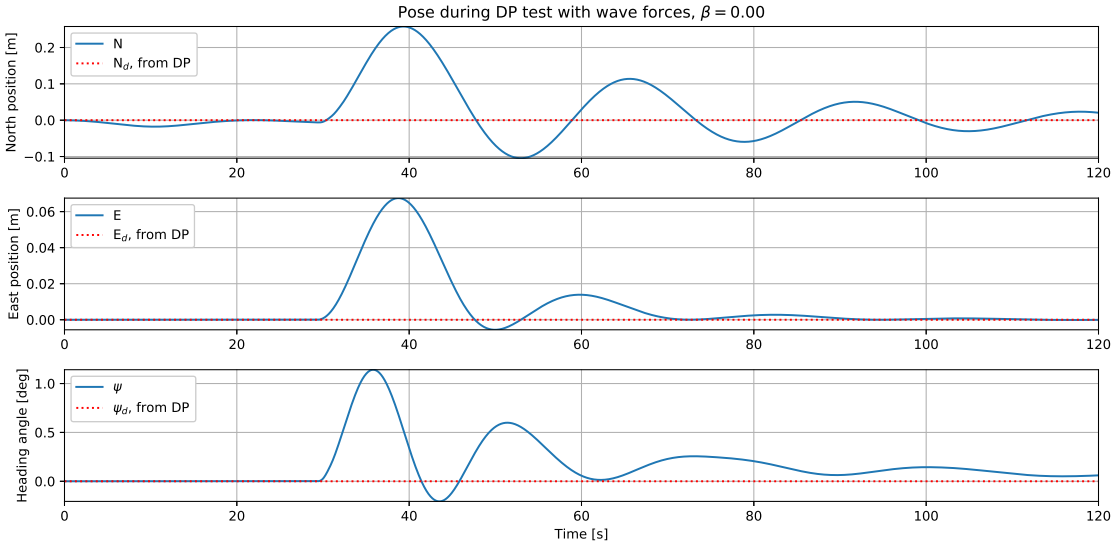

Figure 7.1: The pose of the ferry during the DP stationkeeping test, with $\beta = 0°$. The wake wave and wave drift forces are active from 30 seconds into the simulation.

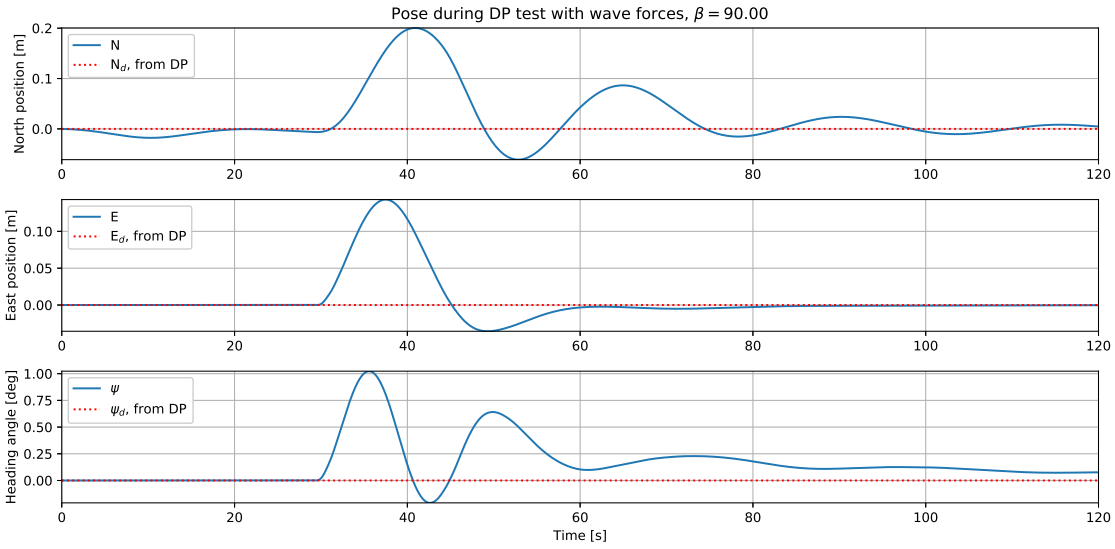

Figure 7.2: The pose of the ferry during the DP stationkeeping test, with $\beta = 90°$. The wake wave and wave drift forces are active from 30 seconds into the simulation.

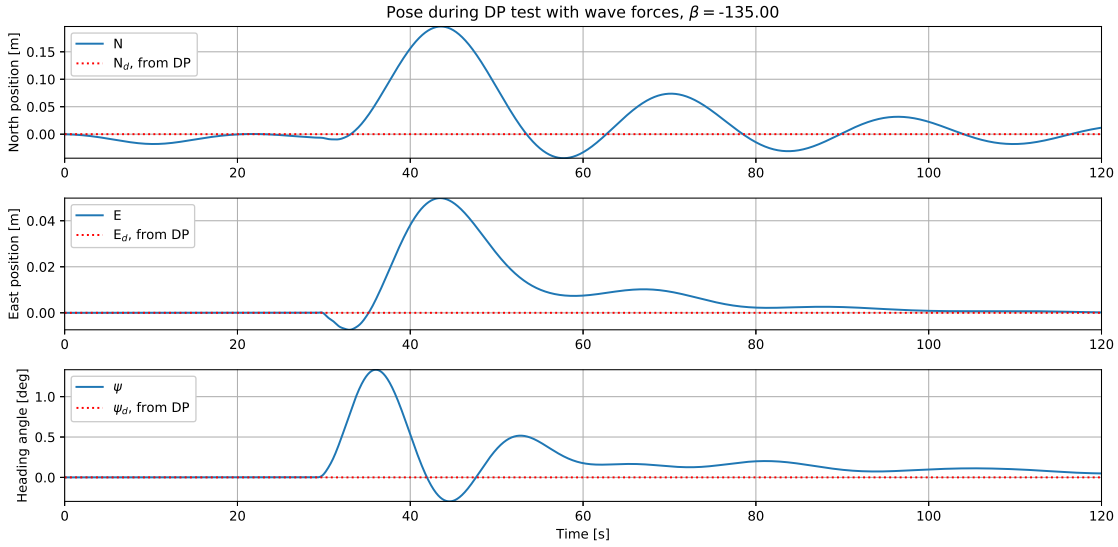

Figure 7.3: The pose of the ferry during the DP stationkeeping test, with $\beta = -135°$. The wake wave and wave drift forces are active from 30 seconds into the simulation.

7.1.3 Discussion

The reason for the deviations in x^n at the start of the simulations may be due to the initialization process of the DP controller. The wave models were inactive during this period of the simulations, consequently the deviations cannot originate from these. Another option is numerical uncertainty originating from either the RK4 method, the thrust allocation node or the actuator models. The ferry is not initialized with a surge velocity, albeit model discrepancies may be a third explanation. Despite these initial deviations, the DP controller manages to control x^n much closer to the zero reference before the wave models are activated. A possible way to rule out the cause of the deviations, would be to replicate the simulation tests using different position or heading parameters during initialization.

One possible explanation of the more significant oscillations in x^n may be that the DP controller focuses on counteracting the deviations in ψ and/or y^n, as the oscillations and deviations are reduced much quicker in these DOFs. The damping term acting in ψ in the DP controller is more than twice the value of the gains acting in x^n and y^n. Furthermore, a heavily damped response in heading may cause a more damped response in sway and consequently, as $\psi \approx 0$, in y^n shown in figs. 7.1–7.3.

The behavior of the DP controller is least satisfactory in x^n and y^n, as the excitations and oscillations are the largest. The long-lasting deviation in y^n seen in fig. 7.3 is likely due to the corresponding deviation in heading, as $\psi \approx 0$ for all three simulations and sway thus coincides with y^n. The most probable origin of the deviation in heading is the second-order drift moment, as this is the only moment acting in heading after roughly 40 seconds into the simulation. Better tuning of the integral action in the DP controller should remove

this deviation. The response in the position may be said to be in an appropriate magnitude, considering the intuitive behavior of smaller crafts in ports being hit by wake forces. The velocities of nearby marine crafts in the waters around Brattøra are usually small, due to both narrow and confined waters, lots of marine traffic and speed limits. The wake wave moment acting in heading could have been larger, in order to investigate how a larger heading excitation influences the overall behavior of the DP controller.

Nevertheless, the mathematical models of the wake forces and moments are simple, yet effective for the purpose of simulating the milliAmpere ferry. The models presented in this thesis may be used as is, or as inspiration for other ways of directly modeling wave forces and moments. Overall, the performance of the DP controller is satisfying when the desired wave encounter angle is 0° and 90°, more problems arise when the coupled effect in surge and sway is tested. That being said, tuning of the DP controller gains should be considered for future work, albeit the deviations across all DOFs are very small. It may take some time for the DP controller to dampen the excitations seen during the stationkeeping tests. Another aspect to consider in future work is a transit test between two waypoints, for examination of how the wave models influence the milliAmpere ferry during forward speed maneuvers. The waypoints could have a distance of 50-200 meters, or similar.

7.2 The validation task

Next, the results from the validation task of the milliAmpere ferry will be presented and discussed. The results consist of the calculated metric values for 12 of the simulations, as well as pose and velocity plots comparing the original simulator model and the most favorable model, alongside the experimental data. Information about what parameter changes were applied to each of the 35 simulations, as well as all RMSE and MAE values, are shown in appendix B.

Due to the arguments presented in Sargent [2010] regarding the chosen approach for model validation in this thesis, i.e. the scoring model, all RMSE and MAE values for 12 of the simulations will be presented. RMSE and MAE values for the experimental data and the original simulator model will be presented as well, for context and easy comparison. Another reason all metrics are presented, is that *one* combined score for each model modification yields little useful information and insight.

7.2.1 Results

Figures 7.4–7.6 compare the heading step responses, pose and velocities from the experiment, the original simulator model and the most favorable model changes. Regarding fig. 7.5, 40 seconds from the simulated responses and 111 seconds from the experimental pose were not included. The reason being that the 40 seconds containing the most interesting dynamics, i.e. the heading step responses, are shown in detail in fig. 7.4. Tables 7.2–7.4 show the RMSE and MAE metrics for the 12 chosen simulations. In the aforementioned tables, the most favorable model change $\sigma_{\text{opt}} = 23$ is given in **bold** font and the least favorable model change (simulation $i = 6$) is given in *italicized* font. In the former, the parameters $K_{\omega,1} = K_{\omega,2} = 1.0$ and the linear damping term in d_{33} $N_r = -250$.

As seen in fig. 7.4, σ_{opt} had a larger heading time constant, compared to the original model. Moreover, the yaw rate r of σ_{opt} depicted in fig. 7.6 was much more similar to the experimental yaw rate. Furthermore, the surge speed u produced by σ_{opt} was very similar to experimental results, albeit the sway speed v had a much more damped dynamics. The latter can be seen when comparing v of σ_{opt} to both experimental results and the original simulator model. A stationary deviation of $3 - 4^\circ$ in the heading angle of σ_{opt} took place from 25 seconds into fig. 7.4. When investigating the continuation of the heading dynamics at the start of fig. 7.5, it took roughly 120 seconds in total before the heading deviation of σ_{opt} was subdued.

		Pose					
		RMSE values			MAE values		
No.	$\hat{T}_\psi$ [s]	$\hat{x}^n$ [m]	$\hat{y}^n$ [m]	$\hat{\psi}$ [rad]	$\hat{x}^n$ [m]	$\hat{y}^n$ [m]	$\hat{\psi}$ [rad]
Experiment	6.30	2.212	1.152	0.070	1.607	0.983	0.033
Original	4.04	1.592	0.568	0.356	1.087	0.382	0.048
1.	3.70	1.804	0.756	0.914	1.226	0.466	0.230
3.	3.96	1.377	0.492	0.335	0.939	0.333	0.050
6.	*3.76*	*2.368*	*0.950*	*1.378*	*1.759*	*0.716*	*0.465*
7.	4.04	1.702	0.602	0.375	1.163	0.403	0.054
12.	4.12	1.852	0.699	0.566	1.257	0.446	0.097
17.	4.78	2.094	0.765	1.015	1.463	0.529	0.264
21.	4.90	1.389	0.500	0.219	0.949	0.341	0.031
23.	**5.24**	**1.459**	**0.523**	**0.088**	**1.004**	**0.360**	**0.023**
24.	4.94	1.455	0.526	0.091	1.000	0.357	0.028
28.	5.06	1.441	0.519	0.089	0.994	0.357	0.024
32.	4.30	1.381	0.497	0.299	0.951	0.341	0.038
33.	4.54	1.407	0.506	0.316	0.943	0.337	0.045

Table 7.2: Heading time constant T_ψ alongside RMS and MAE values for the pose from 12 of the 35 simulations. The values have been rounded off to three decimal places. Bold font symbolizes the most favorable model, while italicized text symbolizes the least favorable model.

	Velocities					
	RMSE values			MAE values		
No.	$\hat{u}$ [m/s]	$\hat{v}$ [m/s]	$\hat{r}$ [rad/s]	$\hat{u}$ [m/s]	$\hat{v}$ [m/s]	$\hat{r}$ [rad/s]
Experiment	0.171	0.062	0.017	0.097	0.040	0.009
Original	0.250	0.088	0.021	0.151	0.052	0.006
1.	0.305	0.132	0.054	0.206	0.083	0.030
3.	0.241	0.081	0.022	0.148	0.048	0.008
6.	*0.422*	*0.182*	*0.073*	*0.340*	*0.146*	*0.043*
7.	0.273	0.099	0.022	0.173	0.063	0.008
12.	0.301	0.112	0.027	0.197	0.072	0.011
17.	0.361	0.133	0.058	0.270	0.099	0.026
21.	0.212	0.075	0.017	0.118	0.041	0.005
23.	**0.201**	**0.071**	**0.016**	**0.109**	**0.038**	**0.004**
24.	0.210	0.074	0.017	0.117	0.040	0.005
28.	0.201	0.071	0.016	0.109	0.038	0.004
32.	0.203	0.070	0.018	0.113	0.038	0.005
33.	0.257	0.089	0.020	0.161	0.054	0.007

Table 7.3: RMS and MAE values for the velocities from 12 of the 35 simulations. The values have been rounded off to three decimal places. Bold font symbolizes the most favorable model, while italicized text symbolizes the least favorable model.

	Control input gradients					
	RMSE [N/s]			MAE [N/s]		
No.	$\hat{X}'_{ref}$	$\hat{Y}'_{ref}$	$\hat{N}'_{ref}$	$\hat{X}'_{ref}$	$\hat{Y}'_{ref}$	$\hat{N}'_{ref}$
Experiment	170.028	61.003	187.217	66.940	46.033	91.311
Original	270.046	40.645	63.136	159.414	15.239	18.473
1.	344.178	129.742	181.012	219.648	53.344	88.403
3.	252.666	42.850	63.799	156.513	17.409	20.919
6.	*468.009*	*227.987*	*304.189*	*354.000*	*108.063*	*147.767*
7.	270.227	39.217	57.910	145.191	14.386	17.721
12.	345.516	83.291	95.194	213.128	32.879	36.318
17.	339.714	147.729	206.347	209.389	49.098	66.158
21.	215.632	38.123	49.976	125.473	10.623	11.219
23.	**191.322**	**36.802**	**46.890**	**111.261**	**9.120**	**9.206**
24.	211.709	43.255	52.204	122.211	12.961	13.437
28.	192.012	35.959	49.249	111.119	9.156	9.304
32.	203.975	37.154	54.965	117.556	10.595	11.413
33.	262.241	42.217	58.221	161.296	16.865	18.342

Table 7.4: RMS and MAE values for gradients of control inputs for 12 of the 35 simulations. The gradients have been calculated using finite differences, with the values rounded off to three decimal places. The simulation rate of the control input references was 0.10 s. Bold font symbolizes the most favorable model, while italicized text symbolizes the least favorable model.

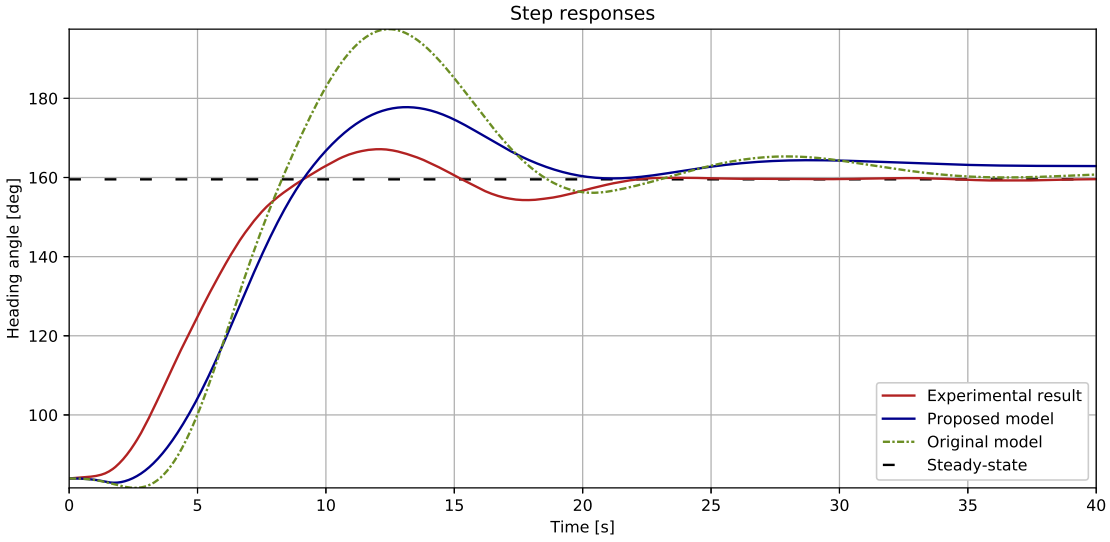

Figure 7.4: Comparison of step responses in heading. The heading angle of the original simulator model (green) has been unwrapped from $-\pi$ to π for readability. The proposed model (blue) has the most favorable performance of the 35 simulations. The black, dashed line shows the steady-state reference.

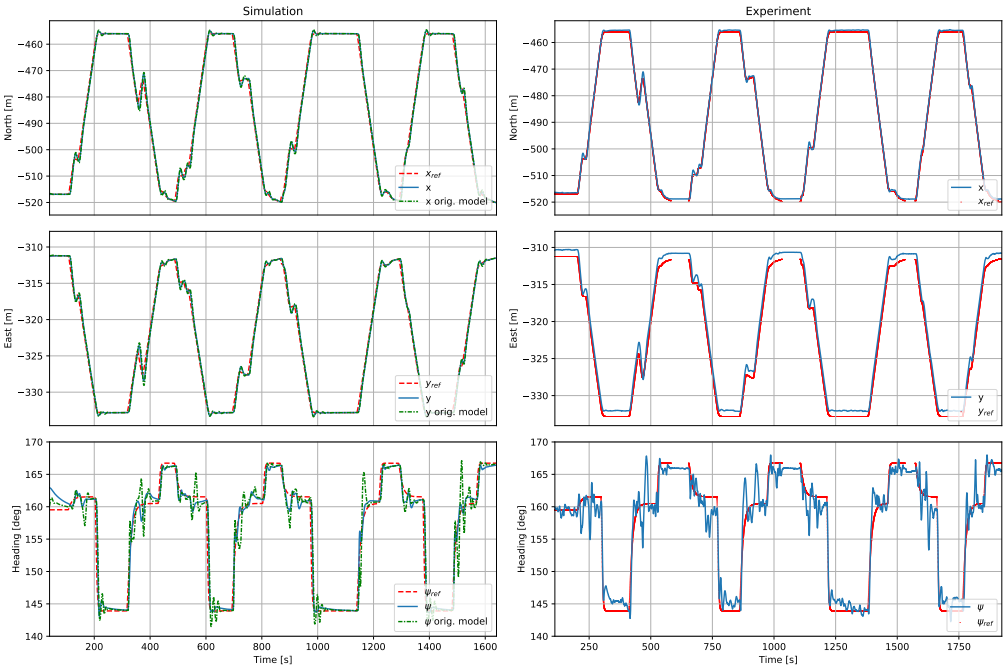

Figure 7.5: Comparison of the pose of the original (green) and proposed simulator model (blue) on the left, with the experimental pose (blue) given on the right. References are given in red. The first 40 seconds of the simulation data and first 111 seconds of the experimental data have been left out for readability.

Figure 7.6: Comparison of the velocities of the original and most favorable simulator models on the left, with the experimental velocities on the right. References are given in red.

7.2.2 Discussion

The discussion for the validation task will be divided in two parts. First, a discussion regarding the validation method used in the thesis takes place, then a discussion on the proposed model changes follows.

The experimental data and the method used for validation

The experimental data contained a variety of poses and velocities, nevertheless it's a specific data set. The data sets used by Pedersen [2019] are alternatives to the data set used in this thesis. These were collected specifically for model identification purposes. Although the experimental data mainly contained docking data and thus were relevant for this thesis, it may prove to be inadequate for other ship missions.

Furthermore, the parameter values in the $\boldsymbol{M}$, $\boldsymbol{C}$ and $\boldsymbol{D}$ matrices were too many to include in the validation task, and is a clear weakness of the manual approach taken in this thesis. When considering the azimuth, propeller and ship model parameters in the simulator, more than 30 parameters could be tuned. These parameters were often highly coupled. The trial-and-error method used in this thesis is inadequate in that regard, despite the goal of the task being a result which is "good enough" for berthing purposes. Which parameters were tested thoroughly may have been subjectively influenced, as some parameters were only tested once or twice before shifting focus to other parameters. This is another weakness regarding the method used for validation. Nevertheless, the subset of parameters that have undergone validation and tuning were based upon knowledge of the milliAmpere model structure (and not pure guess). The number of parameters made the work more challenging than first anticipated, and lead to less time available for improving the berthing scheme. If the simulator models undergo improvements and tuning in the future, a superior alternative to the approach taken in this thesis is e.g. the use of MPC, similar to the work of Pedersen [2019]. Machine learning would be another viable option. Chances are such approaches would take too much time for being only one task, out of several, in a master's thesis.

Other improvements to the method during the validation task would be to calculate RMSE and MAE values after each experiment, instead of only judging the behavior of model changes visually. These metric values may yield a better quantitative foundation from which to draw conclusions on the behavior. Deciding the metrics and how to best apply these *before* initiating the validation task, as well as investigating which aspects associated with each simulation (position deviations, azimuth angles, motor speeds, control input references, among others) are most relevant, exemplify other improvements the author in hindsight would have considered at the start of the validation task. Additionally, more time should have been dedicated to synchronize experimental and simulation data. This would result in the ability to compare deviations between actual experimental and simulated states, and not just their metrics.

Both the desired motor speeds and the desired azimuth angles are computed by the thrust allocation algorithm, mapping the control input references calculated by the DP system

to references for the aforementioned actuators. Consequently, quantifying control input references in order to reflect aggressivity may be achieved several ways. One could either look at the control input references themselves, or look at the resulting behavior in the azimuth angles or motor speeds. Another way to quantify aggressive control input references could be to measure how long control inputs, motor speed RPM and/or azimuth angles produced by one model are saturated, compared to experimental data or the original simulator model. Examining the error state between the control input references and the control forces and moments, given that the model for calculating the latter matches the reality exact, is another alternative for quantifying aggressive control input references. Looking at the gradients of the control input references, motor speed RPM or azimuth angles (the former being the choice in this thesis) are other possible approaches. The main goal regarding the use of control input gradients was to try avoiding rapid-changing or oscillatory control input references. The reasons being that the controller most probably won't be able to follow rapid changes in the references, and the resulting actuator behavior may lead to an increased fuel-consumption and wear-and-tear.

Regarding the reference data in pose, velocity and acceleration from the experimental data, two main challenge presented themselves during this task: (1) Synchronizing data, as the ROS nodes in general start and stop at different time stamps and run with different frequencies; and (2) the fact that during the experiment, the guidance system has been disabled for some periods of time while the DP and navigation systems have been active. An alternative way of calculating the RMSE and MAE values in this thesis, could be to use the average of the five consecutive data points in pose and velocities after a new reference has been sent from the guidance system. In this thesis, four out of five data points were instead overlooked, due to the challenge regarding data synchronization. This alternative approach assumes that reference data received by the guidance system is used by the DP controller until new reference data is available, which is a reasonable assumption to make.

The proposed model

$\sigma_{\text{opt}} = 23$ contains the most favorable model changes out of the 35 changes tried in this thesis, albeit most probably not the most optimal parameter changes overall. Other model changes that performed well in general were simulations $i = 28$ and $i = 24$, while $i = 6$ was the least favorable model changes overall. The parameter changes are shown in table 5.1.

The surge speed of σ_{opt}, shown in fig. 7.6, is more similar to experimental surge speed, compared to the original simulator model. The cause of this is most likely the alterations of the motor speed gains, resulting in a quicker response in surge overall. On the other hand, the sway velocity of σ_{opt} is too much damped compared to both the original simulator model and the experimental data. This is most likely a consequence of the much more damped yaw rate, i.e. the substantial increase of N_r. The damped sway velocity is suboptimal behavior, when the goal is to try replicating the experimental data.

The stationary deviation seen in fig. 7.4 is most likely not caused by the drastic increase of the linear term N_r in d_{33}. The yaw rate in fig. 7.6 from 20 seconds into the plot is

very small. As the aforementioned damping term acts on the yaw rate, this contribution is minimal and is most likely not the source of the deviation. The deviation would most probably not be caused by the changes of the motor speed gains, either, as they were set to 1.0. This should result in a quicker response compared to the original gains, leaving poor tuning of the integral action as a probable cause of the deviation. Moreover, this is an example of one drawback with the method used for validation: Such deviations are not easily brought to attention when only comparing metrics reflecting the overall behavior.

The model changes in σ_{opt} lead to a larger heading time constant than the original simulator model. Consequently, the yaw rate behavior is improved, at least during the initial excitation. Nevertheless, σ_{opt} is unable to capture the experimental heading dynamics. One possible explanation for the experimental heading dynamics may be high frequent measurement noise from the GNSS. The measurements are not filtered in the system. Another possible explanation for the deviation in heading dynamics (experimental data compared to σ_{opt}), may be that the milliAmpere ferry isn't directional stable in yaw. The cause may be the shape of the hull, as well as the flat keel of the ferry. How these effects, in combination with non-ideal water conditions, influence the heading dynamics may not be replicated properly in the simulator dynamics. Pedersen [2019] mentions that it takes roughly 0.40 seconds for the azimuth servo to respond to azimuth angle references during experiments. This time delay is not modeled in the simulator, the reason being that it is notoriously difficult to model. The lack of modeling the time delay may be another reason why the heading dynamics behave as nicely as they do during simulations. If a more realistic azimuth is desired, the azimuth models should be validated in detail and tuned accordingly in future work.

For the experimental data, the metrics of the control input gradients are very similar in magnitude. In the simulations, the metrics for the control input gradient in X_{ref} tends to be much larger in magnitude compared to the gradients in Y_{ref} and N_{ref}. The same is the case for the metrics in x^n and u (compared to y^n and ψ, and v and r, respectively). The larger metrics in x^n in particular may partly be caused by the stationary deviations seen in the experimental x^n in fig. 7.5. Consequently, when considering all 19 metrics, the most favorable model may be the model with the closest metric only in x^n, u and the control input gradient in X_{ref}, compared to experimental metrics.

The surge-decoupled maneuvering model implemented in the milliAmpere simulator deviates from the one presented in Pedersen [2019]. Consequently, the model in the latter could also have been tested as part of this task. Nevertheless, the goal of the task is to yield pointers to which subsystems are in need of tuning, thus validation of the surge-decoupled model from Pedersen [2019] is left for future work. Subsystems in the milliAmpere simulator in need of validation and tuning are the reference model in the guidance system (as this was not in use throughout the task), the azimuth angle model (in particular the transient behavior and the time delay) and the motor speed gains, as well as the thrust allocation algorithm. The damping matrix is another point of interest, as σ_{opt} (and two other well performing simulations) had alterations in this matrix.

7.3 The berthing scheme

This section will first present the experimental setup of the berthing scheme from May 10, 2021. Next, the results from the experiments will be presented, before a discussion of both the results and the berthing scheme follows.

7.3.1 Experimental testing of the berthing scheme

The berthing scheme presented in chapter 6 was tested on May 10, 2021. The milliAmpere ferry was used as the experimental platform, and the tests were situated in the confined waters in Havnebassenget, Trondheim. Figure 7.7 depicts the area in which the experiment was conducted, retrieved from Google Maps [n.d.], with the tip of Hurtigbåtterminalen depicted in fig. 7.8. During these experimental tests, the wind velocity was about $3\,\mathrm{m\,s^{-1}}$, with gust velocities upwards to $4\,\mathrm{m\,s^{-1}}$. The waters in the harbor were calm, with no boats passing in proximity to the milliAmpere ferry during the experiment. The ferry was influenced by a current, as is often the case in the waters in Havnebassenget. The parameter values used throughout the berthing scheme have been found through extensive testing in the simulator.

The parameters for the two ellipses used during the experiments on May 10 are summarized in table 7.5.

Phase	Parameter		Parameter value
APPROACH	a	=	$1.0\,\mathrm{m}$
	b	=	$0.5\,\mathrm{m}$
	φ	=	$42.05\,\mathrm{deg}$
BERTHING	a	=	$4.0\,\mathrm{m}$
	b	=	$1.0\,\mathrm{m}$
	φ	=	$42.05\,\mathrm{deg}$

Table 7.5: The parameters used for transitions between the phases in the berthing scheme, during the experiments on May 10.

The angle α_{quay} was measured to be $137.95°$ on May 10, prior to conducting the experimental trials. This was done by steering the milliAmpere ferry towards Hurtigbåtkaia, keeping the bow of the ferry parallel to the quay when the fenders mounted on the quay were hit, and reading off the heading measurement from the dual-antenna GNSS. Consequently, $\varphi = 180° - 137.95° = 42.05°$ from eq. (6.6) for both transitions.

The values of the berthing parameters defined in chapter 6 were the following during the experiment:

$$\boldsymbol{\eta}_{\text{WP,approach}} = \begin{bmatrix} -44.0 & -120.0 & 137.95° \end{bmatrix}^\top \tag{7.2}$$

$$\boldsymbol{\eta}_{\text{WP,berthing}} = \begin{bmatrix} -46.5 & -119.0 & 137.95° \end{bmatrix}^\top \tag{7.3}$$

$$\boldsymbol{\nu}_{d,\text{berthing}} = \begin{bmatrix} 0.15 & 0.00, 0.00 \end{bmatrix}^\top \tag{7.4}$$

$$\boldsymbol{\tau}_{\text{quay}} = \begin{bmatrix} 25\,\text{N} & 0\,\text{N} & 0\,\text{N} \end{bmatrix}^\top \tag{7.5}$$

The heading values of the waypoints given in eqs. (7.2) and (7.3) were set equal to α_{quay}. In addition, the control input references in eq. (7.5) were large enough for the milliAmpere to reach the quay in simulations, albeit deemed small enough to damage neither the ferry nor the quay structure if collisions would occur during the experiments.

During the experiments on May 10, the last supervisor mode in the system before the berthing scheme started and the APPROACH phase was initiated, was the *Joystick* mode. The reason being that the remote control was used to navigate the ferry to the canal between the breakwater at Brattøra and the tip of Hurtigbåtkaia. This initial mode transition, from *Joystick* to *DP*, didn't take place during the development of the scheme in the simulator. Instead, in the simulations the system started out with a predefined initial pose in the area between the breakwater and quay, while the supervisor mode changed from *Direct actuator control* to *DP* when initiating the APPROACH phase.

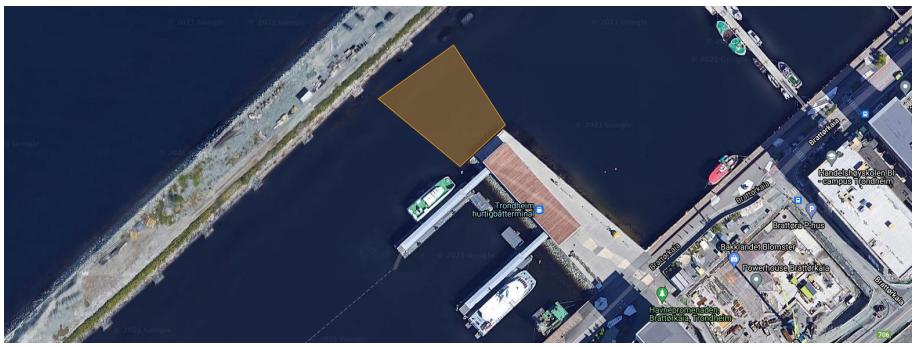

Figure 7.7: Map of Havnebassenget, Trondheim. The area in which the experiment on May 10 was conducted is marked as an orange polygon. *Google Map data ©2021, CNES / Airbus, Maxar Technologies.*

Figure 7.8: The tip of Hurtigbåtterminalen at which the berthing scheme was experimentally tested, depicted by the author. The width of the quay structure is approximately 18 meters.

7.3.2 Results

Figures 7.9–7.11 show the pose, velocity and control input references from the experiment on May 10, respectively. In these aforementioned figures, the yellow dotted vertical line marks when transition from the APPROACH to the BERTHING phase takes place. Likewise, the green dotted vertical line marks the transition from the BERTHING to the QUAY phase.

In fig. 7.9, discontinuous jumps in the references and deviations between the measured states and their references are shown during both the APPROACH and BERTHING phases. These will be discussed in section 7.3.3. The sudden acceleration seen at the end of fig. 7.10 coincided with the milliAmpere ferry hitting the quay structure. Furthermore, distinct discontinuous jumps in both $\dot{x}^n_{ref}$ and $\dot{y}^n_{ref}$ can be seen after transition to the BERTHING phase took place.

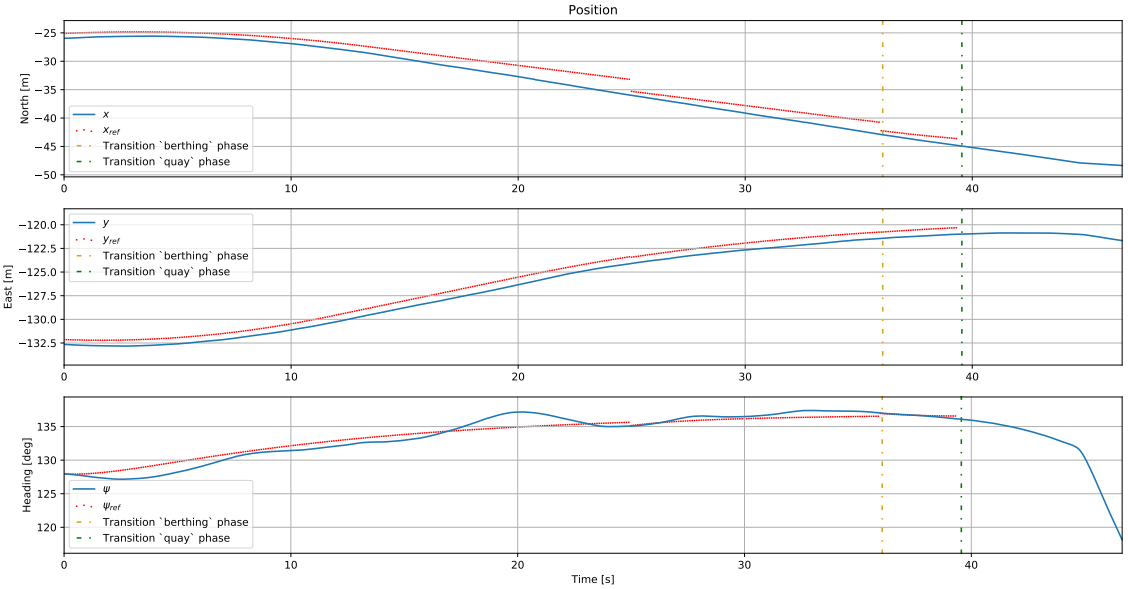

Figure 7.9: The pose (blue) of the milliAmpere ferry during the experiments on May 10, together with the references (red). The yellow dotted line marks the transition to the BERTHING phase, while the green dotted line marks the transition to the QUAY phase.

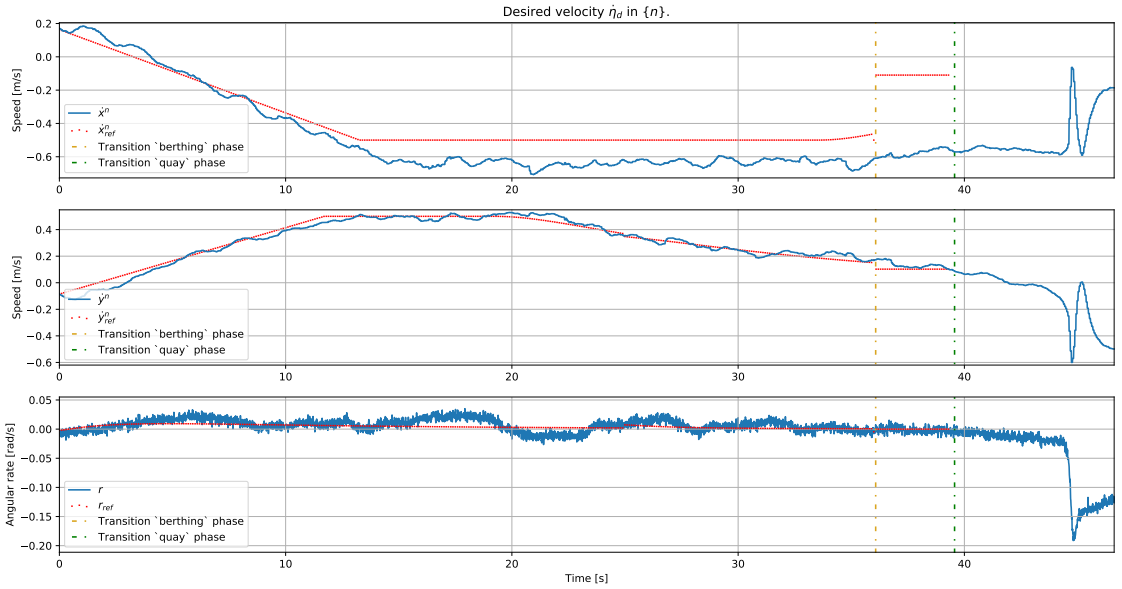

Figure 7.10: The velocities (blue) of the milliAmpere ferry during the experiments on May 10, together with the references (red). The yellow dotted line marks the transition to the BERTHING phase, while the green dotted line marks the transition to the QUAY phase. Velocities and the references are all given in $\{n\}$.

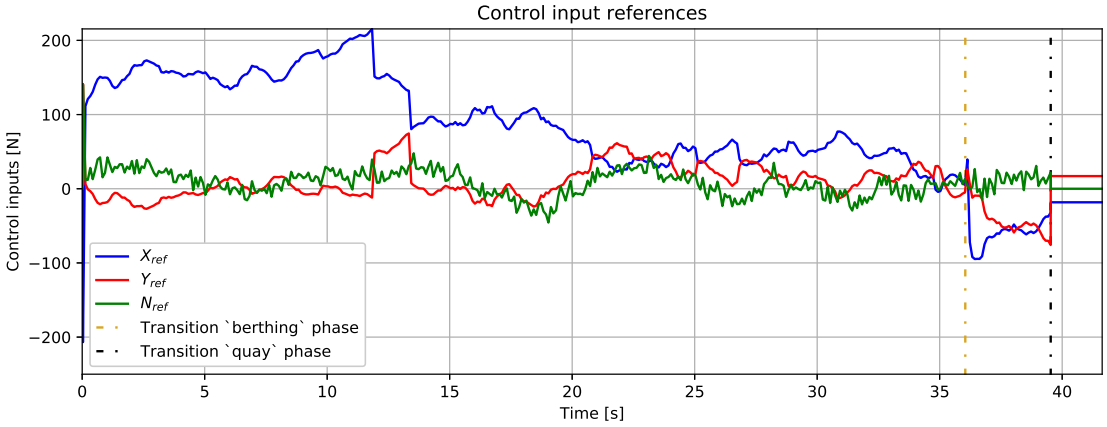

Figure 7.11: The control input references in surge (blue), sway (red) and yaw (green) during the experiments on May 10. The yellow dotted line marks the transition to the BERTHING phase, while the green dotted line marks the transition to the QUAY phase.

7.3.3 Discussion

First, the experimental results will be discussed, followed by a discussion regarding the phases of the berthing scheme and issues experienced during the experimental trials. Next, a discussion of the phase transitions is given. Lastly, a brief discussion of the overall berthing scheme is presented.

The experimental results

The discontinuous jumps in x^n_{ref} and ψ_{ref} in fig. 7.9 during the APPROACH phase may be caused by a smallest signed angle (SSA) error. This was discovered after the experiments on May 10. The SSA algorithm is briefly presented in appendix E, and was implemented using the Python library `NumPy`. At one point, when declaring the error pose $\tilde{\boldsymbol{\eta}} = \boldsymbol{\eta} - \boldsymbol{\eta}_{ref}$ in the DP system, the full pose vector was sent as input to the SSA function, and not just $\tilde{\psi} = \psi - \psi_{ref}$. As the `NumPy` library was utilized in the declaration of the function, and the error state was declared as a `NumPy` array, this did not yield a syntax error during runtime. Instead, the SSA method was performed element-wise on the error pose vector. The reference jumps most likely take place when $\|\tilde{\boldsymbol{\eta}}\| = \pi$, due to the system using radians for angles (as well as radians being a default input parameter to the SSA algorithm). This is deemed to not have any major impact on the overall behavior on the berthing scheme, apart from being a likely explanation of the stationary deviation in x^n and y^n in fig. 7.9 during the APPROACH phase.

The discontinuous jump in $\dot{x}^n_{ref}$ and $\dot{y}^n_{ref}$ in fig. 7.10 is due to the berthing scheme not considering the velocities of the ferry during the transition from the APPROACH to the BERTHING phase, when the desired velocities defined in eq. (6.3) are set. This is one example where bumpless transfer or gain scheduling, as briefly summarized in section 6.3.1, could be utilized. Another example where such techniques would be relevant is the control input references set during the transition from the BERTHING to the QUAY phase, depicted in fig. 7.11. Implementation of such techniques is left for future work.

The velocities and references in fig. 7.10 are given in $\{n\}$. The system publishes velocities and velocity references in $\{n\}$, from the navigation and guidance system, respectively. The deviation in $\dot{x}^n_{ref}$ may not be as large as depicted if rotated to $\{b\}$, which is the reference frame used internally by the DP system. The deviation seen in $\dot{x}^n_{ref}$ may be distributed more equally in surge and sway, both during the APPROACH and BERTHING phases. Moreover, the velocity deviation during the BERTHING phase likely originate from the DP controller not being given enough time to follow the velocity references, as the duration of the BERTHING phase is too short. This, in turn, is a direct consequence of the waypoints $\boldsymbol{\eta}_{\text{WP,approach}}$ and $\boldsymbol{\eta}_{\text{WP,berthing}}$ being set too close to each other during the experimental trials, combined with the saturation on the acceleration references in the reference model. As requirements on the maximum velocities before phase transitions can take place are not implemented as of now, the speed and moment of inertia in surge result in the duration of the BERTHING phase being drastically shortened. The BERTHING phase should be initiated further away from the quay, in order to give the DP controller

time to reach the desired velocities. In addition, lower desired velocities in $\{b\}$ during this phase than those given in eq. (7.5), around $0.05\,\mathrm{m\,s^{-1}}$ in surge, may be advantageous.

The phases of the berthing scheme

During the BERTHING phase, conflict between the position references from the reference model and the velocity reference set manually may arise, especially given that the acceleration references were set to zero. The velocity references set before the BERTHING phase are rotated from $\{b\}$ to $\{n\}$. Consequently, ψ and not α_{quay} should be the angle with which these references are rotated. This, in turn, may make the scheme more robust, and contribute to the ferry reaching the quay head-on, as intended. Another option during the BERTHING phase, is to set only the damping gain in surge to zero in the DP controller. Thus, deviations from surge velocity references are not punished, but instead position control may improve.

During the QUAY phase, it became clear that the milliAmpere ferry is dependent on little to no current and wind, in order to successfully reach the berth. Control in sway and heading is not maintained during this phase as of now, meaning that the ferry is especially prone to arrive at the berth with an unsatisfactory heading, i.e. $\psi \neq \alpha_{\text{quay}} \pm 2°$. To arrive at the berth with an offset in x^n or y^n is deemed acceptable at this point of the proof of concept. Only small changes in heading, due to current or wind, will in turn lead to an unsatisfactory pose at the berth, in worst case resulting in hitting the quay before being pushed away from the quay. One way to improve the QUAY phase would be to have the DP controller publish control input references in sway and heading, while commanding a constant control input in surge only. This solution assumes no conflict arises in the control inputs from the DP controller and the surge force set manually.

The desired surge velocity u_d commanded during the BERTHING phase, as well as the constant control input reference used during the QUAY phase, were determined through simulations only. One better approach would be to e.g. use MPC after initialization of the system, but before the APPROACH phase starts. The optimal u_d and $\boldsymbol{\tau}_{\text{quay}}$ which results in a desired berthing pose could then be calculated.

The phase transitions

One challenge experienced in the experiments was faulty behavior during the mode switches in the system supervisor. Such mode switches take place when transitioning to the APPROACH phase after initialization, and when transitioning between the APPROACH and BERTHING phase. It was experienced that the system started straight in the second phase, when it should have started in the first phase. The timing of publishing waypoints was another issue. If the berthing scheme published a waypoint when the system was in *joystick* mode, the guidance system tended to ignore said waypoint when the mode shortly after was automatically switched to *DP* mode. One possible explanation of why this behavior haven't been discovered in the simulator, is that the system is restarted between each simulation during development of the berthing scheme. This is not the case during

experiments, as turning the whole system off and on again when not moored to a quay is considered hazardous.

When the supervisor mode changes to *DP* during initialization of the berthing scheme, the force component from the integrator term in the DP controller is reset to zero. In previous written code, this is explicitly stated to happen only when transitions to the *DP* mode takes place. Consequently, it does not take place when the supervisor mode is switched to *Berthing* between the APPROACH and BERTHING phase. The effect of this reset would most likely have less impact in the simulator, due to the ideal environments (hydrodynamic effects in the water, no environmental forces and moments, etc.). The same may not be said for the environment in which the experiments take place, where hydrodynamic effects may be substantial, in particular close to quay walls and underwater obstacles, in addition to environmental forces and moments. Examples of such hydrodynamic effects include the bank and bank-cushion effects, the shallow water effect and the squat effect. A summary of these are presented in Knudsen [2020, pp.9-10].

Due to uncertainty regarding mode switches of the milliAmpere system, the berthing scheme should rather depend solely on message sending and Boolean flags for communicating phase transitions. The system supervisor should always remain in the *DP* mode. After the initial experiment on April 19, the author discovered that the guidance node only was active when the mode is set to *DP*, consequently not publishing reference data otherwise. This was one of the main reasons for the second iteration of tests on May 10, and may be an issue in other parts of the milliAmpere system as well. Additionally, different reference frames are used by different subsystems. Information published over topics in one frame may not be the same reference frame used internally in a subsystem utilizing that information, complicating development in general.

The experiments highlighted that message sending is one of the key ROS features yielding a method which scales well, regardless of the size of the vessel, its speed, the configuration of the quay, etc., in addition to avoiding problems with the supervisor state machine. One aspect to consider when publishing important flags to the system during the berthing scheme, is to avoid interruption of the publication by the ROS framework. This happened during one experimental trial, resulting in conflict during the QUAY phase between the constant control input references published from the berthing supervising node, and the DP system (which was meant to be deactivated). This didn't happen in the simulator during development, and the reason is most likely twofold: (1) Such timing issues seldom occur in general; and (2) there may be more nodes running with a higher frequency during the experiment (e.g. the navigation system, the IMU and the GNSS). A timing issue may occur more frequently when the critical resource, time, is in greater demand in the system in general. The Python module `threading` enables mutex-like behavior, locking the threads of the system such that a flag may be set and published, before other threads may run. This is another important aspect to consider for future work. In order to improve the system behavior during phase transitions, regardless of using mode switches or messages, would be to implement bumpless transfer and/or gain scheduling, as briefly introduced in section 6.3.1.

The berthing scheme overall

The general berthing scheme proved to be flexible and scalable, as it is developed without assumptions regarding neither the size and the speed of the vessel, nor the quay structure at which berthing takes place. Moreover, the ellipses which define where phase transitions take place can be configured to fit any given quay structure. The two waypoints can be set at any configuration and distance from each other, and the desired velocity and control input references may be changed such that docking along sway can be achieved (as opposed to docking along surge, as in this thesis). Lastly, the scheme is based upon only minor changes in GNC subsystems already implemented in marine surface crafts, with only the berthing supervising node needed to be included. This highlights the modular advantages of the berthing scheme.

A reason the development of the berthing scheme in the simulator went more smoothly and was less problematic compared to the experimental trials, could be the thrust allocation algorithm. In the simulator, the relationship between the control force one expect to get, and the force which is actually delivered by the actuators, is assumed to be perfect. During experimental trials, hysteresis in the actuators is a prime example which needs to be taken into account. Additionally, the various hydrodynamic effects briefly mentioned previously are not modeled in the simulator, and may be a contributing factor to the difficulties with reaching the berth during the experiments.

The reference model in eq. (4.10) used by the guidance system needs to be investigated. According to Fossen [2011, p.251], nonlinear damping can be included in the reference model given in eq. (4.10), which may lead to reduced velocities for large step amplitudes in the inputs $\boldsymbol{r}^n$. Furthermore, tuning of the relative damping ratios given in eq. (4.11) and the natural frequencies in eq. (4.12) is most likely necessary.

Chapter 8

Conclusion and future work

This chapter will conclude the work conducted in the thesis, before presenting proposals for future work for each of the three main tasks.

8.1 Conclusion

The wake wave model presented in this thesis has tried to model the wave forces and moments themselves, not the influence they have in the navigation system. Consequently, it may be used regardless of the design of the navigation system. In the literature, wave spectra and RAOs are commonly used and have been thoroughly studied. That being said, more basic and easier-to-use wave models may be desirable in some applications. The wake model is an example of such.

Model validation is a notoriously challenging task, with advantages and disadvantages related to each of the common approaches. One challenge is that a model with sufficient accuracy for some experimental conditions, does not imply that the model is valid in the whole applicable domain. In addition, replication of experimental data, as well as validation of the results, may be achieved in different ways. This thesis presents only one option for replication and validation.

The motivation behind autonomous docking in general includes safety improvements, reducing stress and risk for the crew, energy consumption, among others. The berthing scheme presented in this thesis is only partly autonomous, as only two of the four phases of the docking operation are considered. That being said, it may prove to relief the crew of the marine crafts utilizing the scheme. Each of the four phases of docking utilizes different technologies, some which may be more refined and mature than others, and this berthing scheme needs refinements before it can prove its versatility.

8.1.1 The three main tasks of the thesis

- First- and second-order wave-induced forces and moments were implemented, as no such models were present in the milliAmpere simulator. The former tries to

replicate wake wave forces originating from nearby passing marine crafts, typical of the environment in which the milliAmpere ferry operates. The second-order wave model is a sum of a stationary value and a dynamic contribution. Both wave models were tested through three DP stationkeeping simulations, yielding appropriate behavior in all three degrees of freedom. The wake wave models may be used as presented, or as inspiration of other ways of direct modeling of wave forces and moments.

- The validation task was restricted in extent, due to the vast number of parameters which may contribute to the model discrepancies discovered during the specialization project [Knudsen, 2020]. The heading time constant of the most favorable model was significantly improved, compared to the original simulator model. Nevertheless, the task concluded that the azimuth angle models and motor speed gains, the reference model, the damping matrix and the thrust allocation algorithm should be in focus for later model validation and tuning work.

- The proposed berthing scheme has been designed for flexibility, scalability, and modularity. This has been emphasized through experimental trials. Given the experimental results from May 10, the goal of docking head-on may only partly be achieved. The main reason being that the scheme is prone to ocean currents and wind forces and moments, and that control in heading is not maintained during the QUAY phase. With this in mind, a proof of concept is not completely ready yet. That being said, the thesis presents several tangible improvements and techniques for future work on the berthing scheme. Optimally, maintaining control in both sway and heading should be implemented in the QUAY phase, and bumpless transfer or gain scheduling is needed for improvement of the transients during the phase transitions.

8.2 Future work and continuation

Lastly, proposals for the continuation and refinement of this work will be presented. For readability, these proposals will be split into separate bullet lists, one for each main task.

8.2.1 The wave models and environmental forces

- Tuning of the DP controller, in order to better counteract the wave forces and moments implemented in the simulator during this thesis.

- Include hydrodynamic models and test the berthing scheme when hydrodynamic forces act on the milliAmpere ferry during berthing. This is to get a better understanding of the acting hydrodynamic forces in different scenarios. Such models may include a force reflected by the quay structure itself, or models of net wave forces influencing the ferry after it has been moored. Models of e.g. the squat effect, the shallow water effect or the bank and bank cushion effects may also be of interest.

- Transit tests between two waypoints, with distance 50–200 meters in-between, when the wave models are active.
- Investigate which combinations of environmental forces (trying different magnitudes, angles of attack, etc.) that influence the milliAmpere ferry the most during the berthing phase, using the wind, wave and ocean current models in the simulator.

8.2.2 Validation of the simulator models

- Work dedicated to improving the simulator models further, e.g. by use of model-predictive control or an iteration of an optimization-based model identification. This should include validation of the surge-decoupled model presented in Pedersen [2019].
- Investigate how the heading dynamics in the simulator could resemble the experimental heading dynamics, e.g. by validation and tuning of the model of the azimuth model and the unmodeled time delay identified by Pedersen [2019]. This assumes that the oscillatory heading dynamics from the experiment conducted by Bjørn-Olav Holtung-Eriksen on December 1, 2020 is not caused by GNSS measurement noise and similar. If so, stochastic noise models could be implemented in the navigation system used for simulations.
- To validate and tune the behavior of the guidance system [1].

8.2.3 The berthing scheme

- Bumpless transfer or gain scheduling must be implemented for phase transitions. This should include consideration of the velocities of the ferry during the BERTHING phase, when the velocity reference is set.
- Include a collision avoidance technique, as well as a more refined way of detecting when the ferry makes contact with the quay, in order to encompass all four phases of a docking operation as presented in section 1.5.
- Utilize the short-range ultrasonic distance sensors mounted on the milliAmpere ferry during the QUAY phase, for improved safety.
- Mutexes should be implemented when publishing Boolean flags, for fault tolerance.
- Refine the berthing scheme such that control is maintained in sway and heading during the quay phase.
- Calculate the optimal u_d and $\boldsymbol{\tau}_{\text{quay}}$ which will result in a desired berthing pose, during the initialization of the berthing scheme.

[1] Andreas Aurlien, a fellow master student at ITK, improved the behavior of the reference model in the guidance system by tuning the reference model matrices $\boldsymbol{\Delta} = \text{diag}(1.0, 1.0, 1.0)$ and $\boldsymbol{\Omega} = \text{diag}(0.2, 0.2, 0.2)$ during the work of his master's thesis. These values indicate that tuning of the reference model can lead to improvement.

Bibliography

T. Abramowicz-Gerigk. Experimental study on the hydrodynamic forces induced by a twin-propeller ferry during berthing. *Ocean engineering*, 35(3-4):323–332, 2008.

J. F. Alvarez, T. Longva, and E. S. Engebrethsen. A methodology to assess vessel berthing and speed optimization policies. *Maritime Economics & Logistics*, 12(4):327–346, 12 2010.

S. R. Aune. Development and Simulation of an Autonomous Docking System for Unmanned Surface Vehicles (USV). Master's thesis, NTNU, 2019.

J. G. Balchen, N. A. Jenssen, and S. Sælid. Dynamic positioning using Kalman filtering and optimal control theory. In *IFAC/IFIP Symposium on Automation in Offshore Oil Field Operation*, pages 183–188, Amsterdam, Holland, 1976.

J. G. Balchen, N. A. Jenssen, E. Mathisen, and S. Sælid. A Dynamic Positioning System Based on Kalman Filtering and Optimal Control. *Modeling, Identification and Control*, 1(3):135–163, 1980.

J. G. Balchen, T. Andresen, and B. Foss. *Reguleringsteknikk*. NTNU Grafisk Senter, 6th edition, 2016.

M. R. Benjamin and J. A. Curcio. COLREGS-based navigation of autonomous marine vehicles. In *2004 IEEE/OES Autonomous Underwater Vehicles (IEEE Cat. No.04CH37578)*, pages 32–39, 2004.

S. B. Bentzrød. Fergene er hypermoderne. Men de sliter tilsynelatende veldig med å legge til kai. *Aftenposten*, 2019. URL `https://www.aftenposten.no/norge/i/pLlG4E/fergene-er-hypermoderne-men-de-sliter-tilsynelatende-veldig-med-aa-leg`. Published August 8, 2019. Accessed June 1, 2021.

G. Bitar, A. B. Martinsen, A. M. Lekkas, and M. Breivik. Trajectory Planning and Control for Automatic Docking of ASVs with Full-Scale Experiments, 2020.

C. Bohn and D.P. Atherton. An analysis package comparing PID anti-windup strategies. *IEEE Control Systems Magazine*, 15(2):34–40, 1995.

M. Breivik. *Topics in guided motion control of marine vehicles*. PhD thesis, Norwegian University of Science and Technology, 2010.

M. Breivik and T. I. Fossen. Principles of guidance-based path following in 2d and 3d. In *Proceedings of the 44th IEEE Conference on Decision and Control*, pages 627–634, 2005.

M. Breivik, J. P. Strand, and T. I. Fossen. Guided dynamic positioning for fully actuated marine surface vessels. *Proceedings of the 6th IFAC MCMC, Lisbon, Portugal*, 2006.

R. G. Brown and P. Y. C Hwang. *Introduction to random signals and applied Kalman filtering*. John Wiley & Sons, Inc., 4th edition, 2012.

M. Caccia. Autonomous surface craft: prototypes and basic research issues. In *2006 14th Mediterranean Conference on Control and Automation*, pages 1–6, 2006.

T. Chai and R. R. Draxler. Root mean square error (RMSE) or mean absolute error (MAE)? – Arguments against avoiding RMSE in the literature. *Geoscientific model development*, 7(3):1247–1250, 2014.

M. J. Csorba. How to achieve type approval for cyber security. `https://www.dnv.com/expert-story/maritime-impact/How-to-achieve-type-approval-for-cyber-security.html`, 7 2020. Accessed March 8, 2021.

A. Devaraju, L. Chen, and R. R. Negenborn. Autonomous surface vessels in ports: Applications, technologies and port infrastructures. In *Computational Logistics*, pages 86–105. Springer International Publishing, 2018.

C. Edwards and I. Postlethwaite. Anti-windup and bumpless-transfer schemes. *Automatica*, 34(2):199–210, 1998.

O. Egeland and T. Gravdahl. *Modeling and Simulation for Automatic Control*. Tapir Trykkeri, Trondheim, Norway, 2002.

F. El-Hawary. *The ocean engineering handbook*. Crc Press, 2000.

E. Eliopoulou, A. Papanikolaou, and M. Voulgarellis. Statistical analysis of ship accidents and review of safety level. *Safety Science*, 85:282–292, 2016. ISSN 0925-7535.

T. I. Fossen. *Handbook of Marine Craft Hydrodynamics and Motion Control*. John Wiley & Sons, Ltd, West Sussex, United Kingdom, 1st edition, 2011.

T. I. Fossen. *Handbook of Marine Craft Hydrodynamics and Motion Control*. John Wiley & Sons, Ltd, West Sussex, United Kingdom, 2nd edition, 2021.

M. Furat and İ. Eker. Computer-aided experimental modeling of a real system using graphical analysis of a step response data. *Computer Applications in Engineering Education*, 22(4):571–582, 2014.

Google Maps. Map of Havnebassenget, Trondheim, n.d. Accessed May 28, 2021.

V. Hassani, A. J. Sørensen, A. M. Pascoal, and A. P. Aguiar. Multiple model adaptive wave filtering for dynamic positioning of marine vessels. In *2012 American Control Conference (ACC)*, pages 6222–6228, 2012.

Hemisphere GNSS, Inc. Vector™ VS330 GNSS Receiver data sheet. https://www.hemispheregnss.com/wp-content/uploads/2020/06/hemispheregnss_vs330_datasheet_web.pdf, 7 2019. Accessed February 25, 2021.

F. H. Hsu and K. A. Blenkarn. Analysis of peak mooring forces caused by slow vessel drift oscillations in random seas. *Society of Petroleum Engineers Journal*, 12(04):329–344, 1972.

P. Janssen. *The interaction of ocean waves and wind*. Cambridge University Press, 2004.

R. E. Kalman. A New Approach to Linear Filtering and Prediction Problems. *Journal of Basic Engineering*, 82(1):35–45, 1960.

I. Kaminer, A. M. Pascoal, P. P. Khargonekar, and E. E. Coleman. A velocity algorithm for the implementation of gain-scheduled controllers. *Automatica*, 31(8):1185–1191, 1995.

E. Kløvning. Wind affecting berthing operations. *TransNav, the International Journal on Marine Navigation and Safety of Sea Transportation*, 14(3):721–725, 2020.

S. K. Knudsen. Berthing of an unmanned surface vessel influenced by environmental forces, 2020. Unpublished specialization project.

Kongsberg Maritime. Automatic ferry enters regular service following world-first crossing with passengers onboard. https://www.kongsberg.com/maritime/about-us/news-and-media/news-archive/2020/first-adaptive-transit-on-bastofosen-vi/, 02 2020. Accessed May 2, 2021.

Y. Kuwata, M. T. Wolf, D. Zarzhitsky, and T. L. Huntsberger. Safe Maritime Autonomous Navigation With COLREGS, Using Velocity Obstacles. *IEEE Journal of Oceanic Engineering*, 39(1):110–119, 2014.

K. Lindegaard. *Acceleration feedback in dynamic positioning*. PhD thesis, Norwegian University of Science and Technology, 2003.

Z. Liu, Y. Zhang, X. Yu, and C. Yuan. Unmanned surface vehicles: An overview of developments and challenges. *Annual Reviews in Control*, 41:71–93, 2016. ISSN 1367-5788.

A. B. Martinsen, A. M. Lekkas, and S. Gros. Autonomous docking using direct optimal control. *IFAC-PapersOnLine*, 52(21):97–102, 2019. ISSN 2405-8963. 12th IFAC Conference on Control Applications in Marine Systems, Robotics, and Vehicles CAMS 2019.

A. B. Martinsen, G. Bitar, A. Lekkas, and S. Gros. Optimization-Based Automatic Docking and Berthing of ASVs Using Exteroceptive Sensors: Theory and Experiments. *IEEE Access*, 8:204974 – 204986, 11 2020.

N. Mizuno, Y. Uchida, and T. Okazaki. Quasi real-time optimal control scheme for automatic berthing. *IFAC-PapersOnLine*, 48(16):305–312, 2015.

E. Murdoch, C. Clarke, and I. W. Dand. *A Master's Guide To: Berthing*. Standard House, 2nd edition, 2 2012.

Norwegian Coastal Administration. Havnestruktur. `https://kystverket.no/Maritim-infrastruktur/Havner/Klassifisering-av-havner/`, 2016. Accessed May 11, 2021.

NTNU. Autoferry NTNU. `https://www.ntnu.edu/autoferry/about`, n.d. Accessed February 4, 2021.

A. C. Paixão and P. B. Marlow. Strengths and weaknesses of short sea shipping. *Marine Policy*, 26(3):167–178, 2002. ISSN 0308-597X.

A. A. Pedersen. Optimization based system identification for the milliampere ferry. Master's thesis, Norwegian University of Science and Technology NTNU, Trondheim, Norway, 6 2019.

S. Saelid, N. Jenssen, and J. Balchen. Design and analysis of a dynamic positioning system based on Kalman filtering and optimal control. *IEEE Transactions on Automatic Control*, 28(3):331–339, 1983.

Saildrone, Inc. Saildrone USV Completes First Atlantic Crossing East to West. `https://www.saildrone.com/news/first-autonomous-vehicle-atlantic-crossing-east-west`, 10 2019. Accessed February 17, 2021.

Saildrone, Inc. What is a Saildrone? `https://www.saildrone.com/technology/vehicles`, 2021. Accessed March 1, 2021.

R. G. Sargent. Verification and validation of simulation models. In *Proceedings of the 2010 winter simulation conference*, pages 166–183. IEEE, 2010.

Y. Shuai, G. Li, J. Xu, and H. Zhang. An Effective Ship Control Strategy for Collision-Free Maneuver Toward a Dock. *IEEE Access*, 8, 2020. doi: 10.1109/ACCESS.2020.3001976.

SNAME. Nomenclature for Treating the Motion of a Submerged Body Through a Fluid. *Technical and Research Bulletin No. 1–5*, 1950.

J. Spange. Autonomous docking for marine vessels using a lidar and proximity sensors. Master's thesis, NTNU, 2016.

G. Thorsnæs. Norges geografi i *Store norske leksikon* på snl.no. https://snl.no/Norges_geografi, 8 2020. Accessed May 11, 2021.

S. A. Værnø, R. Skjetne, Ø. K. Kjerstad, and V. Calabrò. Comparison of control design models and observers for dynamic positioning of surface vessels. *Control Engineering Practice*, 85:235–245, 2019. ISSN 0967-0661.

J. Werner. How to drive and dock a boat in current. https://www.allatsea.net/how-to-drive-a-boat-in-current/, 9 2020. Accessed May 27, 2021.

Yara. The first ever zero emission, autonomous ship. https://www.yara.com/knowledge-grows/game-changer-for-the-environment/, 03 2018. Accessed February 17, 2021.

Yara. Yara Birkeland press kit. https://www.yara.com/news-and-media/press-kits/yara-birkeland-press-kit/, 11 2020. Accessed February 17, 2021.

L. Zaccarian and A. R. Teel. A common framework for anti-windup, bumpless transfer and reliable designs. *Automatica*, 38(10):1735–1744, 2002.

Appendix A

Experimental data used for model validation

This appendix contains plots of the experimental data from 1 December, 2020. The experiment was conducted by Bjørn-Olav Holtung-Eriksen, and not by the author. The time axes in figs. A.1 and A.2 are given in Unix time, i.e. the number of seconds since 01 January, 1970 excluding leap seconds. The former plot depicts the pose of the milliAmpere ferry, while the latter shows the velocities.

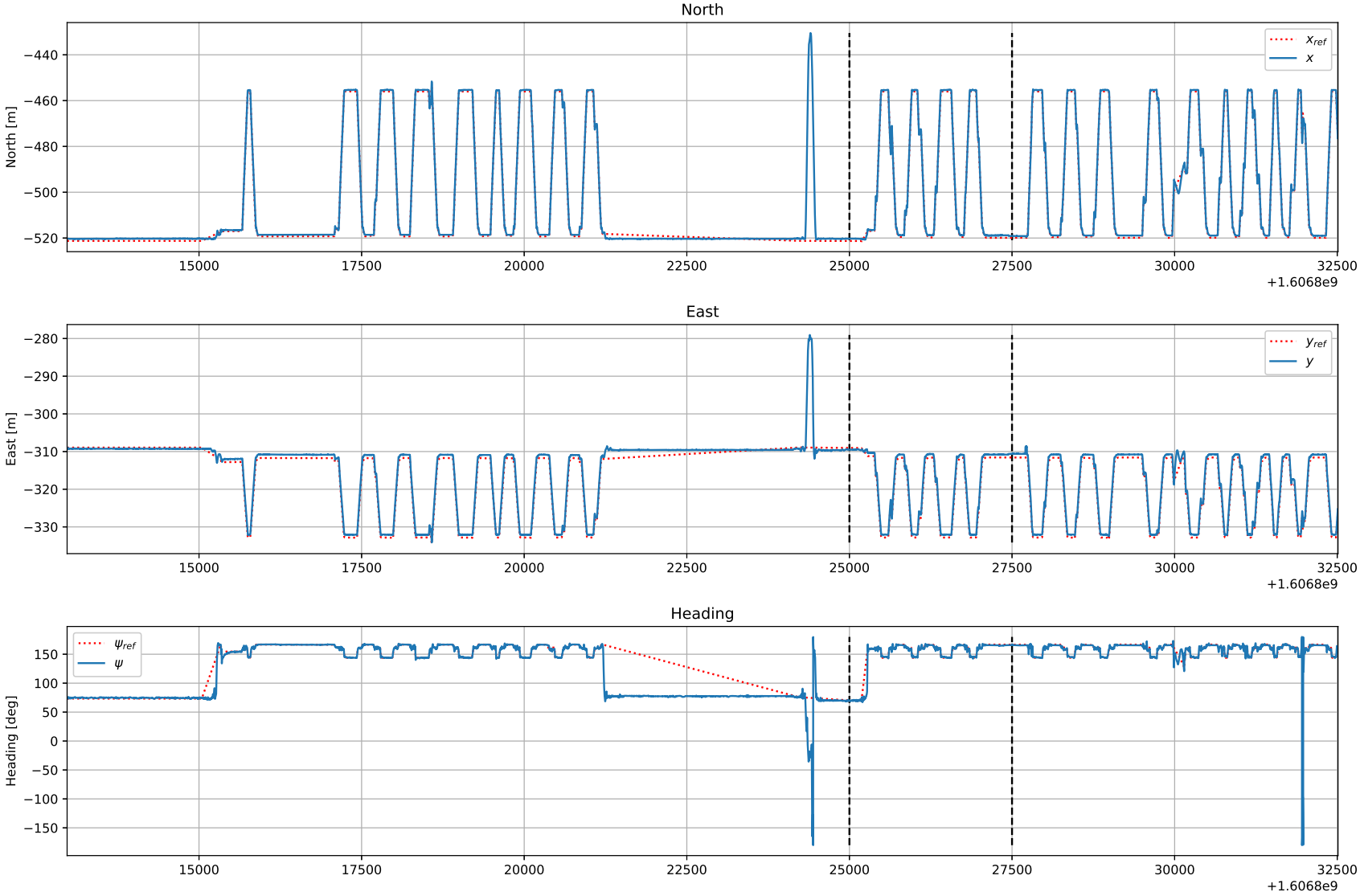

Figure A.1: The pose of the milliAmpere ferry during the experiments performed by Bjørn-Olav Holtung Eriksen on December 1, 2020. The time interval between the two black dotted lines marks the data the validation task in this thesis replicated. The time axis is given in Unix time.

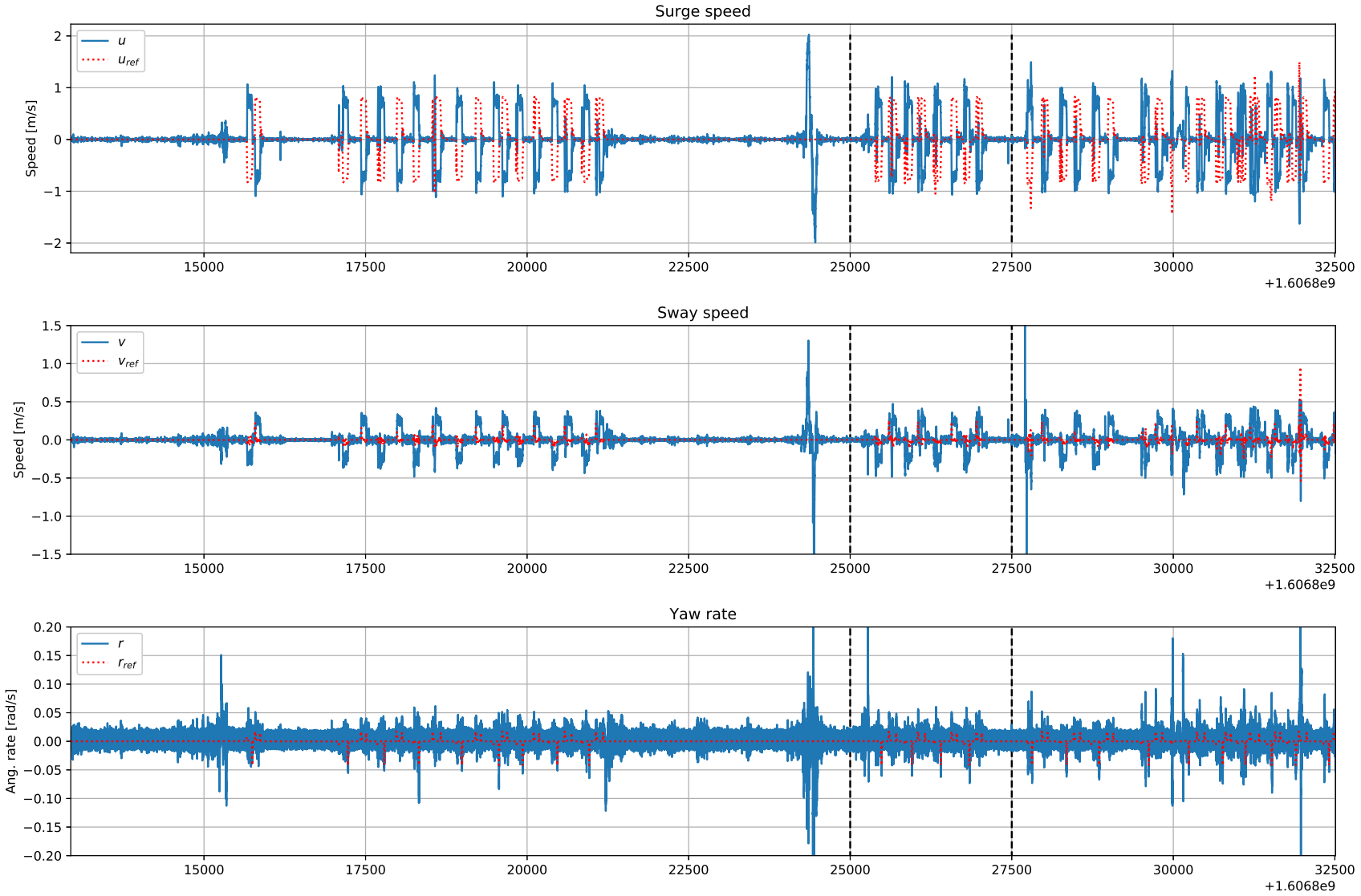

Figure A.2: The velocities of the milliAmpere ferry during the experiments performed by Bjørn-Olav Holtung Eriksen on December 1, 2020. The time interval between the two black dotted lines marks the data the validation task in this thesis replicated. The time axis is given in Unix time.

Appendix B

Validation results and metrics from 35 simulation

This appendix contains the following four tables:

- Table B.1 contains an overview of the parameter changes in each of the 35 simulations run during the valdiation task. An empty cell indicates that the given parameter value was unchanged from the experiment and the original simulator model. Furthermore, ϵ_i marked *NA* indicates that the azimuth dynamics only were the error states $\dot{\alpha}_i = \alpha_{d,i} - \alpha_i$.
- Table B.2 shows the heading time constant as well as RMSE and MAE values for the pose of the milliAmpere during each of the 35 simulations.
- Table B.3 shows the RMSE and MAE values for the velocities of the ferry during each of the 35 simulations.
- Table B.4 shows the RMSE and MAE values for the gradients of the control input references, for the 35 simulations.

In tables B.1–B.4, the most favorable model change is given in **bold** font and the least favorable model change is given in *italicized* font. Relevant data for the original simulator model and the experiment conducted by Bjørn-Olav Holtung-Eriksen are given as well, for comparison.

Parameter changes

Model	$\boldsymbol{M}$ *matrix*	*Motor speed*		*Azimuth angles*		$\boldsymbol{D}$ *matrix*			
No.	m_{33}	$K_{\omega,1}$	$K_{\omega,2}$	ϵ_1	ϵ_2	N_r	N_v	$N_{\|v\|v}$	$N_{\|v\|r}$
Exp. Orig.	4862	0.563	0.591	6.277	7.721	-142.7	7.34	-4.352	-122
1.	4660			*NA*	*NA*				
2.		1.0	1.0						
3.	4660	1.0	1.0						
4.			0.400						
5.			0.500						
6.			*0.300*						
7.		0.500	0.400						
8.			0.450						
9.			0.475						
10.	4660		0.400						
11.	5000		0.400						
12.		0.450	0.450						
13.	5200	0.450	0.450						
14.	5200	0.450	0.450					-24.352	
15.	5200	0.450	0.450		6.500			-24.352	
16.	5200	0.450	0.450		9.000			-24.352	
17.	5200	0.450	0.450	8.000	9.000			-24.352	
18.	5200	0.450	0.450	5.500	9.000			-24.352	
19.	5200	1.0	1.0					-24.352	
20.	5000	1.0	1.0					-24.352	
21.	5000	1.0	1.0					-24.352	-250
22.	5000	1.0	1.0					-24.352	-200
23.		**1.0**	**1.0**			**-250.0**			
24.		1.0	1.0			-250.0	8.50	-24.352	
25.						-250.0			
26.	5000	1.0	1.0			-250.0			
27.	4800	1.0	1.0			-225.0			
28.	4700	1.0	1.0			-250.0			
29.		1.0	1.0			-200.0			
30.		1.0	1.0			-180.0			
31.		1.0	1.0				15.0		
32.		1.0	1.0			-200.0	2.00		
33.		1.0	1.0			-200.0	15.0		
34.								-24.352	-200
35.	4660								

Table B.1: Parameter changes in all 35 simulations, for validation and tuning of the simulator models. The abbreviations *Exp.* and *Orig.* stand for experimental data and data using the original simulator model, respectively. The parameter values in these two cases are the same. Bold font symbolizes the most favorable model, while italicized text symbolizes the least favorable model.

		Pose					
		RMSE values			MAE values		
No.	$\hat{T}_\psi$ [s]	$\hat{x}^n$ [m]	$\hat{y}^n$ [m]	$\hat{\psi}$ [rad]	$\hat{x}^n$ [m]	$\hat{y}^n$ [m]	$\hat{\psi}$ [rad]
Experiment	6.30	2.212	1.152	0.070	1.607	0.983	0.033
Original	4.04	1.592	0.568	0.356	1.087	0.382	0.048
1.	3.70	1.804	0.756	0.914	1.226	0.466	0.230
2.	5.48	1.375	0.496	0.319	0.948	0.340	0.050
3.	3.96	1.377	0.492	0.335	0.939	0.333	0.050
4.	5.80	1.662	0.588	0.089	1.140	0.395	0.028
5.	4.20	1.634	0.578	0.349	1.113	0.390	0.046
6.	*3.76*	*2.368*	*0.950*	*1.378*	*1.759*	*0.716*	*0.465*
7.	4.04	1.702	0.602	0.375	1.163	0.403	0.054
8.	5.02	2.023	0.739	0.761	1.390	0.506	0.176
9.	3.68	1.639	0.591	0.516	1.099	0.379	0.084
10.	3.76	1.868	0.677	0.822	1.314	0.488	0.186
11.	5.22	2.105	0.882	0.937	1.532	0.609	0.230
12.	4.12	1.852	0.699	0.566	1.257	0.446	0.097
13.	4.96	1.885	0.672	0.332	1.291	0.460	0.075
14.	5.36	1.745	0.619	0.093	1.207	0.416	0.029
15.	3.62	2.225	0.878	0.828	1.621	0.607	0.194
16.	3.62	1.752	0.626	0.395	1.215	0.425	0.064
17.	4.78	2.094	0.765	1.015	1.463	0.529	0.264
18.	3.78	2.065	0.736	0.929	1.458	0.523	0.238
19.	4.46	1.423	0.510	0.331	0.974	0.347	0.050
20.	4.20	1.369	0.494	0.325	0.942	0.338	0.048
21.	4.90	1.389	0.500	0.219	0.949	0.341	0.031
22.	4.02	1.415	0.507	0.353	0.969	0.347	0.044
23.	**5.24**	**1.459**	**0.523**	**0.088**	**1.004**	**0.360**	**0.023**
24.	4.94	1.455	0.526	0.091	1.000	0.357	0.028
25.	5.18	1.697	0.602	0.103	1.173	0.403	0.041
26.	4.18	1.358	0.491	0.341	0.919	0.330	0.049
27.	3.82	1.429	0.513	0.349	0.953	0.342	0.046
28.	5.06	1.441	0.519	0.089	0.994	0.357	0.024
29.	4.66	1.366	0.495	0.263	0.942	0.338	0.035
30.	4.44	1.269	0.461	0.274	0.858	0.310	0.035
31.	4.44	1.412	0.507	0.282	0.972	0.350	0.035
32.	4.30	1.381	0.497	0.299	0.951	0.341	0.038
33.	4.54	1.407	0.506	0.316	0.943	0.337	0.045
34.	4.94	1.376	0.498	0.182	0.937	0.339	0.028
35.	5.02	1.763	0.674	0.148	1.160	0.439	0.040

Table B.2: Heading time constant T_ψ alongside RMSE and MAE values for the pose from 35 simulations, rounded off to three decimal places. Bold font symbolizes the most favorable model, while italicized text symbolizes the least favorable model.

	Velocities					
	RMSE values			MAE values		
No.	$\hat{u}$ [m/s]	$\hat{v}$ [m/s]	$\hat{r}$ [rad/s]	$\hat{u}$ [m/s]	$\hat{v}$ [m/s]	$\hat{r}$ [rad/s]
Experiment	0.171	0.062	0.017	0.097	0.040	0.009
Original	0.250	0.088	0.021	0.151	0.052	0.006
1.	0.305	0.132	0.054	0.206	0.083	0.030
2.	0.220	0.075	0.019	0.129	0.043	0.007
3.	0.241	0.081	0.022	0.148	0.048	0.008
4.	0.262	0.095	0.016	0.163	0.059	0.006
5.	0.256	0.091	0.020	0.154	0.054	0.006
6.	*0.422*	*0.182*	*0.073*	*0.340*	*0.146*	*0.043*
7.	0.273	0.099	0.022	0.173	0.063	0.008
8.	0.352	0.128	0.055	0.259	0.094	0.023
9.	0.283	0.102	0.026	0.181	0.063	0.010
10.	0.320	0.119	0.046	0.231	0.087	0.022
11.	0.372	0.156	0.050	0.291	0.119	0.023
12.	0.301	0.112	0.027	0.197	0.072	0.011
13.	0.317	0.114	0.026	0.216	0.078	0.015
14.	0.274	0.102	0.017	0.176	0.065	0.006
15.	0.413	0.161	0.043	0.327	0.122	0.022
16.	0.289	0.104	0.025	0.192	0.068	0.010
17.	0.361	0.133	0.058	0.270	0.099	0.026
18.	0.351	0.128	0.055	0.263	0.094	0.027
19.	0.248	0.086	0.021	0.154	0.052	0.008
20.	0.215	0.073	0.021	0.124	0.041	0.007
21.	0.212	0.075	0.017	0.118	0.041	0.005
22.	0.205	0.072	0.021	0.113	0.039	0.005
23.	**0.201**	**0.071**	**0.016**	**0.109**	**0.038**	**0.004**
24.	0.210	0.074	0.017	0.117	0.040	0.005
25.	0.274	0.097	0.019	0.175	0.059	0.009
26.	0.235	0.080	0.021	0.143	0.047	0.007
27.	0.255	0.088	0.022	0.158	0.054	0.006
28.	0.201	0.071	0.016	0.109	0.038	0.004
29.	0.207	0.073	0.018	0.119	0.040	0.005
30.	0.195	0.068	0.018	0.108	0.036	0.005
31.	0.198	0.069	0.018	0.107	0.037	0.004
32.	0.203	0.070	0.018	0.113	0.038	0.005
33.	0.257	0.089	0.020	0.161	0.054	0.007
34.	0.208	0.073	0.017	0.114	0.040	0.004
35.	0.295	0.111	0.025	0.171	0.065	0.006

Table B.3: RMSE and MAE values for the velocities from 35 simulations, rounded off to three decimal places. Bold font symbolizes the most favorable model, while italicized text symbolizes the least favorable model.

	Control input gradients					
	RMSE [N/s]			MAE [N/s]		
No.	$\hat{X}'_{ref}$	$\hat{Y}'_{ref}$	$\hat{N}'_{ref}$	$\hat{X}'_{ref}$	$\hat{Y}'_{ref}$	$\hat{N}'_{ref}$
Experiment	170.028	61.003	187.217	66.940	46.033	91.311
Original	270.046	40.645	63.136	159.414	15.239	18.473
1.	344.178	129.742	181.012	219.648	53.344	88.403
2.	236.119	46.988	69.040	145.047	16.219	22.029
3.	252.666	42.850	63.799	156.513	17.409	20.919
4.	285.645	40.580	50.048	170.099	14.748	16.074
5.	250.832	35.866	53.066	134.400	11.539	13.532
6.	*468.009*	*227.987*	*304.189*	*354.000*	*108.063*	*147.767*
7.	270.227	39.217	57.910	145.191	14.386	17.721
8.	397.848	156.489	235.727	269.657	59.442	76.566
9.	322.196	53.225	82.329	199.483	23.213	32.263
10.	361.480	111.206	158.493	245.407	50.397	68.795
11.	416.104	175.993	213.510	299.421	67.658	78.672
12.	345.516	83.291	95.194	213.128	32.879	36.318
13.	357.320	61.050	85.492	229.854	35.184	47.050
14.	306.609	44.976	55.471	187.089	17.271	16.471
15.	428.876	130.484	150.679	298.402	60.705	63.128
16.	298.499	45.373	68.960	173.604	20.265	24.757
17.	339.714	147.729	206.347	209.389	49.098	66.158
18.	390.031	157.311	215.378	270.320	63.173	88.638
19.	253.616	42.727	59.490	157.829	17.198	21.707
20.	227.923	38.422	61.524	136.697	13.896	20.070
21.	215.632	38.123	49.976	125.473	10.623	11.219
22.	206.065	37.009	60.443	120.701	10.095	12.257
23.	**191.322**	**36.802**	**46.890**	**111.261**	**9.120**	**9.206**
24.	211.709	43.255	52.204	122.211	12.961	13.437
25.	306.943	49.022	66.217	190.848	22.464	27.489
26.	621.531	753.196	62.296	159.005	23.141	19.258
27.	249.033	39.668	60.761	144.875	14.016	14.768
28.	192.012	35.959	49.249	111.119	9.156	9.304
29.	219.485	39.802	51.995	129.064	11.788	12.885
30.	202.455	36.297	54.585	115.732	10.123	11.862
31.	599.422	752.054	53.929	115.240	15.043	10.065
32.	203.975	37.154	54.965	117.556	10.595	11.413
33.	262.241	42.217	58.221	161.296	16.865	18.342
34.	211.073	39.339	49.885	121.174	9.903	10.724
35.	312.303	60.192	81.571	176.280	15.769	17.022

Table B.4: RMSE and MAE values for gradients of control inputs from 35 simulations, rounded off to three decimal places. The gradients have been calculated using finite differences, and the simulation rate of the control input references was $0.10\,\mathrm{s}$. Bold font symbolizes the most favorable model, while italicized text symbolizes the least favorable model.

Appendix C

Plots of the wave forces

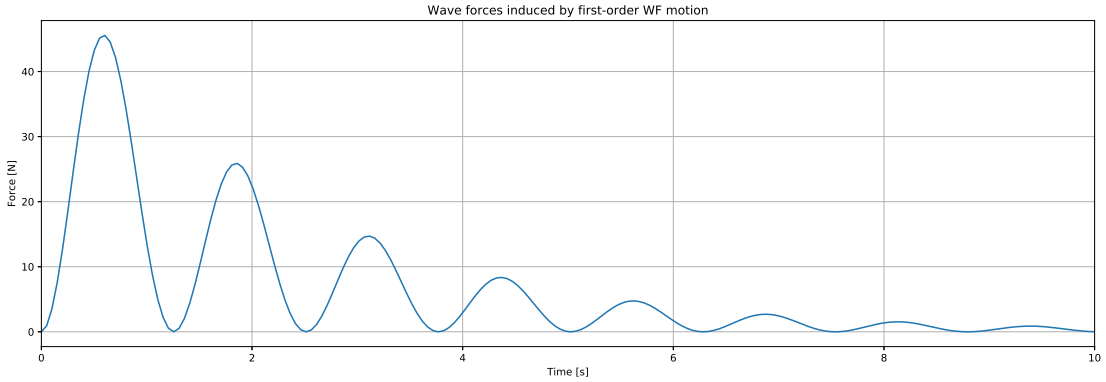

Figure C.1: The first-order wave-induced force $W_{xy}^{n}(t)$ given in $\{n\}$. The force is further decomposed in x^n and y^n given the desired wave encounter angle β, before being rotated to $\{b\}$.

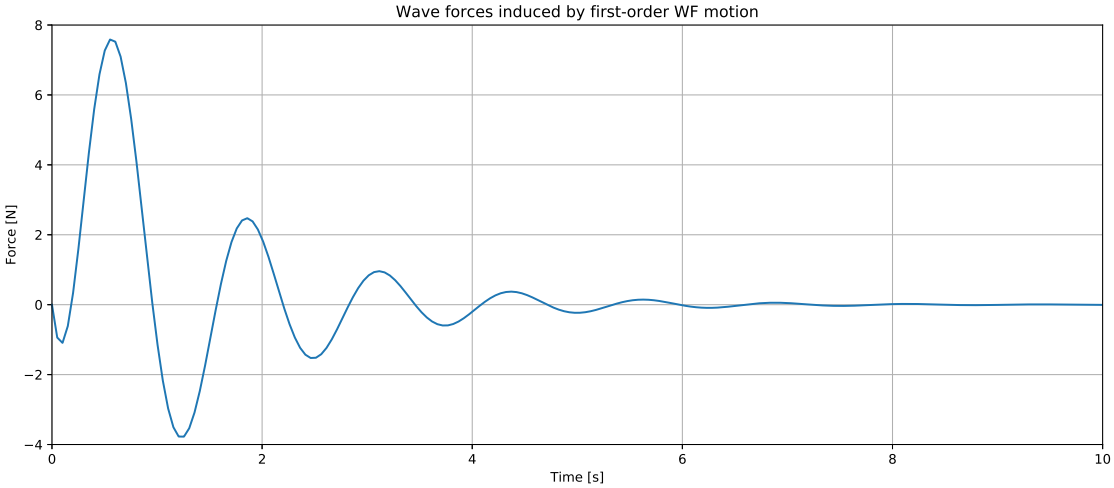

Figure C.2: The first-order wave-induced moment $W_{\psi}(t)$ affecting heading, given in $\{b\}$.

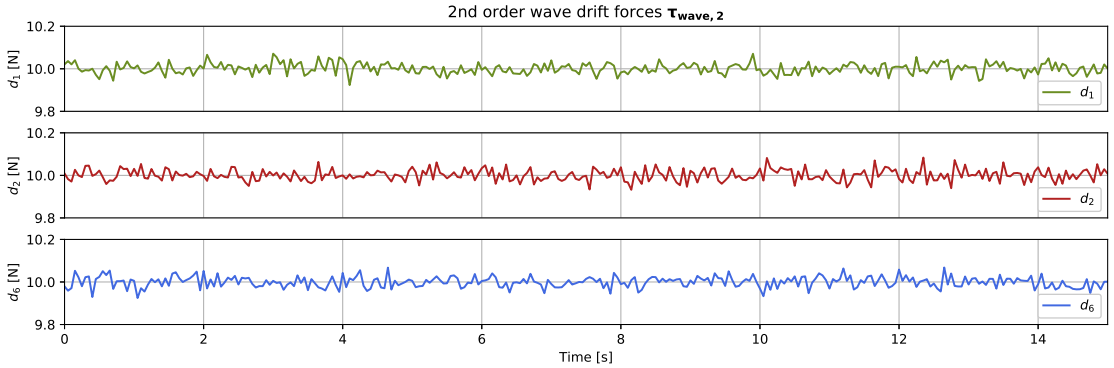

Figure C.3: The second-order wave drift forces, given in $\{b\}$, as a sum of a stationary value of $10\,\mathrm{N}$ as well as a dynamic part.

Appendix D

Overview of the ROS nodes and topics in the simulator

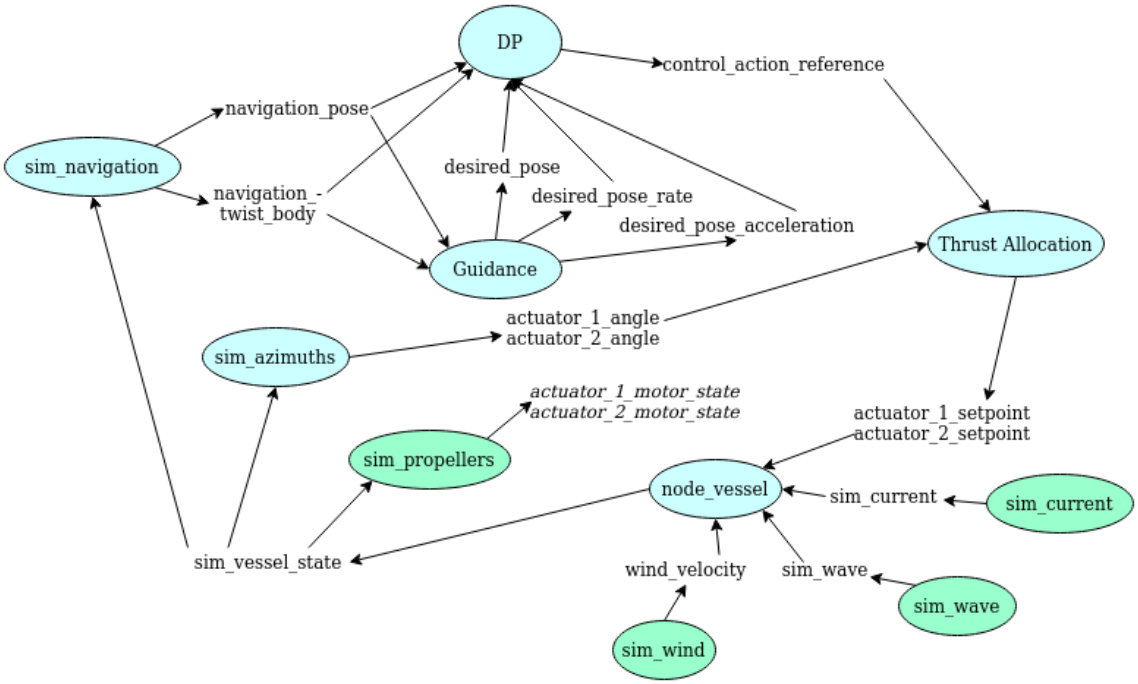

Figure D.1: Sketch of the most important nodes (colored ellipses) and topics used in the milliAmpere simulator. The flow of information is depicted as arrows.

Appendix E

Smallest signed angle (SSA)

The smallest signed angle (SSA) is a modification for the Euler angles, in the case of 3 degrees of freedom only the yaw angle ψ [Fossen, 2021]. The Euler angles are confined to the interval $[-\pi, \pi)$, and a problem arises in practical applications when error states are being used: If a craft with $\psi = 10°$ receives a heading reference of $350°$, a controller which do not consider the SSA would calculate an error of $-340°$. In other words, the control system commands an almost full rotation clockwise, albeit the reference is only $20°$ from the heading angle in an anti-clockwise direction [Fossen, 2021]. The SSA algorithm implemented in this thesis was written in Python using the library `NumPy` version 1.16.6, but originates from Fossen [2021, p.388]:

Listing E.1: Smallest signed angle algorithm, from Fossen [2021]. Implemented in Python using the library `NumPy`.

```
def ssa(angle, unit='rad'):
        """Smallest signed angle, the smallest
        difference between two angles.
        Maps an angle from [-pi, pi) [rad] or [-180, 180) [deg].
        See Fossen 2021 p. 388 for definition.

        @param angle: The angle to map.
        @param unit: Default 'rad', maps angle in radians.
            If 'deg' is specified, maps angle in degrees.
        @return: Mapped angle."""
        mapped_angle = np.nan
        if unit == 'rad':
                mapped_angle = ((angle + np.pi) % \
                    (2*np.pi)) - np.pi
        elif unit == 'deg':
                mapped_angle = ((angle + 180) % \
                    (360)) - 180
        return mapped_angle
```

Simen Krantz Knudsen

Model validation and berthing of an autonomous ferry

NTNU
Norwegian University of
Science and Technology